Noninvasive Optical Inhibition with a Red-Shifted Microbial Rhodopsin

by

Amy S. Chuong

B.S. in Biology
Massachusetts Institute of Technology, 2009

B.S. in Humanities and Science
Massachusetts Institute of Technology, 2009

M.S. in Media Arts and Sciences
Massachusetts Institute of Technology, 2011

Submitted to the Program in Media Arts and Sciences, School of Architecture and Planning,
in partial fulfillment of the requirements for the degree of
Doctor of Philosophy in Media Arts and Sciences

at the

Massachusetts Institute of Technology

June 2015

Author: Signature redacted

Program in Media Arts and Sciences
School of Architecture and Planning
March 19, 2015

Certified by: Signature redacted

Edward S. Boyden, III, Ph.D.
Benesse Career Development Professor
Program in Media Arts and Sciences, MIT
Thesis Supervisor

Accepted by: Signature redacted

Pattie Maes, Ph.D.
Academic Head
Program in Media Arts and Sciences

Noninvasive Optical Inhibition with a Red-Shifted Microbial Rhodopsin

by

Amy S. Chuong

Submitted to the Program in Media Arts and Sciences,

School of Architecture and Planning,

on March 19, 2015

in partial fulfillment of the requirements for the degree of

Doctor of Philosophy in Media Arts and Sciences

Abstract

Optogenetic inhibition of neurons enables the causal assessment of their contributions to brain functions, but a limit to the utility of optogenetic modulation is the quantity of neural tissue that can be successfully addressed from a given optical source. Previous optogenetic inhibitors are driven by blue, green, or yellow wavelengths, all of which suffer substantial light power attenuation as a result of tissue and hemoglobin optical absorption.

In this thesis, I describe the discovery, engineering, and implementation of a new red-shifted cruxhalorhodopsin, Jaws, derived from *Haloarcula salinarum* (strain Shark), which mediates three-fold higher red light-induced photocurrents than other inhibitory opsins. I describe the design process involved in engineering Jaws, as well as its characterization *in vitro*, *ex vivo*, within the awake *in vivo* rodent brain, and in transgenic mice. Jaws exhibits robust inhibition of sensory-evoked neural activity in the cortex and results in strong light responses when used in retinas of retinitis pigmentosa model mice. Finally, I demonstrate that Jaws can mediate transcranial optical silencing of neurons deep in the brains of awake mice. The noninvasive optogenetic inhibition opened up by Jaws enables a variety of important neuroscience experiments, and offers a powerful general-use chloride pump for basic and applied neuroscience.

Thesis Supervisor:
Ed Boyden, Ph.D.
Associate Professor
Program in Media Arts and Sciences, MIT

Noninvasive Optical Inhibition with a Red-Shifted Microbial Rhodopsin

by

Amy S. Chuong

The following served as readers on this dissertation

Signature redacted

Reader: _____

Thomas U. Schwartz, Ph.D.
Associate Professor
Department of Biology, MIT

Signature redacted

Reader: _____

Kay M. Tye, Ph.D.
Assistant Professor
Picower Institute for Learning and Memory, MIT
Department of Brain and Cognitive Sciences, MIT

Acknowledgements

A lot of people have helped me over the course of my Ph.D. work. I would first like to thank my advisor Ed Boyden, for his support as my research advisor and for the significant effort he put into making resources available for the lab and creating an intellectual environment.

My thesis committee members Kay Tye and Thomas Schwartz have always graciously made themselves available and freely offered outside perspectives. I would particularly like to thank Kay, who went out of her way to help me and invited me into her research group to learn slice electrophysiology.

I also want to thank Xue Han and Brian Chow, who let me share their project and work under them as a UROP. Brian provided much intellectual support and advice in the years following, and Xue was generous enough to let me work part-time in her research group as a graduate student. None of this would have been possible without their mentorship.

Jess Cardin, Hongkui Zeng, Yingxi Lin, Volker Busskamp, Andreas Sørensen, Mitra Miri and Botond Roska have been great collaborators. I am in particular indebted to Jess for letting me visit her research group, allowing me to watch her at the bench, and the significant time and effort she put into answering my many questions and emails.

Daniel Schmidt and Yongku Cho gave me much intellectual advice, feedback, and discussion, both on my research project as well as the scientific world outside light-activated proteins. Nathan Klapoetke has been a great intellectual resource and fellow labrat, even though his molecules go in the wrong direction. My graduate student experience would have been very different without the insights they helped provide: I can only hope to emulate their examples of how science should be done.

I would also like to thank:

The entire Boyden lab, in particular: Suhasa Kodandaramaiah, Masaaki Ogawa, Paul Tillberg and Fei Chen for their intellectual input and advice over the years.

The entire Han lab, in particular Richie Kohman and Jiamin Zhuo for teaching me how to do surgery and in vivo recordings.

The entire Tye lab, in particular Gillian Matthews and Anna Beyeler for teaching me slice electrophysiology and for being kind enough to share rig time and space.

None of this would have been possible without the love and support of my parents. Sherri Viera has been a great friend and help over the past decade, and I've been incredibly lucky in my best friends, S. and C., who were patient and supportive through all the angst.

Lastly, I would like to thank my boyfriend, the greatest optics gnome in the world.

Table of Contents

Figure Listing

Chapter 1 - Introduction

Overview

My dissertation work has focused on the development and neuroscientific application of light-drivable ion pumps based on microbial rhodopsins, with a specific emphasis on red light drivable molecules in order to modulate large *in vivo* brain volumes. I here present and characterize a novel red-light drivable chloride pump known as Jaws, which enables the non-invasive inhibition of the mouse brain, and examine its capabilities in a number of contexts.

Background

The brain is a complex biological system, comprised of as many as billions of interconnected cells spanning a tremendous variety of circuits and cell types. To better understand this high order system, it is necessary to read out the behavior of individual subcomponents with high precision, as well as to modulate these subcomponents' activity. Classically, this modulation has been achieved with techniques such as physical ablation, genetic knockout, direct electrode stimulation, temperature control, pharmacogenetics or conventional pharmacology, but none of these methods have been able to provide both spatial and cell-type specificity.

In 1979, Francis Crick stated that the field of neuroscience was limited by the rate of gathered information relative to the system's complexity, and that new techniques would be needed for studying and measuring neurobiological features, such as "a method by which all neurons of just one type could be inactivated, leaving the others more or less unaltered"[1]. Over the past three decades, a range of technologies has been devised to address this problem of cell-type specific neuromodulation.

Optogenetics, the light-modulatable activity of genetically-targeted cells or cell-types, was implemented in its initial form by Gero Miesenböck in 2002 by coexpressing photoreceptor genes with a G-protein α subunit in Drosophila neurons to generate light-induced depolarization[2]. Other early work focused on engineering photoswitchable chemical ligands in conjunction with

genetically-encoded ion channels[3-5], but the practical implementation of such methods was limited by the number of components which needed to be expressed and modulated.

In its more common use today, optogenetics refers to the light-sensitization of genetically specified neurons through the heterologous expression of microbial rhodopsins. Optogenetic activation is conducted with depolarizing algal-derived cation channels known as channelrhodopsins[6-8], while optogenetic inhibition utilizes hyperpolarizing microbial outward proton pumps known as bacteriorhodopsins[9, 10], or inward chloride pumps known as halorhodopsins[11-14] (Figure 1.1). These tools are typically heterologously expressed through viral transduction, transgenic line generation, or electroporation, and have been widely adopted by the neuroscience community to interrogate complex brain modalities such as hunger[15, 16], anxiety[17-20], sensory processing[21, 22], adult neurogenesis[23] and depression[24, 25].

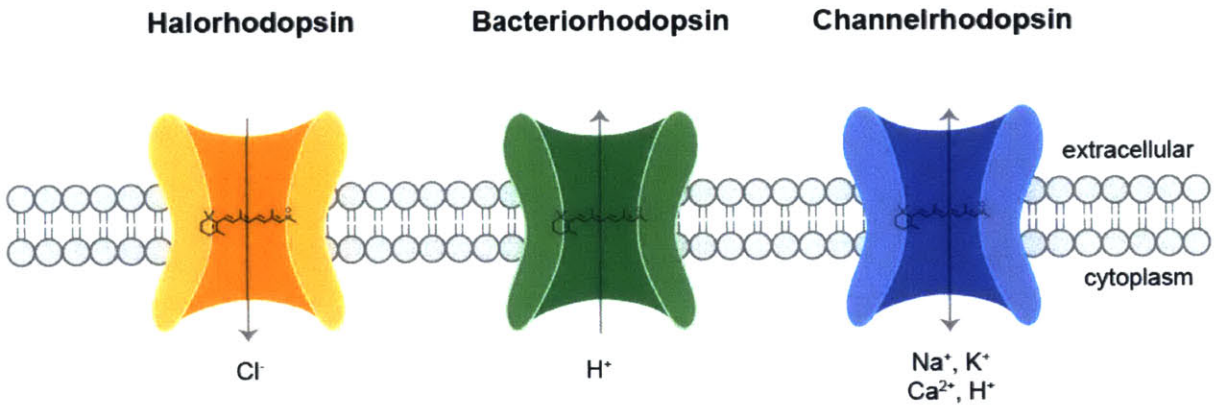

Figure 1.1 - Type I microbial rhodopsins

Halorhodopsins and bacteriorhodopsins respectively pump chloride ions into or protons out of the cell, hyperpolarizing it, while channelrhodopsins are non-specific cation channels that depolarize the cell's membrane potential.

Microbial rhodopsins

All members of the opsin superfamily share a highly characteristic seven transmembrane alpha-helical structure and retinal chromophore attached to a conserved lysine residue, but can be divided by primary sequence alignment into two independent protein families: microbial "type 1"

opsins which mediate phototaxis and light-driven ion transport[26], and the higher eukaryotic "type 2" opsins, which mediate vision[27] and circadian rhythms[28, 29]. It is currently unknown whether the two protein families descend from a single shared ancestor or result from horizontal gene transfer[30] or convergent evolution[31]. Other photoreceptor families of interest include the xanthopsins, light-oxygen-voltage (LOV) sensors, blue-light sensors using flavine adenine dinucleotide (BLUF), cryptochromes, phytochromes, and cyanobacteriochromes.

Type 1 opsins are divided into transporters (bacteriorhodopsin[32, 33], halorhodopsin[34-36]) which maintain electrochemical potentials/hyperpolarize the cell membrane, and "visual" photoreceptors (sensory rhodopsin I[37-40], sensory rhodopsin II/phoborhodopsin[41-46]) for microbial phototaxis. Extensive structural work has been carried out on both types, resulting in a number of crystallographic structures[47-54], in particular for the *H. salinarum* halorhodopsin[55, 56], *N. pharaonis* halorhodopsin[57] and the *C. reinhardtii* "C1C2" ChR1/ChR2 chimera[58]. Transport mechanisms vary among the different opsin classes, but they all possess an all-*trans*-retinal chromophore bound to a conserved lysine residue in helix 7 via a Schiff base. Upon photon absorption, the chromophore isomerizes into the 13-*cis* form (Figure 1.2), resulting in either a Schiff base rotation or a helix-helix shifting which ultimately leads to ion transport.

From a functional optogenetics standpoint, the major microbial rhodopsin classes of interest are the chloride pumping halorhodopsins (halorhodopsin, cruxhalorhodopsins), the proton pumping bacteriorhodopsins (archaerhodopsins, bacteriorhodopsins), and the non-specific cation channel channelrhodopsins.

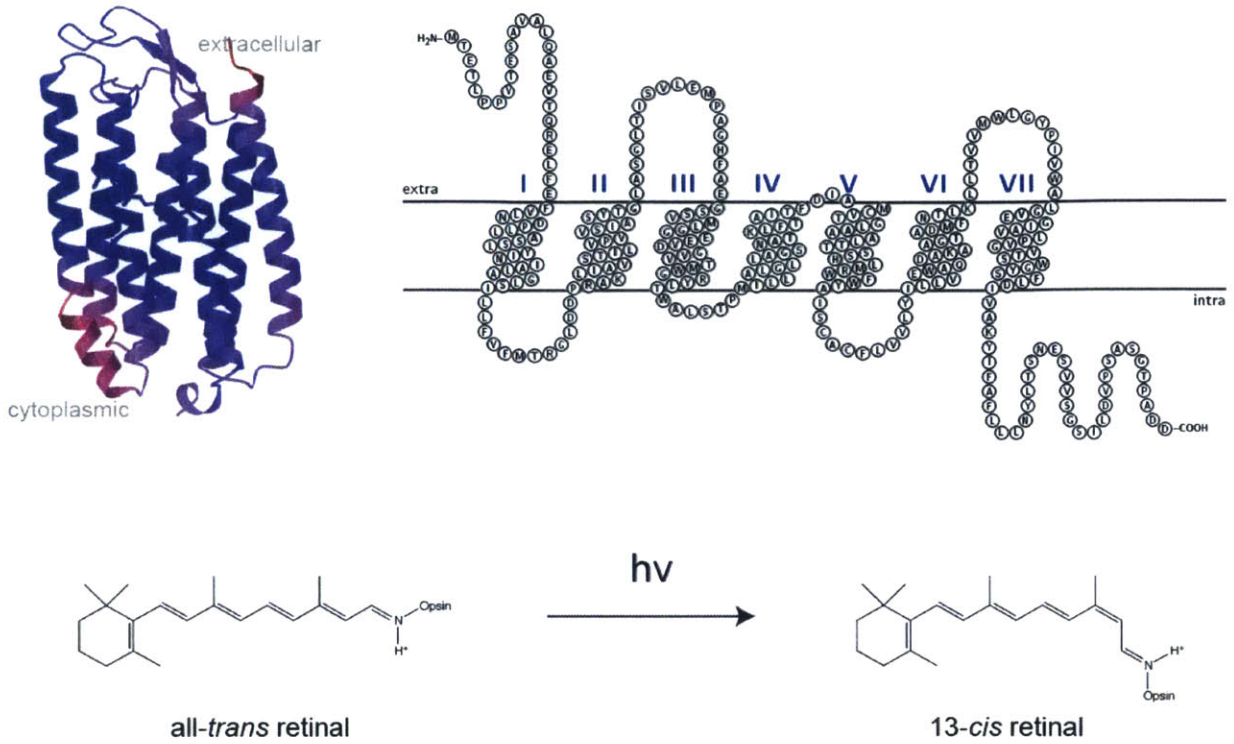

Figure 1.2 - Halorhodopsin protein and retinal chromophore

All opsins have a highly stereotyped seven transmembrane helix structure connected to a retinal chromophore via a Schiff base, as represented here by the *H. salinarum* halorhodopsin (*top*). Upon illumination, the retinal chromophore undergoes an isomerization from the all-*trans* conformation to 13-*cis* (*bottom*). The crystal structure shown at top left was adapted from Kolbe *et al.*[56]

Channelrhodopsins

The first reported channelrhodopsins were channelrhodopsin-1 (ChR1)[59] and channelrhodopsin-2 (ChR2)[6], both of which were isolated from the green freshwater algae *Chlamydomonas reinhardtii* between 2002 to 2003. While a number of other channelrhodopsin sequences have been identified and published[7, 8, 60, 61], many have had limited optogenetic utility due to poor heterologous expression and/or function in mammalian systems. From a functional optogenetics perspective, the naturally occurring opsins of primary interest are restricted to ChR2, the *Volvox carteri* channelrhodopsin-1 (VChR1)[8], the *Chlamydomonas noctigama* channelrhodopsin-1 (Chrimson)[7] and the *Stigeoclonium helveticum* channelrhodopsin (Chronos)[7].

Detailed channelrhodopsin mechanisms are not yet well understood, but it is generally

agreed that cation conduction occurs during the P_{520} intermediate (Figure 1.3), and that while attempts have been made to alter channelrhodopsin conductance[62], that this conductance is primarily non-selective and includes Na^+, H^+, Ca^{2+} and K^+. Broadly, engineering efforts have focused primarily on spectral shift, improving channel kinetics, and photocurrent amplitude: these have been typically executed via genomic mining, chimeragenesis, or directed protein engineering resulting in molecules such as C1V1[63], ReaChR[61], Chef[64], Chief[64], CsChrimson[7], and the step function opsins[65, 66].

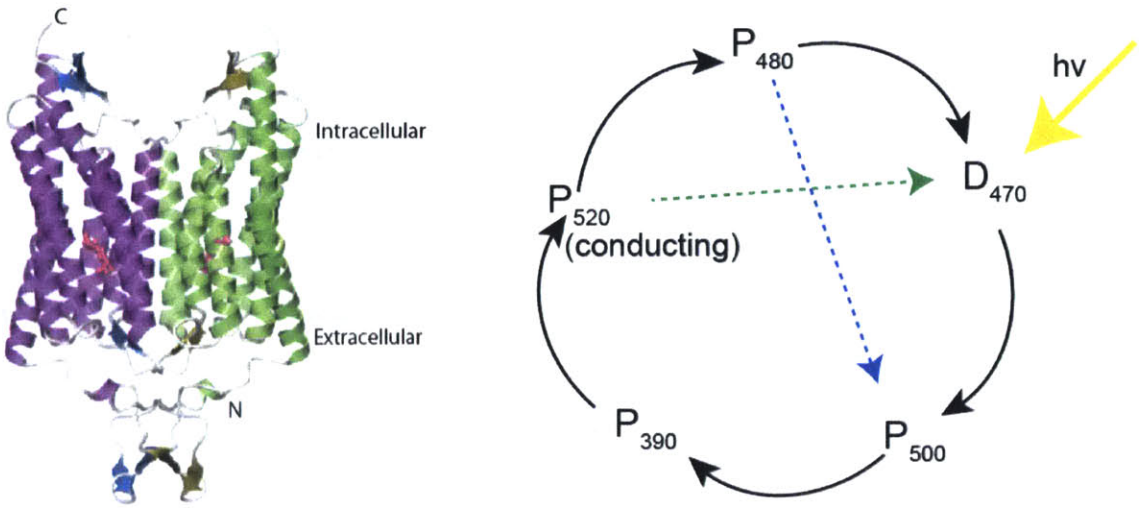

Figure 1.3 - Channelrhodopsins are light-gated non-specific cation channels.

Crystal structure of the *Chlamydomonas reinhardtii* ChR1/ChR2 chimera (C1C2), as adapted from Kato *et al.* 2012[58] (*left*) and channelrhodopsin-2 photocycle (*right*). Photocycle states are typically identified via spectroscopy and referred to by letters; subscript numbers refer to their absorbance maxima at each photocycle intermediate. Dashed lines indicate alternate photocycle pathways which can respectively be triggered by blue or green illumination.

Halorhodopsins and bacteriorhodopsins

Early microbial rhodopsin studies focused on the *Halobacterium salinarum* bacteriorhodopsin[32] due to its high protein stability and ability to be optically activated, making it an ideal model system for detailed biophysical investigation. The wildtype *H. salinarum* bacteriorhodopsin does not have sufficient photocurrent for optogenetic applications (data not shown), but subsequent genetic screening led to the identification of proton pumps from

Halorubrum sodomense (Arch[9]), *Halorubrum* strain TP009 (ArchT[10]) and *Leptosphaeria maculans* (Mac[9]).

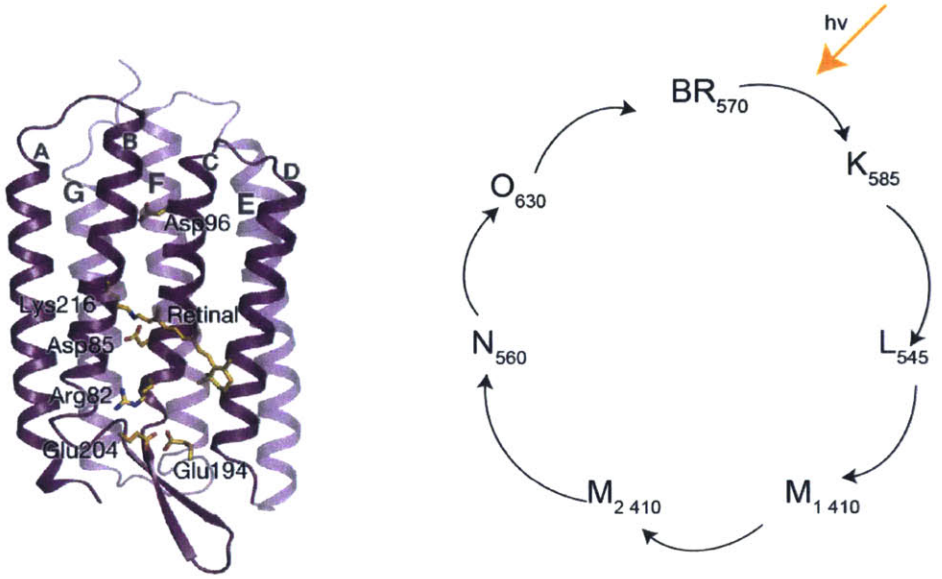

Figure 1.4 - Bacteriorhodopsin structure and photocycle are highly stereotyped for entire microbial rhodopsin class.

Bacteriorhodopsin structure, modified from Wickstrand *et al*[67] (*left*) and photocycle (*right*). In its K ground state, water molecule 402 bridges the positively charged Schiff base with negatively charged Asp85 and Asp212. Illumination causes the retinal to isomerize (K->L) such that a proton is directly transferred to Asp85 (L->M), after which the proton is extracellularly released. Asp96 reprotonates the retinylidene nitrogen (M2->N), Asp96 is cytoplasmically reprotonated simultaneously with the retinal reisomerization (N->O), followed by O state decay back to the ground K state.

While the halorhodopsin and bacteriorhodopsin families share only 25% sequence homology, they have remarkably similar structures and photocycles[68] and have even demonstrated interconvertible ion selectivities via azide addition[69, 70], acidification[71], or bacteriorhodopsin Asp85 mutations[72, 73]. A number of halorhodopsin sequences have been identified, but the two most characterized are the *Halobacterium salinarum* halorhodopsin (sHR) and the *Natronomonas pharaonis* halorhodopsin (pHR, NpHR, or halo). A third, evolutionary distinct family of chloride pumps are the cruxhalorhodopsins (cR) derived from the haloarcula class[74], and the three different halorhodopsins homologs have roughly 25% sequence conservation. Of these, the *H. salinarum* halorhodopsin does not possess sufficient photocurrent

in mammalian cells for optogenetic inhibition (data not shown), so the *N. pharaonis* halorhodopsin has received the bulk of neuroscientific attention[13, 14]. My thesis work has focused on the cruxhalorhodopsins, which I will discuss later in more detail.

All halorhodopsins possess both chloride and nitrate inward pumping activity, and mutual binding competition has been observed for both ions. The transport rate for Cl^- is three times the nitrate transport rate for the *H. salinarum* halorhodopsin[75, 76], but the two ions' transport rates are identical for the *N. pharaonis* halorhodopsin[75, 77], interestingly suggesting some mechanistic difference in ion selectivity/uptake. From an optogenetics perspective, nitrate transport is generally disregarded due to its low concentration levels relative to Cl^-.

There has been significant historical debate about the number of halorhodopsin ion binding sites, their specificity, and the role they play in translocation[78-80]. X-structures of the *H. salinarum* halorhodopsin identified a transport site (site I) near the Schiff base, and suggested a second, transient cytoplasmic release site (site II)[56]. A third extracellular Cl^- binding site has been experimentally suggested but not directly observed in any structural studies[81]. Current consensus is in favor of the "one site, two state" model[80].

In its dark state, the transport binding site has a chloride binding affinity of 2.5 mM (NpHR) or 10 mM (sHR)[82]. Illumination photoisomerizes the retinal chromophore from its all-*trans* state into a 13-*cis*, 15-*anti* conformation and the Schiff base N-H dipole rotates, causing the halorhodopsin to enter the HR_{600} state, displacing the chloride ion, and causing the transport site binding affinity to drop to 1.1 M[82] (while the cytoplasmic release site affinity remains a constant 5.7 M)[81]. The later photocycle steps are not as well characterized and are thought to diverge across different halorhodopsin types, but essentially the L state (HR_{520}) transition reflects the chloride ion movement from transport site to cytoplasmic release site, and Cl^- release and chromophore reisomerization occur during the L2 (HR_{520})→O1 (HR_{640}) transition. Chloride cytoplasmic release is aided by the T203/R200 ion pair[83, 84]: T203 most likely directly contacts the chloride ion, while the R200 effect is indirect and most likely relates to general structure. The cytosolic pathway then closes, and Cl- is reuptaken into the transport site during the O states (most likely via passive diffusion[85]), before the molecule returns to its initial HR_{580} state.

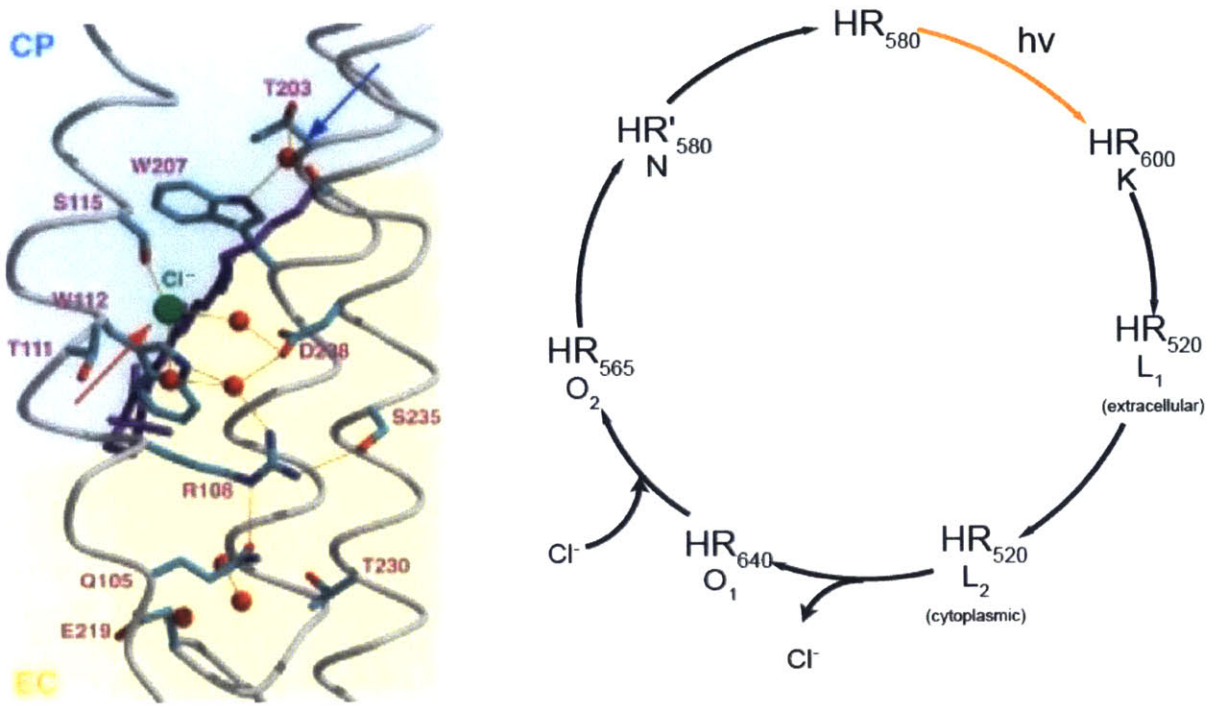

Figure 1.5 - Halorhodopsin photocycle primarily transports chloride ions.

H. salinarum halorhodopsin ion transport site (left) as schematized by Essen[86], and photocycle (*right*). The photocycles are thought to be generally similar between the *H. salinarum*, *N. pharaonis* and cruxhalorhodopsin halorhodopsins apart from some divergence in later photocycle intermediates and different absorption maxima at specific photocycle stages.

Optogenetic engineering

While the first round of optogenetic tools met with early success, there is still much room for improvement. From an implementation perspective, there are four primary constraints on optogenetic tools. The first of these is heterologous expression: the majority of microbial opsins functionally express poorly, due to differences between their parent algal/archaeal species and the system of interest. Inherent single-molecule biophysical properties--kinetics, photocurrent, and spectrum--necessarily limit the parameters for implementation. Light delivery, both in terms of the necessary amounts to drive an opsin, as well as constraints on the total amount of input power and spot irradiance are critical. Finally, an ideal actuating tool should modulate a circuit

only as much as is necessary to produce the desired effect, and with minimal other impact on the system under study.

A great deal of effort has gone into identifying/engineering novel optogenetic proteins, with varying degrees of success. Primarily these efforts have focused on altering channelrhodopsin kinetics, conductance, or spectrum through chimeragenesis, genomic mining, or the introduction of point mutations. However, the majority of these changes have resulted in some tradeoff between conductance and kinetics: to date the most commonly used channelrhodopsin is still the original channelrhodopsin-2 with the H134R mutation[87].

Substantially less engineering has been done on the inhibitory opsins. Since illumination is typically sustained and carried out on a seconds-to-minute timescale, primary parameters of interest include light sensitivity, conductance, cycle turnover, spectral shift and desensitization/recovery. However, efforts to improve these have been limited to genomic mining[9, 10] or appending signal sequences from the potassium channel Kir2.1[9, 12, 88] and the amount of mediated current per photocycle event is substantially lower for a pump versus a channel due to differences in active versus passive conductance. As a result, inhibitory opsins have generally been less widely used than the channelrhodopsins.

Within the context of *in vivo* optogenetics, light is typically delivered using a 50-200 μm diameter fiber and reported as irradiance in units of mW/mm^2: the primary constraints are optical falloff and attenuation from hemoglobin, lipid, and water (Figure 1.6). Under typical physiological conditions, the awake rodent brain is 33-36 C and homeostatically maintained by neural metabolism, arterial circulation cooling, and heat loss through the scalp[89, 90]. Disrupting this homeostasis alters neural behavior on the protein[91, 92], synaptic[93], cellular[94-96] and systems level[97], and sustained optical stimulation >500 ms at light powers above 100 mW/mm^2 has been reported to cause "significant tissue damage in cortex immediately under the optical fiber"[98] . Additionally, high light powers can cause recording photoelectric or behavioral[99, 100] artifacts. All of these necessarily constrain the amount of input light power to modulate a given volume, both in terms of local heating at the fiber tip (as a function of irradiance) and whole brain heating (as a function of total input power).

A number of neuroscientific problems require the ability to inhibit large brain volumes, however, this has thus far been limited both by ion conductance as well as light delivery. It would therefore be of great interest to the broader neuroscience community to create a novel

optogenetic inhibitor with high red light sensitivity, which might enable the inhibition of larger brain volumes than previously possible.

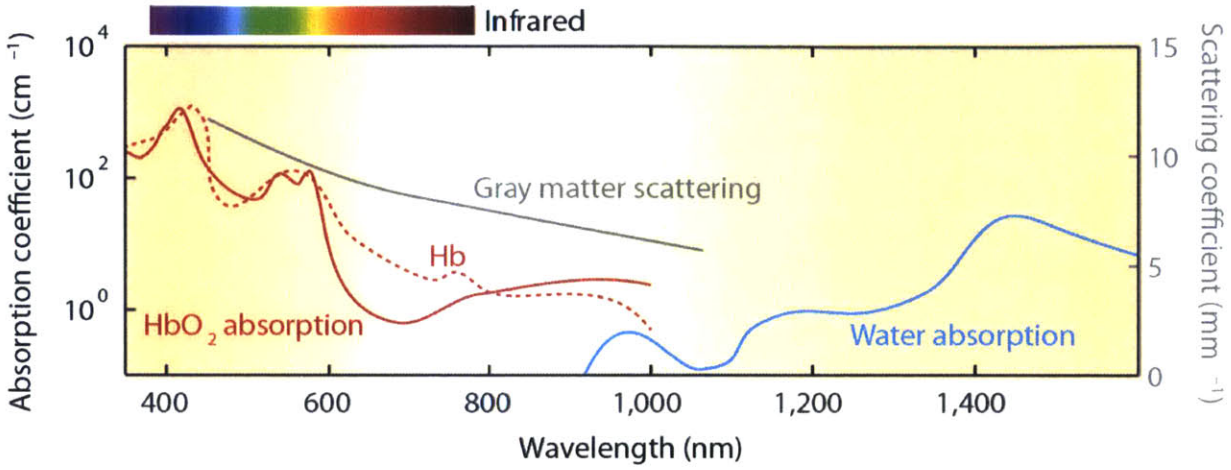

Figure 1.6 - Sources of optical attenuation in the brain

Optical propagation in the brain is heavily governed by hemoglobin, lipid and water attenuation. All currently existing optogenetic proteins are driven with blue, green, or yellow wavelengths which has substantially more hemoglobin attenuation than red wavelengths. It would therefore be desirable to develop red-light drivable optogenetic proteins. Figure modified from Smith *et al*[101].

References

1. Crick, F.H. Thinking about the brain. *Scientific American* **241**, 219-232 (1979).
2. Zemelman, B.V., Lee, G.A., Ng, M. & Miesenbock, G. Selective photostimulation of genetically chARGed neurons. *Neuron* **33**, 15-22 (2002).
3. Zemelman, B.V., Nesnas, N., Lee, G.A. & Miesenbock, G. Photochemical gating of heterologous ion channels: remote control over genetically designated populations of neurons. *Proceedings of the National Academy of Sciences of the United States of America* **100**, 1352-1357 (2003).
4. Banghart, M., Borges, K., Isacoff, E., Trauner, D. & Kramer, R.H. Light-activated ion channels for remote control of neuronal firing. *Nature neuroscience* **7**, 1381-1386 (2004).
5. Volgraf, M. et al. Allosteric control of an ionotropic glutamate receptor with an optical switch. *Nature chemical biology* **2**, 47-52 (2006).

6. Boyden, E.S., Zhang, F., Bamberg, E., Nagel, G. & Deisseroth, K. Millisecond-timescale, genetically targeted optical control of neural activity. *Nature neuroscience* **8**, 1263-1268 (2005).
7. Klapoetke, N.C. et al. Independent optical excitation of distinct neural populations. *Nature methods* (2014).
8. Zhang, F. et al. Red-shifted optogenetic excitation: a tool for fast neural control derived from Volvox carteri. *Nature neuroscience* **11**, 631-633 (2008).
9. Chow, B.Y. et al. High-performance genetically targetable optical neural silencing by light-driven proton pumps. *Nature* **463**, 98-102 (2010).
10. Han, X. et al. A high-light sensitivity optical neural silencer: development and application to optogenetic control of non-human primate cortex. *Frontiers in systems neuroscience* **5**, 18 (2011).
11. Chuong, A.S. et al. Noninvasive optical inhibition with a red-shifted microbial rhodopsin. *Nature neuroscience* (2014).
12. Gradinaru, V. et al. Molecular and cellular approaches for diversifying and extending optogenetics. *Cell* **141**, 154-165 (2010).
13. Han, X. & Boyden, E.S. Multiple-color optical activation, silencing, and desynchronization of neural activity, with single-spike temporal resolution. *PloS one* **2**, e299 (2007).
14. Zhang, F., Aravanis, A.M., Adamantidis, A., de Lecea, L. & Deisseroth, K. Circuit-breakers: optical technologies for probing neural signals and systems. *Nature reviews. Neuroscience* **8**, 577-581 (2007).
15. Aponte, Y., Atasoy, D. & Sternson, S.M. AGRP neurons are sufficient to orchestrate feeding behavior rapidly and without training. *Nature neuroscience* **14**, 351-355 (2011).
16. Atasoy, D., Betley, J.N., Su, H.H. & Sternson, S.M. Deconstruction of a neural circuit for hunger. *Nature* (2012).
17. Tye, K.M. et al. Amygdala circuitry mediating reversible and bidirectional control of anxiety. *Nature* **471**, 358-362 (2011).
18. Ciocchi, S. et al. Encoding of conditioned fear in central amygdala inhibitory circuits. *Nature* **468**, 277-282 (2010).
19. Haubensak, W. et al. Genetic dissection of an amygdala microcircuit that gates conditioned fear. *Nature* **468**, 270-276 (2010).
20. Johansen, J.P. et al. Optical activation of lateral amygdala pyramidal cells instructs associative fear learning. *Proceedings of the National Academy of Sciences of the United States of America* **107**, 12692-12697 (2010).
21. Atallah, B.V., Bruns, W., Carandini, M. & Scanziani, M. Parvalbumin-expressing interneurons linearly transform cortical responses to visual stimuli. *Neuron* **73**, 159-170 (2012).
22. Olsen, S.R., Bortone, D.S., Adesnik, H. & Scanziani, M. Gain control by layer six in cortical circuits of vision. *Nature* **483**, 47-52 (2012).
23. Gu, Y. et al. Optical controlling reveals time-dependent roles for adult-born dentate granule cells. *Nature neuroscience* **15**, 1700-1706 (2012).
24. Chaudhury, D. et al. Rapid regulation of depression-related behaviours by control of midbrain dopamine neurons. *Nature* **493**, 532-536 (2013).
25. Tye, K.M. et al. Dopamine neurons modulate neural encoding and expression of depression-related behaviour. *Nature* **493**, 537-541 (2013).

26. Spudich, J.L., Yang, C.S., Jung, K.H. & Spudich, E.N. Retinylidene proteins: structures and functions from archaea to humans. *Annual review of cell and developmental biology* **16**, 365-392 (2000).
27. Palczewski, K. G protein-coupled receptor rhodopsin. *Annual review of biochemistry* **75**, 743-767 (2006).
28. Freedman, M.S. et al. Regulation of mammalian circadian behavior by non-rod, non-cone, ocular photoreceptors. *Science* **284**, 502-504 (1999).
29. Provencio, I. et al. A novel human opsin in the inner retina. *The Journal of neuroscience : the official journal of the Society for Neuroscience* **20**, 600-605 (2000).
30. Sharma, A.K., Spudich, J.L. & Doolittle, W.F. Microbial rhodopsins: functional versatility and genetic mobility. *Trends in microbiology* **14**, 463-469 (2006).
31. Spudich, J.L., Yang, C.S., Jung, K.H. & Spudich, E.N. Retinylidene proteins: structures and functions from archaea to humans. *Annual review of cell and developmental biology* **16**, 365-392 (2000).
32. Oesterhelt, D. & Stoeckenius, W. Rhodopsin-like protein from the purple membrane of Halobacterium halobium. *Nature: New biology* **233**, 149-152 (1971).
33. Oesterhelt, D. & Stoeckenius, W. Functions of a new photoreceptor membrane. *Proceedings of the National Academy of Sciences of the United States of America* **70**, 2853-2857 (1973).
34. Lanyi, J.K. & Oesterhelt, D. Identification of the retinal-binding protein in halorhodopsin. *The Journal of biological chemistry* **257**, 2674-2677 (1982).
35. Lanyi, J.K. & Weber, H.J. Spectrophotometric identification of the pigment associated with light-driven primary sodium translocation in Halobacterium halobium. *The Journal of biological chemistry* **255**, 243-250 (1980).
36. Schobert, B. & Lanyi, J.K. Halorhodopsin is a light-driven chloride pump. *The Journal of biological chemistry* **257**, 10306-10313 (1982).
37. Bogomolni, R.A. & Spudich, J.L. Identification of a third rhodopsin-like pigment in phototactic Halobacterium halobium. *Proceedings of the National Academy of Sciences of the United States of America* **79**, 6250-6254 (1982).
38. Hildebrand, E. & Dencher, N. Two photosystems controlling behavioural responses of Halobacterium halobium. *Nature* **257**, 46-48 (1975).
39. Spudich, J.L. & Bogomolni, R.A. Mechanism of colour discrimination by a bacterial sensory rhodopsin. *Nature* **312**, 509-513 (1984).
40. Tsuda, M. Spectral changes in the photolysis of invertebrate rhodopsin by rapid scan spectrophotometry. *Methods in enzymology* **81**, 392-399 (1982).
41. Marwan, W. & Oesterhelt, D. Signal formation in the halobacterial photophobic response mediated by a fourth retinal protein (P480). *Journal of molecular biology* **195**, 333-342 (1987).
42. Spudich, E.N., Sundberg, S.A., Manor, D. & Spudich, J.L. Properties of a second sensory receptor protein in Halobacterium halobium phototaxis. *Proteins* **1**, 239-246 (1986).
43. Spudich, J.L. & Bogomolni, R.A. Sensory rhodopsins of halobacteria. *Annual review of biophysics and biophysical chemistry* **17**, 193-215 (1988).
44. Takahashi, T., Watanabe, M., Kamo, N. & Kobatake, Y. Negative phototaxis from blue light and the role of third rhodopsinlike pigment in halobacterium cutirubrum. *Biophysical journal* **48**, 235-240 (1985).

45. Tomioka, H., Takahashi, T., Kamo, N. & Kobatake, Y. Flash spectrophotometric identification of a fourth rhodopsin-like pigment in Halobacterium halobium. *Biochemical and biophysical research communications* **139**, 389-395 (1986).
46. Wolff, E.K., Bogomolni, R.A., Scherrer, P., Hess, B. & Stoeckenius, W. Color discrimination in halobacteria: spectroscopic characterization of a second sensory receptor covering the blue-green region of the spectrum. *Proceedings of the National Academy of Sciences of the United States of America* **83**, 7272-7276 (1986).
47. Henderson, R. & Unwin, P.N. Three-dimensional model of purple membrane obtained by electron microscopy. *Nature* **257**, 28-32 (1975).
48. Essen, L., Siegert, R., Lehmann, W.D. & Oesterhelt, D. Lipid patches in membrane protein oligomers: crystal structure of the bacteriorhodopsin-lipid complex. *Proceedings of the National Academy of Sciences of the United States of America* **95**, 11673-11678 (1998).
49. Grigorieff, N., Ceska, T.A., Downing, K.H., Baldwin, J.M. & Henderson, R. Electron-crystallographic refinement of the structure of bacteriorhodopsin. *Journal of molecular biology* **259**, 393-421 (1996).
50. Kimura, Y. et al. Surface of bacteriorhodopsin revealed by high-resolution electron crystallography. *Nature* **389**, 206-211 (1997).
51. Luecke, H., Richter, H.T. & Lanyi, J.K. Proton transfer pathways in bacteriorhodopsin at 2.3 angstrom resolution. *Science* **280**, 1934-1937 (1998).
52. Luecke, H., Schobert, B., Richter, H.T., Cartailler, J.P. & Lanyi, J.K. Structure of bacteriorhodopsin at 1.55 A resolution. *Journal of molecular biology* **291**, 899-911 (1999).
53. Pebay-Peyroula, E., Rummel, G., Rosenbusch, J.P. & Landau, E.M. X-ray structure of bacteriorhodopsin at 2.5 angstroms from microcrystals grown in lipidic cubic phases. *Science* **277**, 1676-1681 (1997).
54. Kunji, E.R., Spudich, E.N., Grisshammer, R., Henderson, R. & Spudich, J.L. Electron crystallographic analysis of two-dimensional crystals of sensory rhodopsin II: a 6.9 A projection structure. *Journal of molecular biology* **308**, 279-293 (2001).
55. Kunji, E.R., von Gronau, S., Oesterhelt, D. & Henderson, R. The three-dimensional structure of halorhodopsin to 5 A by electron crystallography: A new unbending procedure for two-dimensional crystals by using a global reference structure. *Proceedings of the National Academy of Sciences of the United States of America* **97**, 4637-4642 (2000).
56. Kolbe, M., Besir, H., Essen, L.O. & Oesterhelt, D. Structure of the light-driven chloride pump halorhodopsin at 1.8 A resolution. *Science* **288**, 1390-1396 (2000).
57. Kouyama, T. et al. Crystal structure of the light-driven chloride pump halorhodopsin from Natronomonas pharaonis. *Journal of molecular biology* **396**, 564-579 (2010).
58. Kato, H.E. et al. Crystal structure of the channelrhodopsin light-gated cation channel. *Nature* **482**, 369-374 (2012).
59. Nagel, G. et al. Channelrhodopsin-1: a light-gated proton channel in green algae. *Science* **296**, 2395-2398 (2002).
60. Govorunova, E.G., Sineshchekov, O.A., Li, H., Janz, R. & Spudich, J.L. Characterization of a highly efficient blue-shifted channelrhodopsin from the marine alga Platymonas subcordiformis. *The Journal of biological chemistry* **288**, 29911-29922 (2013).

61. Lin, J.Y., Knutsen, P.M., Muller, A., Kleinfeld, D. & Tsien, R.Y. ReaChR: a red-shifted variant of channelrhodopsin enables deep transcranial optogenetic excitation. *Nature neuroscience* **16**, 1499-1508 (2013).
62. Kleinlogel, S. et al. Ultra light-sensitive and fast neuronal activation with the Ca(2)+-permeable channelrhodopsin CatCh. *Nature neuroscience* **14**, 513-518 (2011).
63. Yizhar, O. et al. Neocortical excitation/inhibition balance in information processing and social dysfunction. *Nature* **477**, 171-178 (2011).
64. Lin, J.Y., Lin, M.Z., Steinbach, P. & Tsien, R.Y. Characterization of engineered channelrhodopsin variants with improved properties and kinetics. *Biophysical journal* **96**, 1803-1814 (2009).
65. Berndt, A. et al. High-efficiency channelrhodopsins for fast neuronal stimulation at low light levels. *Proceedings of the National Academy of Sciences of the United States of America* **108**, 7595-7600 (2011).
66. Berndt, A., Yizhar, O., Gunaydin, L.A., Hegemann, P. & Deisseroth, K. Bi-stable neural state switches. *Nature neuroscience* **12**, 229-234 (2009).
67. Wickstrand, C., Dods, R., Royant, A. & Neutze, R. Bacteriorhodopsin: Would the real structural intermediates please stand up? *Biochimica et biophysica acta* **1850**, 536-553 (2015).
68. Varo, G. Analogies between halorhodopsin and bacteriorhodopsin. *Biochimica et biophysica acta* **1460**, 220-229 (2000).
69. Varo, G., Duschl, A. & Lanyi, J.K. Interconversions of the M, N, and O intermediates in the bacteriorhodopsin photocycle. *Biochemistry* **29**, 3798-3804 (1990).
70. Scharf, B. & Engelhard, M. Blue halorhodopsin from Natronobacterium pharaonis: wavelength regulation by anions. *Biochemistry* **33**, 6387-6393 (1994).
71. Dér, A., Tóth-Boconádi, R. & Keszthelyi, L. Bacteriorhodopsin as a possible chloride pump. *FEBS letters* **259**, 24-26 (1989).
72. Sasaki, J. et al. Conversion of bacteriorhodopsin into a chloride ion pump. *Science* **269**, 73-75 (1995).
73. Ganea, C., Tittor, J., Bamberg, E. & Oesterhelt, D. Chloride- and pH-dependent proton transport by BR mutant D85N. *Biochimica et biophysica acta* **1368**, 84-96 (1998).
74. Otomo, J., Tomioka, H. & Sasabe, H. Bacterial Rhodopsins of Newly Isolated Halobacteria. *J Gen Microbiol* **138**, 1027-1037 (1992).
75. Duschl, A., Lanyi, J.K. & Zimanyi, L. Properties and photochemistry of a halorhodopsin from the haloalkalophile, Natronobacterium pharaonis. *The Journal of biological chemistry* **265**, 1261-1267 (1990).
76. Matsuno-Yagi, A. & Mukohata, Y. Two possible roles of bacteriorhodopsin; a comparative study of strains of Halobacterium halobium differing in pigmentation. *Biochemical and biophysical research communications* **78**, 237-243 (1977).
77. Lanyi, J.K., Duschl, A., Hatfield, G.W., May, K. & Oesterhelt, D. The primary structure of a halorhodopsin from Natronobacterium pharaonis. Structural, functional and evolutionary implications for bacterial rhodopsins and halorhodopsins. *The Journal of biological chemistry* **265**, 1253-1260 (1990).
78. Oesterhelt, D., Hegemann, P. & Tittor, J. The photocycle of the chloride pump halorhodopsin. II: Quantum yields and a kinetic model. *The EMBO journal* **4**, 2351-2356 (1985).

79. Lanyi, J.K. Light-dependent trans to cis isomerization of the retinal in halorhodopsin. *FEBS letters* **175**, 337-342 (1984).
80. Walter, T.J. & Braiman, M.S. Anion-protein interactions during halorhodopsin pumping: halide binding at the protonated Schiff base. *Biochemistry* **33**, 1724-1733 (1994).
81. Okuno, D., Asaumi, M. & Muneyuki, E. Chloride concentration dependency of the electrogenic activity of halorhodopsin. *Biochemistry* **38**, 5422-5429 (1999).
82. Chizhov, I. & Engelhard, M. Temperature and halide dependence of the photocycle of halorhodopsin from Natronobacterium pharaonis. *Biophysical journal* **81**, 1600-1612 (2001).
83. Paula, S., Tittor, J. & Oesterhelt, D. Roles of cytoplasmic arginine and threonine in chloride transport by the bacteriorhodopsin mutant D85T. *Biophysical journal* **80**, 2386-2395 (2001).
84. Rudiger, M. & Oesterhelt, D. Specific arginine and threonine residues control anion binding and transport in the light-driven chloride pump halorhodopsin. *The EMBO journal* **16**, 3813-3821 (1997).
85. Sato, M., Kanamori, T., Kamo, N., Demura, M. & Nitta, K. Stopped-flow analysis on anion binding to blue-form halorhodopsin from Natronobacterium pharaonis: comparison with the anion-uptake process during the photocycle. *Biochemistry* **41**, 2452-2458 (2002).
86. Essen, L.O. Halorhodopsin: light-driven ion pumping made simple? *Current opinion in structural biology* **12**, 516-522 (2002).
87. Nagel, G. et al. Light activation of channelrhodopsin-2 in excitable cells of Caenorhabditis elegans triggers rapid behavioral responses. *Current biology : CB* **15**, 2279-2284 (2005).
88. Mattis, J. et al. Principles for applying optogenetic tools derived from direct comparative analysis of microbial opsins. *Nature methods* **9**, 159-172 (2012).
89. Kalmbach, A.S. & Waters, J. Brain surface temperature under a craniotomy. *Journal of neurophysiology* **108**, 3138-3146 (2012).
90. Andersen, P. & Moser, E.I. Brain temperature and hippocampal function. *Hippocampus* **5**, 491-498 (1995).
91. Shibasaki, K., Suzuki, M., Mizuno, A. & Tominaga, M. Effects of body temperature on neural activity in the hippocampus: regulation of resting membrane potentials by transient receptor potential vanilloid 4. *The Journal of neuroscience : the official journal of the Society for Neuroscience* **27**, 1566-1575 (2007).
92. Nilius, B., Vriens, J., Prenen, J., Droogmans, G. & Voets, T. TRPV4 calcium entry channel: a paradigm for gating diversity. *American journal of physiology. Cell physiology* **286**, C195-205 (2004).
93. Moser, E., Mathiesen, I. & Andersen, P. Association between brain temperature and dentate field potentials in exploring and swimming rats. *Science* **259**, 1324-1326 (1993).
94. Han, X. Optogenetics in the nonhuman primate. *Progress in brain research* **196**, 215-233 (2012).
95. Hodgkin, A.L. & Katz, B. The effect of temperature on the electrical activity of the giant axon of the squid. *The Journal of physiology* **109**, 240-249 (1949).
96. Katz, B. & Miledi, R. The effect of temperature on the synaptic delay at the neuromuscular junction. *The Journal of physiology* **181**, 656-670 (1965).

97. Reig, R., Mattia, M., Compte, A., Belmonte, C. & Sanchez-Vives, M.V. Temperature modulation of slow and fast cortical rhythms. *Journal of neurophysiology* **103**, 1253-1261 (2010).
98. Cardin, J.A. et al. Targeted optogenetic stimulation and recording of neurons in vivo using cell-type-specific expression of Channelrhodopsin-2. *Nature protocols* **5**, 247-254 (2010).
99. Sparta, D.R. et al. Construction of implantable optical fibers for long-term optogenetic manipulation of neural circuits. *Nature protocols* **7**, 12-23 (2012).
100. Kravitz, A.V., Owen, S.F. & Kreitzer, A.C. Optogenetic identification of striatal projection neuron subtypes during in vivo recordings. *Brain research* (2012).
101. Smith, I.T. & Smith, S.L. Getting it through your thick skull. *Nature neuroscience* **17**, 1018-1019 (2014).

Chapter 2 – Non-invasive optical inhibition with a red-shifted microbial rhodopsin

This chapter was adapted from a paper published in Nature Neuroscience. I designed and developed Jaws, cloned all constructs, and carried out all *in vivo* glass pipette extracellular recordings. Nathan and I performed transfections, cell culture, *in vitro* virus infection and *in vitro* electrophysiology. Gillian, Andrew, Andreas and I performed *ex vivo* slice electrophysiology. Mitra and Jess carried out *in vivo* tetrode recordings and Volker performed multielectrode array recordings. Mitra, Volker, Gillian, Andreas, Shreshtha, Masaaki and I all performed histology. I coordinated all experiments and data analysis. Ed and I wrote the paper text, with contributions from other authors.

Introduction

Optogenetic inhibition, the use of light-activated ion pumps to enable transient activity suppression of genetically targeted neurons by pulses of light[1-3], is valuable for the causal parsing of neural circuit component contributions to brain functions and behaviors. A major limit to the utility of optogenetic inhibition is the addressable quantity of neural tissue. Previous optogenetic hyperpolarizers have successfully inhibited volumes of approximately a cubic millimeter, but many neuroscience questions require the ability to suppress larger tissue volumes. A number of pharmacogenetic, chemical and genetic strategies have been utilized for this purpose[4-7], but it would ideally be possible to address these large brain volumes with the millisecond temporal precision of optogenetic tools.

Another common desire in optogenetic experiments is to minimize invasiveness from inserting optical fibers into the brain, which displaces brain tissue and can lead to side effects such as brain lesion, neural morphology changes, glial inflammation and motility, or aseptic compromise[8-10] (Figure 2.1). Less invasive strategies that do not require an implanted optical device would also increase experimental convenience and enable longer-timescale experiments than often feasible with fragile implants. While a number of previous studies utilizing channelrhodopsins have attempted to address this problem with approaches such as placing the

optical fiber at the brain surface[11, 12], illuminating through optical windows[13, 14]/a thinned skull[15-17], or treating the skull with acrylic resin[18] (Table 2.1), non-invasive optical inhibition had not yet been possible due to the different light power requirements between channelrhodopsins, which conduct cations via passive transport, and the hyperpolarizing ion pumps, which rely on active transport[19].

It has been previously established that red light (635-660 nm) penetrates deeper into tissue than other visible wavelengths[20], most likely due to lessened hemoglobin optical attenuation[21, 22] (Figure 1.6). However, the majority of optogenetic inhibitors are driven with blue, green, or yellow light. The development of a red-light drivable silencer would therefore be of great interest to the neuroscience community, and potentially enable the silencing of much larger brain regions than previously possible.

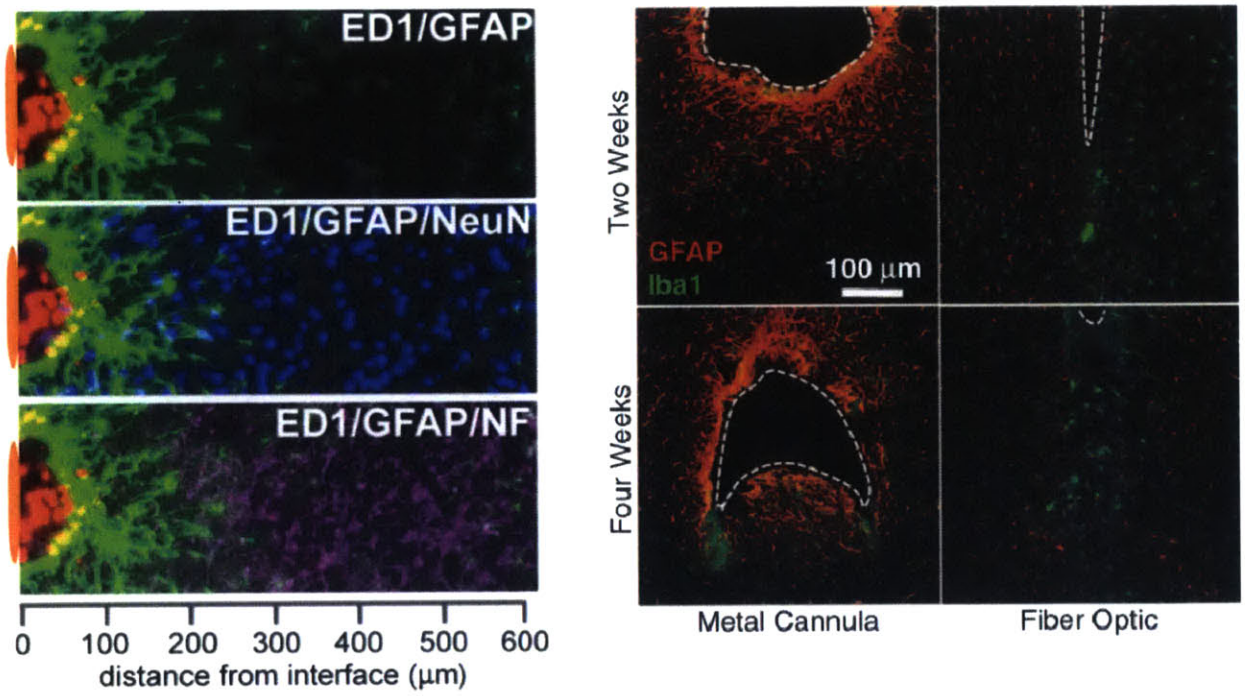

Figure 2.1 - Neural implantation leads to neuronal cell loss and immune response.

Representative images from an animal 4-weeks-post-implanatation with a microelectrode (*left*), modified from Biran *et al.* 2005[23], demonstrating inflammatory response (ED1, green) and astrocytic (GFAP, red) reactivity, as well as a reduction in $NeuN^+$ cell bodies (blue) and neurofilament (NF, purple) density, and an animal 2- and 4-weeks post-implantation with a metal cannula or optical fiber (*right*), modified from Kim *et al.* 2013[24], demonstrating astrocytic staining (GFAP, red) and activated microglia (Iba1, green).

Table 2.1 - All previous non-invasive optogenetic studies relied on activation.

Method	Reference	Expression Method	Wavelength
optical source at brain surface	Arenkiel Neuron 2007[11]	ChR2 transgenics	488 nm
	Yizhar Nature 2011[12]	ChR2 (C128S/D156A) injection	473 nm
	Lin Nature Neuro 2013[25]	ReaChR injection	617 nm
optical window / thinned skull	Gradinaru J. of Neuroscience 2007[15]	ChR2 transgenics	473 nm
	Huber Nature 2008[14]	ChR2 electroporation	470 nm
	Drew Nature Methods 2010[13]	ChR2 transgenics	467 nm
	Iwai Neuroscience Research 2011[16]	ChR2 transgenics	470 nm
	Scott PLoS One 2012[17]	ChR2 transgenics	473 nm
chemically treated skull	Hira J of Neuroscience Methods 2011[18]	ChR2 transgenics	473 nm

Engineering a novel red-light sensitive chloride pump from the cruxhalorhodopsin class

Previously, our lab screened type I microbial opsins from archaeabacteria, plants, bacteria, and fungi to identify hyperpolarizers similar to the *N. pharaonis* halorhodopsin (NpHR/halo) (Figure 2.2). Two chloride pumps identified in that screen, *H. vallismortis* and *H. marismortui* had the most red-shifted action spectra known for any hyperpolarizing opsin, but bore relatively low photocurrents. While their low photocurrents made them poor candidates for *in vivo* use[1], their spectra suggested they might be good scaffolds for further engineering.

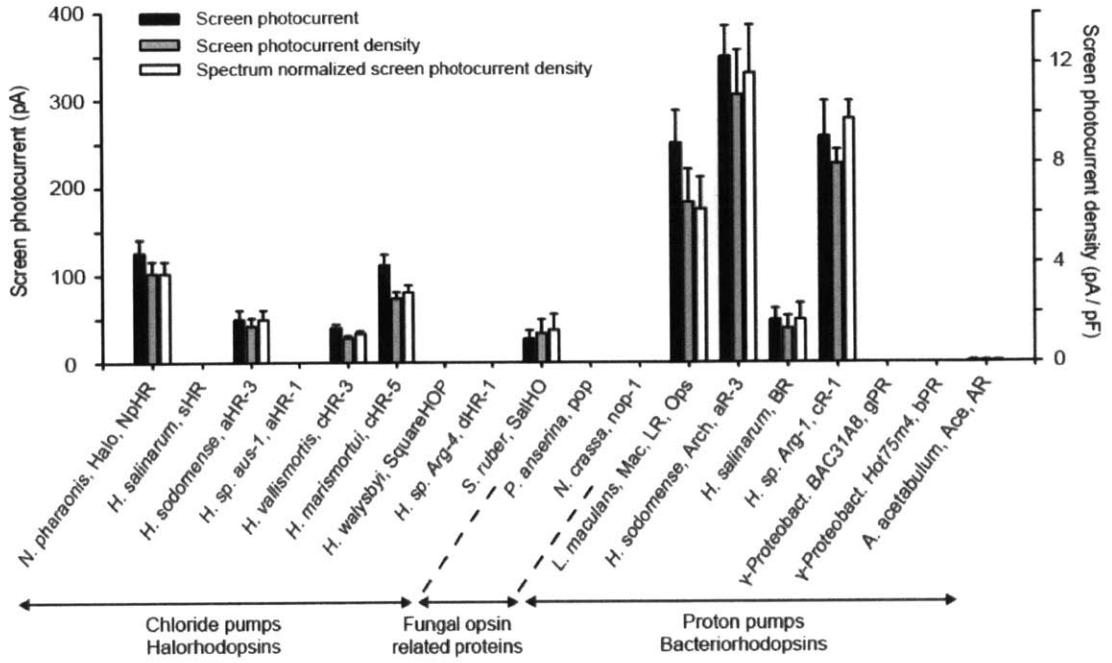

Figure 2.2 Optical neural silencing by light-driven proton pumping, revealed by a cross-kingdom functional molecular screen.

Photocurrents for different opsins across multiple kingdoms, as measured via whole-cell patch-clamp in cultured neurons. Full species names from left to right: *Natronomonas pharaonis, Halobacterium salinarum, Halorubrum sodomense*, *Halorubrum* species aus-1, *Haloarcula vallismortis, Haloarcula marismortui, Haloquadratum walsbyi, Haloterrigena* species Arg-4, *Salinibacter ruber, Podospora anserina, Neurospora crassa, Leptosphaeria maculans, Halorubrum sodomense, Halobacterium salinarum, Haloarcula species* Arg-1, uncultured gamma-proteobacterium BAC31A8, uncultured gamma-proteobacterium Hot75m4 and *Acetabularia acetabulum*. Figure modified from Chow *et al.*[1]

I therefore screened opsins within the cruxhalorhodopsin class for red-light photocurrents, based on homology to *H. vallismortis* and *H. marismortui* (Figure 2.3) and identified a molecule from *Haloarcula salinarum* (strain Shark) that I named "Halo57". Halo57 has an action spectra red-shifted by 14 nm relative to the *N. pharaonis* halorhodopsin, resulting in substantially higher red-light photocurrents (Figure 2.8a). Through rational mutagenesis, I identified two residues (K200R W214F) that boosted Halo57's photocurrent several-fold when mutated (Figure 2.4a-b) without altering its red action spectra (n = 9-10 cells; $P < 0.05$, ANOVA

with Dunnett's post hoc test). These mutations boosted opsin kinetics relative to the wildtype (Figure 2.5a; $P < 0.01$ for τ_{on} and $P < 0.001$ for τ_{off}, ANOVA with Newman Keuls post hoc test), as well as the photocurrent / fluorescence ratio (Figure 2.5b), suggesting that the observed effect is biophysical rather than expression level-based ($n = 4$-6 cells; $P = 0.02$, unpaired T-test).

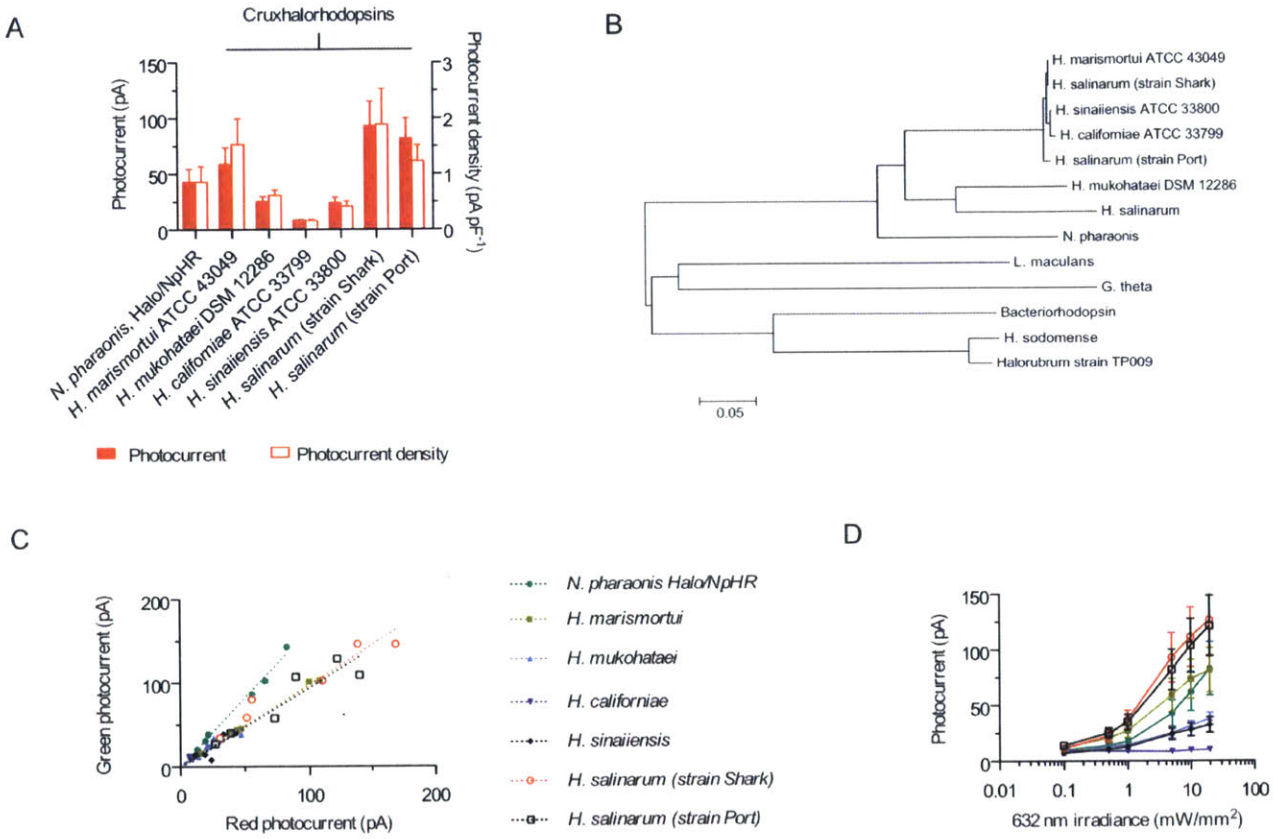

Figure 2.3 - Screening the cruxhalorhodopsin class

(a) Red light photocurrents (left y-axis, red bars) and photocurrent densities (right y-axis, white bars) from cruxhalorhodopsin class members and the *N. pharaonis* halorhodopsin in primary neuron culture. **(b)** Cruxhalorhodopsin phylogeny tree. Scale bar indicates number of amino acid substitutions per site. **(c)** Members of the cruxhalorhodopsin class have uniquely red-shifted spectra compared to the *N. pharaonis* halorhodopsin, as reflected by red-green photocurrent ratios in cultured cortical neurons. Regressed lines are shown for each opsin, indicating distinct color shifts. Illumination was 5 mW/mm^2 at 543 or 632 nm. **(d)** Photocurrents of cruxhalorhodopsin class members as a function of red light irradiance (632 nm; $n = 6$ cells for each opsin). All measurements were taken in primary neuron culture; all values are means ± standard error.

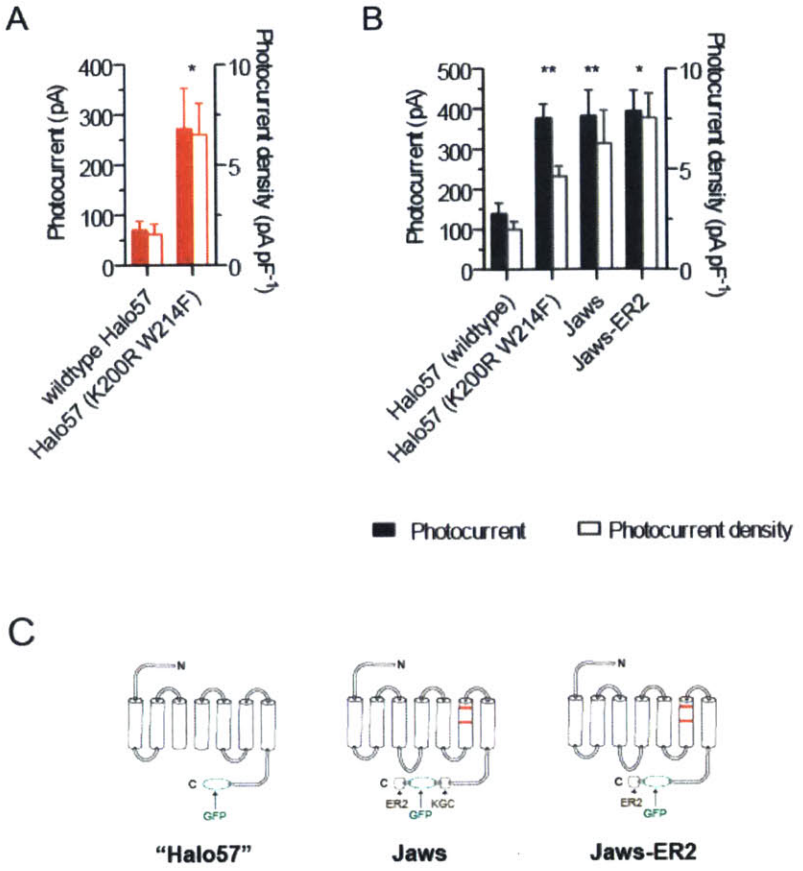

Figure 2.4 - Engineering Halo57

(a) The K200R W214F Halo57 mutant (n = 9 cells) demonstrates enhanced photocurrents over wild-type Halo57 in cultured neurons (n = 10 cells; 632 nm, 5 mW/mm^2). **(b)** Photocurrents (black bars) and photocurrent densities (white bars) for wild-type Halo57 (n = 9 cells), Halo57 (K200R W214F) (n = 21 cells), Jaws (n = 11 cells) and Jaws-ER2 in cultured neurons (n = 5 cells; 5 mW/mm^2, 543 nm; $P < 0.01$ for all variants compared to the wild-type Halo57). **(c)** Schematic of Halo57, Jaws, and Jaws-ER2 proteins. Black denotes the Halo57 protein scaffold, red indicates the K200R and W214F point mutations, green indicates the C terminal GFP fusion, and KGC and ER2 respectively refer to endoplasmic reticulum forward transport and Golgi export sequences from the potassium channel Kir2.1.

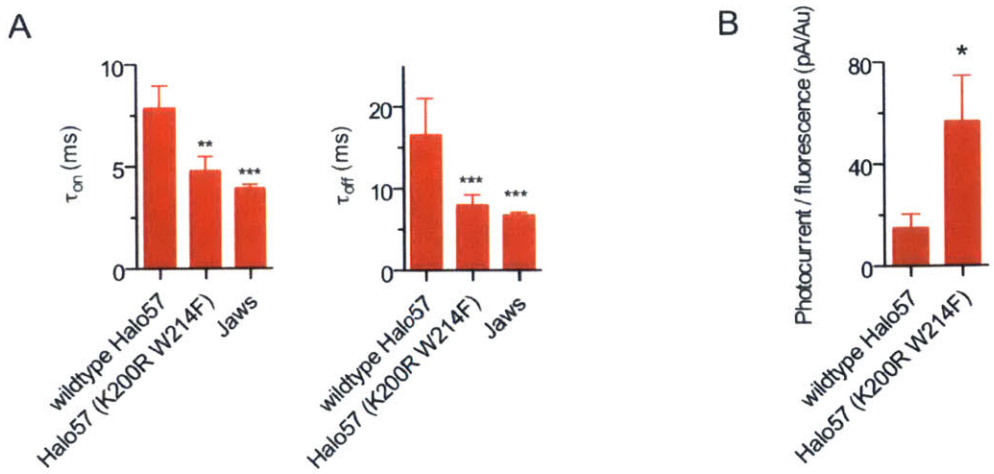

Figure 2.5 - The K200R W214F mutation is biophysical in nature.

(a) The K200R W214F Halo57 mutant and Jaws trafficking variant demonstrate enhanced kinetics over wild-type Halo57 in cultured neurons. **(b)** Photocurrent / fluorescence ratio of the wildtype mutant versus K200R W214 mutant.

I applied the homologous mutations to the *N. pharaonis* halorhodopsin and found them to be deleterious, suggesting a fundamental biophysical difference between Halo57 and the *N. pharaonis* halorhodopsin. This was unsurprising given that the two constructs share only 60% sequence homology (Figure 2.6) and have different chloride:nitrate affinity ratios, most likely due to differences in the binding site. Previous stopped-flow experiments suggest that the *N. pharaonis* halorhodopsin Cl^- uptake is limited by passive extracellular diffusion[26], but the τ_{on} improvement suggests this may not be the case for Halo57. Ion specific solutions confirm Jaws is a light-driven chloride pump (Figure 2.7) with an extrapolated reversal of -254 mV. I did not test Jaws' nitrate selectivity since the low levels of nitrate in the brain would render any nitrate currents minimal at best. Finally, I appended trafficking sequences from the potassium channel Kir2.1[27, 28] to result in the final molecules Jaws and Jaws-ER2 (Figure 2.4b,c). The addition of these sequences did not affect opsin biophysical properties (Figure 2.4b).

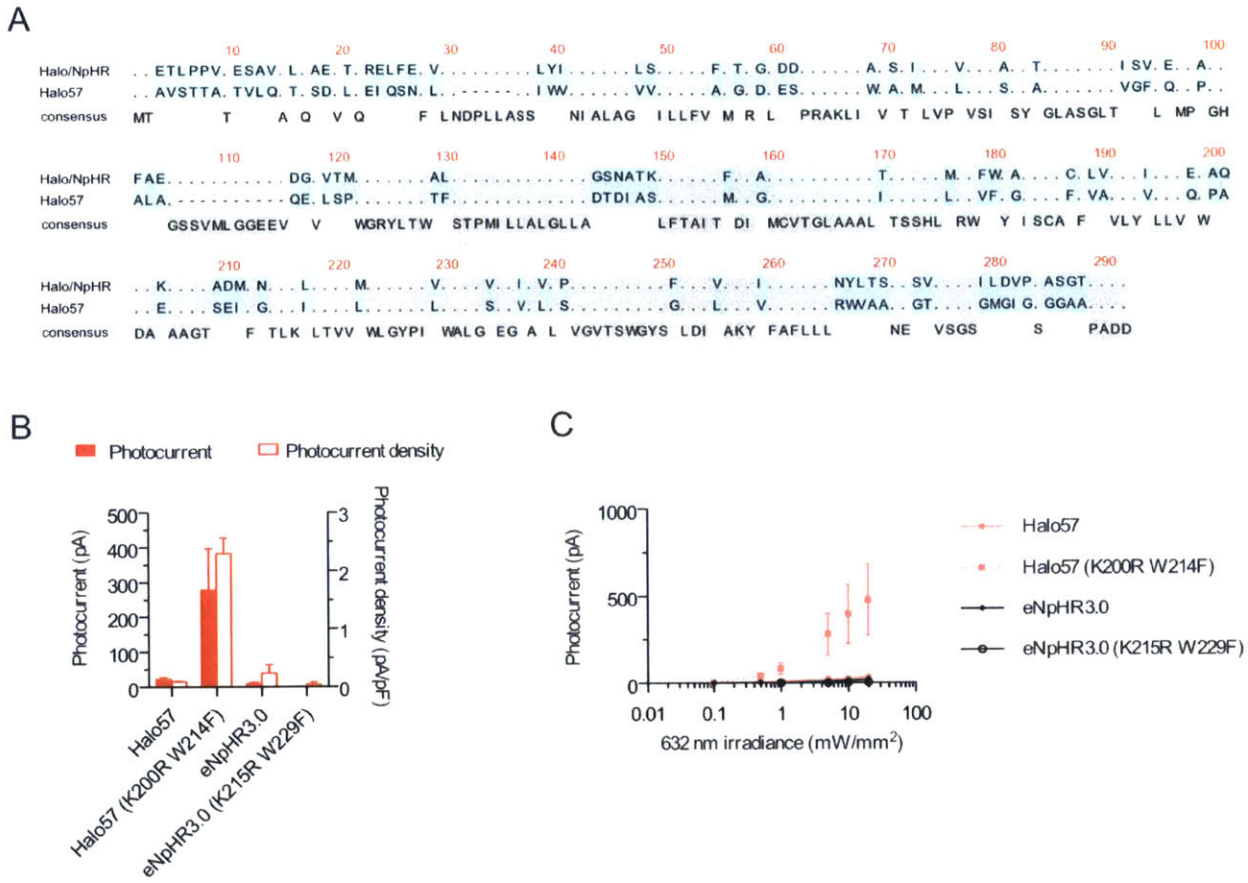

Figure 2.6 - The K200R and W214F mutations do not work for the *N. pharaonis* halorhodopsin.

(a) Sequence alignment of Halo57, the *H. salinarum* strain shark cruxhalorhodopsin, with the *N. pharaonis* halorhodopsin, demonstrating < 60% sequence homology; blue residues denote sequence divergence, and grey residues, conservation. **(b-c)** The K200R W214F mutation boosts Halo57 photocurrents (n = 3 cells for wildtype, n = 6 cells for K200R W214F mutant), but the homologous K215R W229F mutations cause no effect in eNpHR3.0 at 5 mW/mm^2 or across a range of 632 nm light powers (n = 3 cells for both wildtype and mutant eNpHR3.0). All measurements were taken in HEK293FT cells; values are mean ± standard error.

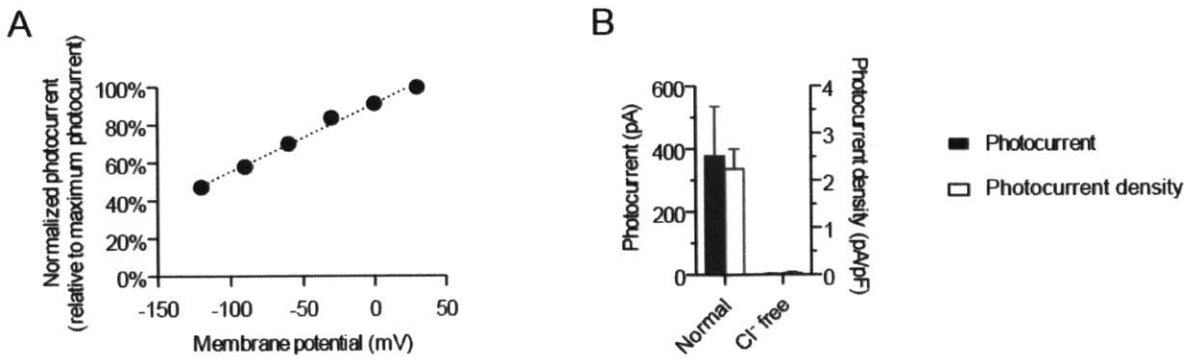

Figure 2.7 - Jaws is a chloride-selective ion pump.

(a) Current-voltage relationship for light-activated Jaws photocurrents (n = 5 cells; 632 nm, 5 mW/mm^2). Error bars are smaller than the symbols plotted. **(b)** Jaws photocurrent is dependent on [Cl^-] in the extracellular bath solution (n = 3-5 cells; 632 nm, 5 mW/mm^2). All measurements were taken in HEK293FT cells; values are mean ± standard error.

In vivo optogenetic inhibition has previously only been possible with blue, green and yellow light, due to the fact that current optogenetic silencers operate at only 10-30% of their peak capacity at red wavelengths. Because Jaws has a 14 nm red shift relative to the *N. pharaonis* halorhodopsin, we hypothesized that it might be a good candidate for potent red-light neural inhibition (Figure 2.8a-b). To further characterize this, I co-transfected Jaws, eNphR3.0, or ArchT into primary neuron culture along with a secondary cytosolic tdTomato plasmid and selected cells for whole-cell patch clamp characterization based solely on the presence of tdTomato (Figure 2.9), to be unbiased by visual appearance of the brightness of GFP fused to the opsin. This blind selection method helped avoid selection bias for opsin expression levels, and also more accurately represents the full range of in vivo expression: I found Jaws had significantly higher red light (632 nm) photocurrents than eNpHR3.0 or ArchT across all tested light powers (Figure 2.8c and Figure 2.9d; n = 21-30 cells; $P < 0.01$ for 0.1-20 mW/mm^2, ANOVA with Newman-Keuls post hoc test.) The robust *in vitro* photocurrents we observed seemed promising, so we next moved to assess Jaws in a variety of *in vivo* contexts.

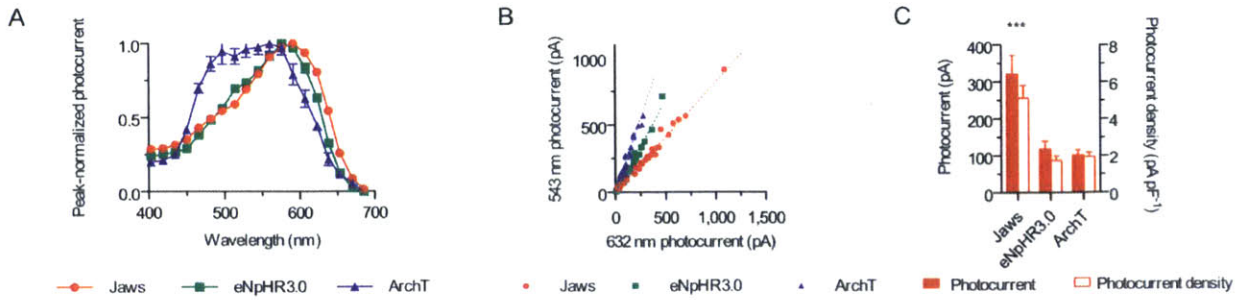

Figure 2.8 - Jaws has a distinct red-shift relative to other inhibitory opsins.

(a) Action spectra for Jaws (n = 12 cells), ArchT (n = 13 cells) and eNpHR3.0 (n = 15 cells; measured in cultured neurons using equal photon fluxes of ~3.0 x 10^{21} photons/s/m^2). **(b)** Red:green photocurrent ratios for Jaws (n = 33 cells), ArchT (n = 36 cells) and eNpHR3.0 in cultured neurons (n = 29 cells; 5 mW/mm^2 at 632 nm or 543 nm). Regressed lines are shown for each opsin, indicating distinct spectral shifts. **(c)** Red-light mediated photocurrents (left y-axis, red bars) and photocurrent densities (right y-axis, white bars) for Jaws (n = 33 cells), ArchT (n = 36 cells) and eNpHR3.0 in cultured neurons (n=29 cells; 5 mW/mm^2 at 632 nm). Values throughout are mean ± standard error. Panel c was an ANOVA with a Newman-Keuls post hoc test

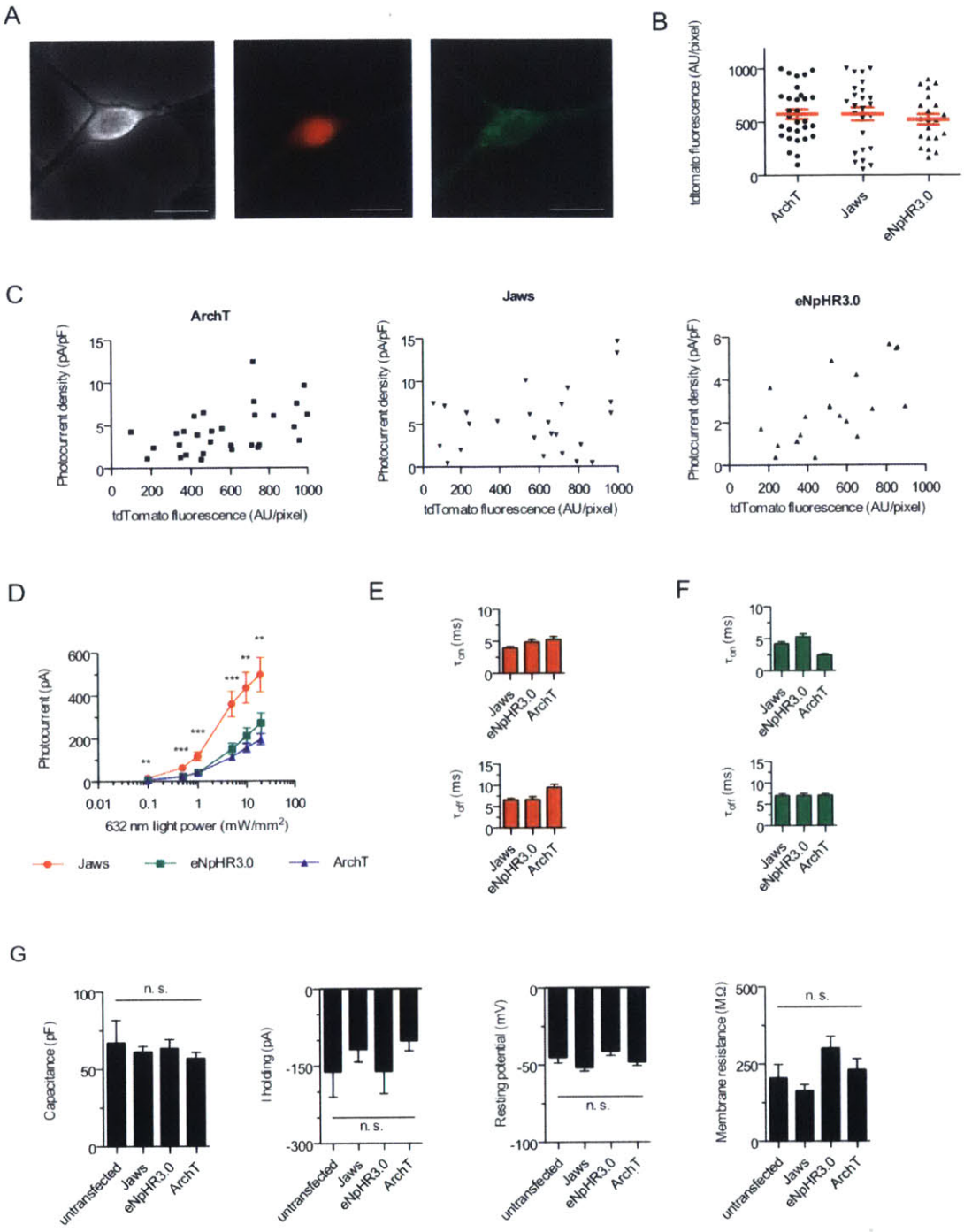

Figure 2.9 - Side-by-side comparison of different hyperpolarizing opsins.

(a) Representative phase contrast (*left*), tdTomato (*middle*) and GFP (*right*) images of a tdTomato and opsin-GFP fusion transfected neuron in culture. Scale bar is 50 µm. (**b-c**) Pooled tdTomato fluorescence **(b)** as well as plotted vs. photocurrent density for ArchT (*left*), Jaws (*middle*), and eNpHR3.0 (*right*). Photocurrents were measured at 5 mW/mm^2; 632

nm for Jaws (n = 26 cells) and eNpHR3.0 (n = 21 cells), and at 543 nm for ArchT (n = 30 cells). **(d)** Photocurrents for Jaws (n = 26 cells), eNpHR3.0 (n = 21 cells) and ArchT (n = 30 cells) as a function of red light irradiance (632 nm) as measured in transfected neuron culture. **(e-f)** Comparison of hyperpolarizing opsin on-kinetics and off-kinetics using red or green illumination for Jaws (n = 24 cells), eNpHR3.0 (n = 20 cells) or ArchT (n = 29 cells). **(g)** Neuron properties upon opsin expression in primary neuron culture for Jaws (n = 33 cells), ArchT (n = 36 cells), and eNpHR3.0 (n = 29 cells) as compared to untransfected cells (n = 15), including cell membrane capacitance, holding current when held at -65 mV, resting potential, and cell input resistance. Values are means ± standard error. Statistics for panels d and h: ** $P < 0.01$, *** $P < 0.001$. Panel d was an ANOVA with a Newman-Keuls post hoc test, panel g was an ANOVA with Dunnett's post hoc test using untransfected neurons as the reference.

Potential for optogenetic visual therapeutics

Optogenetic neural hyperpolarization is being explored not only as a tool for basic neuroscience, but also as a prototype therapeutic. As one example, retinitis pigmentosa (*RP*) is a visual disorder which first results in night blindness, and subsequent overall blindness as a result of photoreceptor degeneration[29]. A potential therapeutic treatment for patients with cone photoreceptor atrophy would be to resensitize the cone cells to light by genetically expressing light-activated hyperpolarizing ion pumps in the cone photoreceptors, which in their healthy state hyperpolarize in response to optical stimulation.

When expressed in retinal cones of RP mouse models, eNpHR has previously been shown to be capable of transducing spikes in downstream retinal ganglion cells and mediating visually guided behaviors (Figure 2.10). However, the resultant spiking rates are limited to less than 200 Hz, substantially less than the full wild-type range of 15-450 Hz[30], and thus potentially limiting fine visual perception in the potential scenario of future clinical use. Additionally, while eNpHR can be activated using light powers that are safe for human use[30], more light-sensitive hyperpolarizers would require less light for stimulation and thus provide a greater margin of efficacy and safety given the inevitable unknowns that might crop up in potential future trials in humans. Thus, better neural hyperpolarizers remain of great interest for potential future clinical use in the human eye.

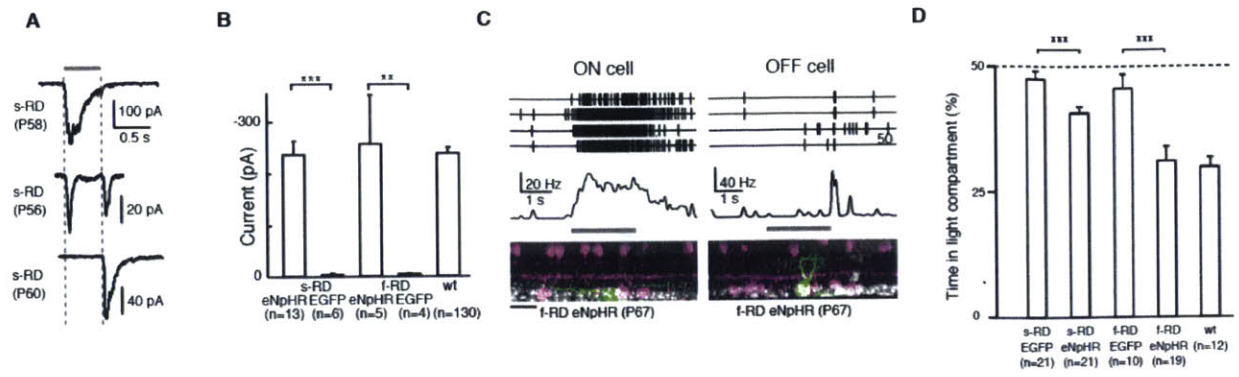

Figure 2.10 - eNpHR-expression is sufficient to restore visual function in RP mouse models

(a) Ganglion cell excitatory currents in ON (*top*), ON-OFF (*middle*), and OFF (*bottom*) ganglion cells in eNpHR-expressing s-RD retinas. Gray bars show the timing of the full-field light stimulus. **(b)** Magnitude of light-evoked peak excitatory currents in s-RD, f-RD, and WT mice. **(c)** Ganglion cell spiking output. *(Left)* Top, spike recordings (four repetitions) from ON (*left*) and OFF (*right*) ganglion cells from an eNpHR- expressing f-RD retina; middle, spike frequency responses (gray bar shows the timing of a full-field light stimulus); bottom, corresponding cells filled with neurobiotin (green), choline acetyltransferase (magenta) as an IPL stratification marker, and DAPI staining (white) to visualize nuclear layers. **(d)** Visually guided behavior in eNpHR-expressing RD mice. Dark-light box experiment. Percentage of time the AAV-injected RD animals and WT mice spent in the light compartment. Figure modified from Busskamp *et. al.* Science 2010[30].

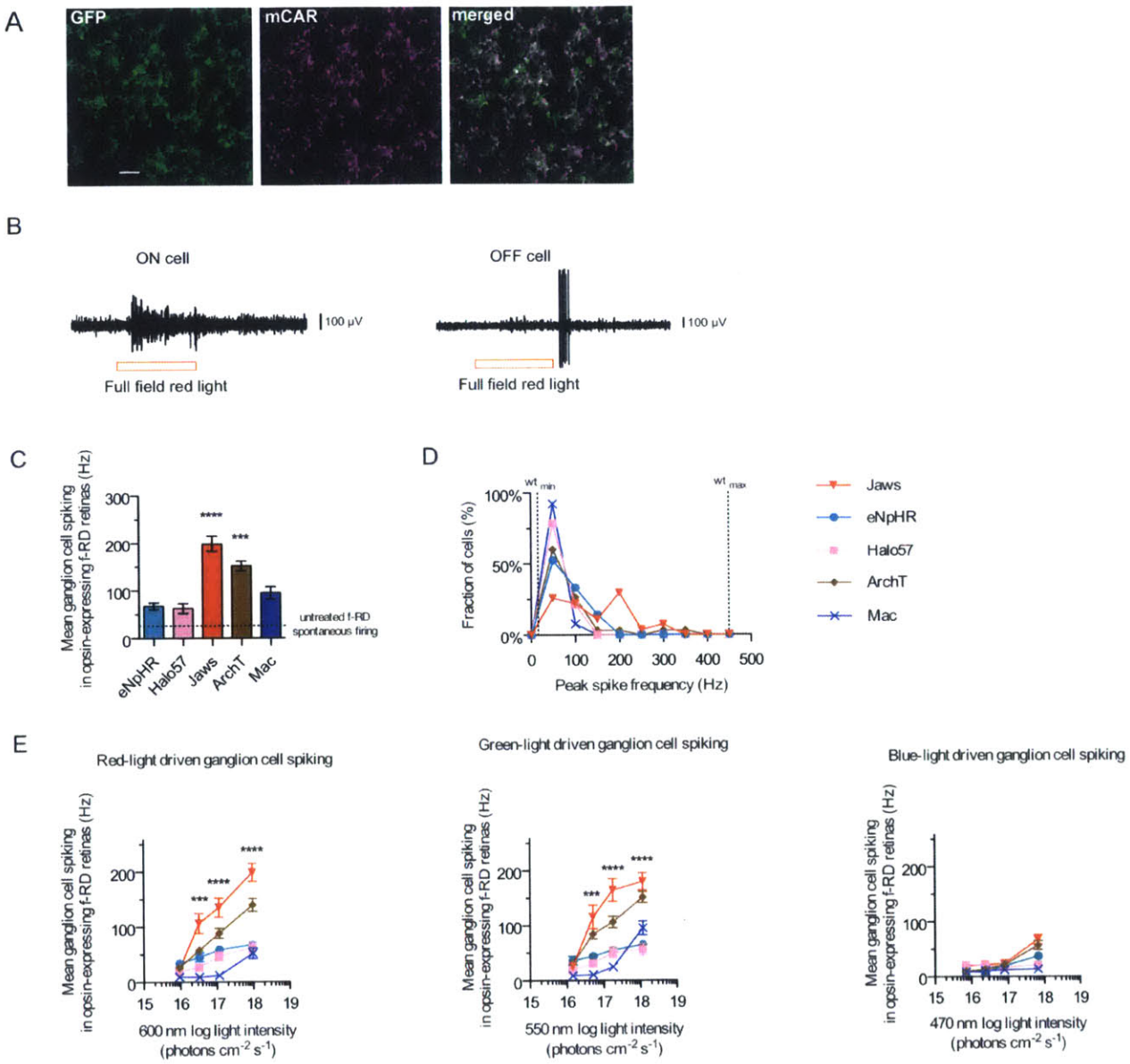

Figure 2.11 - Jaws-mediated light responses in murine retinitis pigmentosa retinas.

(a) Confocal fluorescence images from Jaws-GFP expressing retina (with the "fast" form of retinal degeneration (f-RD), stained for GFP (green) and mouse cone arrestin (mCAR) (magenta), 4 weeks post-injection with AAV8-mCAR-Jaws-GFP virus. Scale bar, 20 µm. **(b)** Raw traces recorded from ON and OFF retinal ganglion cells in retinas expressing Jaws in cone photoreceptors, optically stimulated with 9.6 x 10^{17} photons cm^{-2} s^{-1} at 600 nm for 1 second. **(c)** Comparison of mean spiking in ganglion cells downstream from eNpHR- (n = 21 cells), Halo57- (n = 14 cells), ArchT- (n = 30 cells), Mac (n = 13 cells), or Jaws-expressing (n = 27 cells) opsin-expressing neurons at opsin peak wavelength sensitivity (light intensity was 1.2 x 10^{18} photons cm^{-2} s^{-1} for green light (ArchT, Mac) and 9.6 x 10^{17} photons cm^{-2} s^{-1} for red light (Jaws, eNpHR, Halo57),

and baseline f-RD firing is indicated by the dotted line according to ref. [31]. **(d)** Population distribution of retinal ganglion cell peak firing rates at opsin peak wavelength sensitivity (light intensities as indicated in **C**; dotted lines indicate wild-type dynamic range[30]. **(e)** Retinal ganglion spike rate vs. red, green, and blue irradiances, measured in ganglion cells downstream of opsin-expressing cones in f-RD retina. Values are means $\pm$ standard error; n values for **c**, **d**, and **e** are as indicated in **c**. Statistics for panels **c**, **d** and **e**: * $P < 0.05$, ** $P < 0.01$, *** $P < 0.001$. Panel **d** was a Kolmogorov-Smirnov test, panels **c** and **e** were ANOVAs.

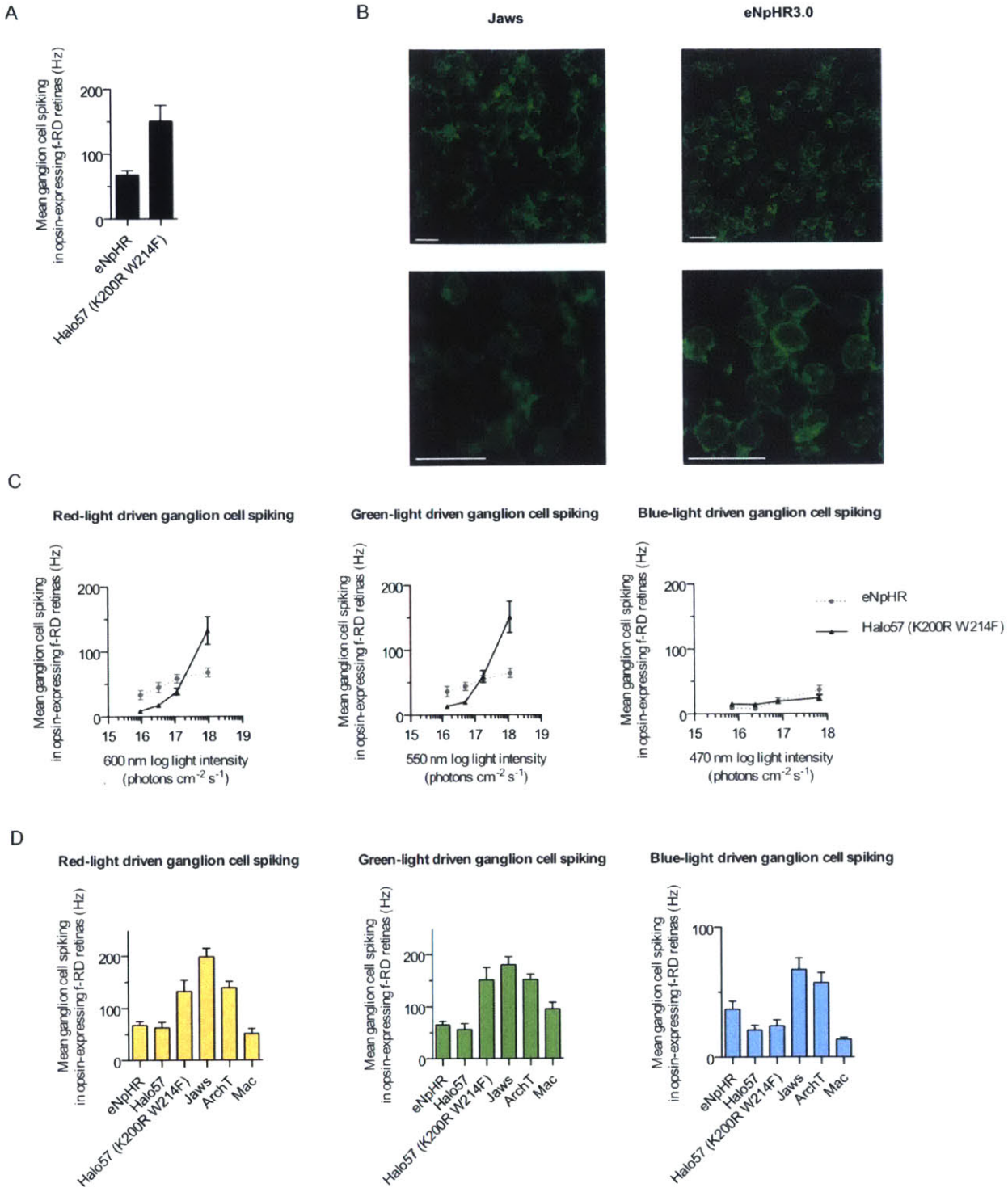

Figure 2.12 - Light responses mediated by cone expression and illumination of Halo57 (K200R W214F) in murine retinitis pigmentosa retinas.

(a) Comparison of mean spiking for Halo57 (K200R W214F) mutant (n = 16) in ganglion cells downstream from opsin-expressing neurons (9.6 x 10^{17} photons cm^{-2} s^{-1} at 600 nm), using AAV with the mCAR promoter

and serotype 8, ~40 days post infection. **(b)** Confocal fluorescence images of Jaws-GFP (left) and eNpHR3.0-expressing (right) f-RD retinas. Scale bars 20 μm. **(c)** Retinal ganglion cell spike rates vs. red (left), green (middle), and blue (right) irradiances, comparing Halo57 (K200R W214F) vs. eNpHR. **(d)** Comparison of retinal ganglion cell spiking under red, green, and blue illumination for eNpHR (n = 21 cells), Halo57 (n = 14 cells), Halo57 (K200R W214F) (n = 16 cells), Jaws (n = 27 cells), ArchT (n = 30 cells) or Mac (n = 13 cells) expressed in mouse cone cells (light intensity was 6.7 x 10^{17} photons cm^{-2} s^{-1} at 470 nm, 1.2 x 10^{18} photons cm^{-2} s^{-1} at 550 nm, and 9.6 x 10^{17} photons cm^{-2} s^{-1} at 600 nm). Values are means ± standard error.

We decided to first compare Jaws' performance against those of other known hyperpolarizers by injecting AAV8 encoding various light-driven proton or chloride pumps into the cone photoreceptors of $Pde6b^{rd1}$ mice, also called fast retinal degeneration mice (f-RD)[30, 32] (Figure 2.11a), which are blind by postnatal day 28 (P28). We conducted extracellular retinal ganglion cell recordings (Figure 2.11b) 4-6 weeks post-injection (P64-75) and found peak wavelength photostimulation of Jaws-expressing photoreceptors induced significantly more retinal ganglion spiking, indicated by mean spiking frequencies greater than for eNpHR, ArchT, Mac, or the wild-type Halo57 (Figure 2.11c, Figure 2.12b). Jaws also enabled a broader peak spike frequency distribution than other opsins ($P < 0.05$ for Jaws vs all other opsins, Kolmogorov-Smirnov test), with an increase in mean frequency from 67.8 ± 7.0 Hz with eNpHR, to 189.5 ± 15.9 Hz with Jaws (mean ± standard error), increasing the wild-type spiking bandwidth by 3-fold (Figure 2.11d). We additionally observed Jaws to mediate the highest ganglion spiking rates over various irradiances of 600 nm, 550 nm, and 470 nm light (Figure 2.11e, Figure 2.12c-d), indicating its high light sensitivity, which alongside Jaws' spectral peak at 600 nm may confer benefits because of the relative safety of 600 nm light[33]. We also found that the improvements between the wildtype Halo57 and K200R W214F mutant to be consistent with previous data in primary neuron culture (Figure 2.4, Figure 2.11, Figure 2.12) suggesting this improvement was not specific to expression in primary neuron culture. From this comparison of light-sensitive hyperpolarizers, we conclude Jaws may represent an optogenetic reagent with molecular properties better suited than previous opsins for therapeutic cone reactivation for a subset of retinitis pigmentosa patients.

In vivo suppression of visually-evoked cortical activity

We next evaluated the performance of Jaws in an experimental context common in neuroscience: the suppression of stimulus-evoked neural activity. Given the proximity of yellow light to all currently existing inhibitory opsins' peak excitation wavelengths[1, 2], we decided, for this specific experiment, to directly compare Jaws' *in vivo* performance in the mouse brain against that of other silencers, using yellow light. Although all previous studies characterizing optogenetic hyperpolarizers have focused on inhibiting spontaneous neural activity[1-3, 34], many neuroscientific questions focus on stimulus-evoked or event-associated neural activity[35]. The ability to suppress the activity of a given cell type responding to behaviorally relevant inputs is therefore critical.

To assess Jaws' potential as a general-purpose silencer of stimulus-evoked neural activity, we injected a Cre-dependent adeno-associated virus (AAV; serotype 5) expressing eNpHR, eNpHR3.0, Arch, ArchT, or Jaws into the primary visual cortex of Emx1-Cre transgenic mice and delivered visual stimuli while delivering yellow light with an optetrode (593 nm; 35 mW/mm^2 out of a 200 μm fiber tip). Inhibition of visually-evoked neural activity was strong (Figure 2.13a,b), with an 86 ± 3% reduction of visually evoked activity in Jaws-expressing cortex (Figure 2.13c; n = 27 units with a significant reduction in firing; n = 3 units showed no change and n = 3 units showed a significant increase in firing) over a range of evoked firing rates (1.8-12.5 Hz; Figure 2.14), and consistent across a range of input contrast strengths (Figure 2.13d). This comparison of neural silencers thus reveals that Jaws is capable of mediating excellent inhibition of evoked neural activity in a biologically meaningful context.

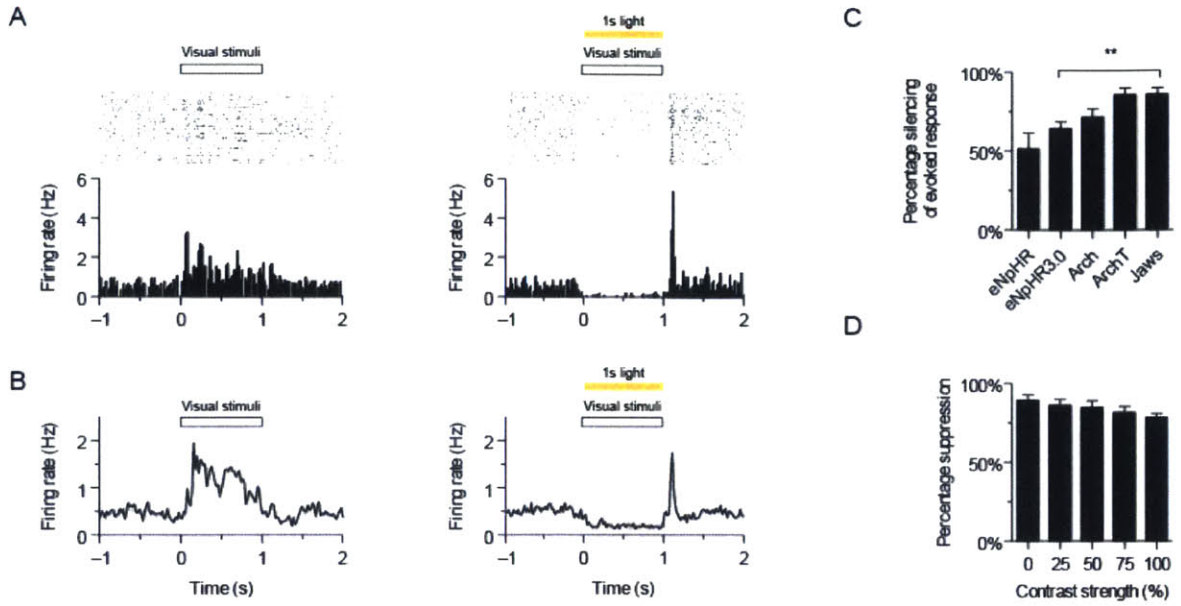

Figure 2.13 - Jaws-mediated inhibition of evoked responses in visual cortex.

(a) Representative rasters of visually evoked responses (top left) and Jaws-mediated inhibition of visually evoked responses (top right), and post-stimulus time histograms for visually evoked (bottom left) and Jaws-inhibited visually evoked (bottom right) responses, of a representative neuron (n = 27) in the visual cortex of an anesthetized Emx1-cre mouse, as measured by extracellular tetrode recording (AAV5-FLEX virus; 35 mW/mm^2 at 593 nm using a 200-42m fiber). **(b)** Population average of five simultaneously recorded neurons showing visually evoked responses (left) and Jaws-mediated inhibition of visually evoked responses (right). **(c)** Inhibition of visually evoked neural responses for eNpHR (n = 8 units from 2 mice), eNpHR3.0 (n = 32 units from 4 mice), Arch (n = 18 units from 3 mice), ArchT (n = 21 units from 3 mice) and Jaws (n = 27 units from 4 mice; $P < 0.01$ for Jaws versus eNpHR3.0). **(d)** Jaws-mediated inhibition of visually evoked responses (n = 14 units from 2 mice) for different visual input stimulus strengths.

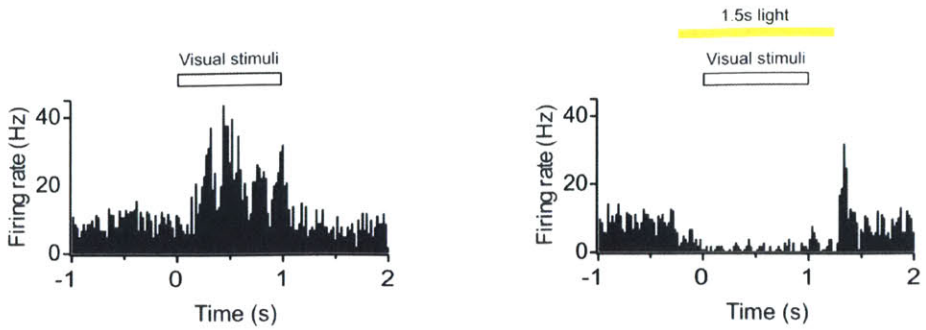

Figure 2.14 - Jaws shuts down fast-firing interneurons in visual cortex.

Post-stimulus time histograms for a putative fast-spiking interneuron in the visual cortex of an anesthetized PV-Cre mouse injected with AAV5-FLEX-Jaws virus (35 mW/mm^2 at 593 nm using a 200 μm fiber) undergoing visual stimulation (*left*) and Jaws-mediated inhibition of a visually evoked response (*right*).

It has been noted in previous publications that a rebound burst of action potentials is common after illumination of halorhodopsin-[36-40] or archaerhodopsin-expressing[36, 40-42] cells, which respectively pump chloride inward and protons outward (Figure 2.15a,b). A variety of possible mechanisms have been proposed, including hyperpolarization-activated I_h currents[35, 38, 39] or changes in Cl- reversal potential due to intracellular Cl- accumulation[43]. We similarly observed post-illumination rebound in Jaws-, eNpHR3.0-, and ArchT-transduced neurons (Figure 2.15c), and Jaws presented higher effects than eNpHR3.0 or ArchT (Figure 2.16a; n = 8-32 units; $p < 0.05$, ANOVA with Newman-Keuls post-hoc test). We attempted to ameliorate this by gradually ramping down illumination over a duration of 200-1000 ms, and found that the mean rebound instantaneous firing rate dropped significantly from 52 ± 12 Hz to 23 ± 6 Hz (n = 16 units; $p < 0.01$, paired t-test), suggesting that sculpting of light pulses may enable rebound reduction. Notably, the rebound delay also significantly lengthened from 18 ± 6 ms to 76 ± 6 ms (n = 16 units; $p < 0.001$, paired t-test) and became more temporally dispersed (Figure 2.16). Like all previous silencers, Jaws does exhibit post-illumination rebound, which likely has implications for careful experiment design comparable to those for prior silencers such as eNpHR3.0. Further attention to light pulse shape may be additionally merited as a way to reduce rebound for potentially all optogenetic silencers.

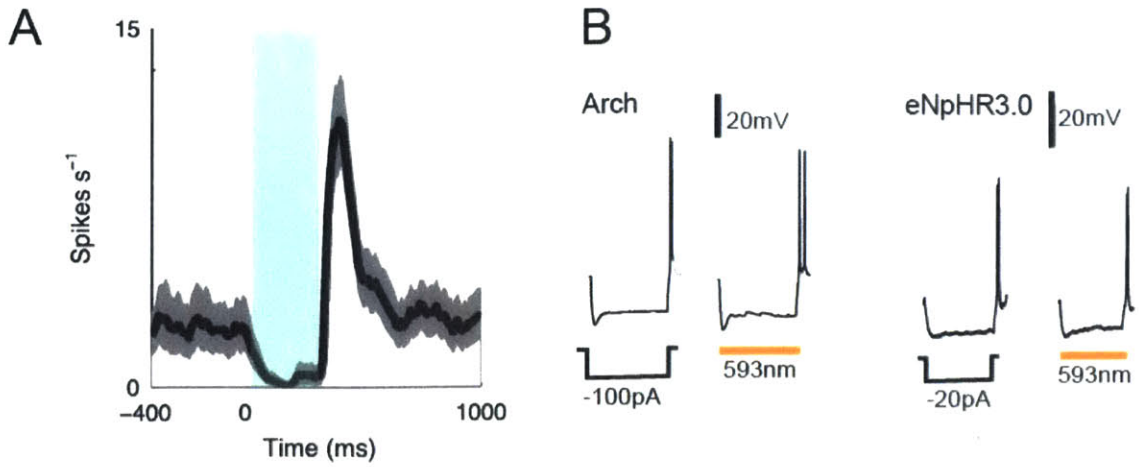

Figure 2.15 - Rebound firing can occur post-inhibition for all inhibitory opsins independent of ion conductance.

Examples of rebound across different opsin classes. **(a)** Post-illumination rebound in a corticostriatal Arch-expressing neuron in an awake rodent, as measured via extracellular tetrode recording, modified from Znamenskiy *et al*[44]. **(b)** Post-hyperpolarization rebound in Arch- or eNpHR3.0-expressing neurons when hyperpolarized either optically or electrically as measured via slice, modified from Madisen *et al*[36].

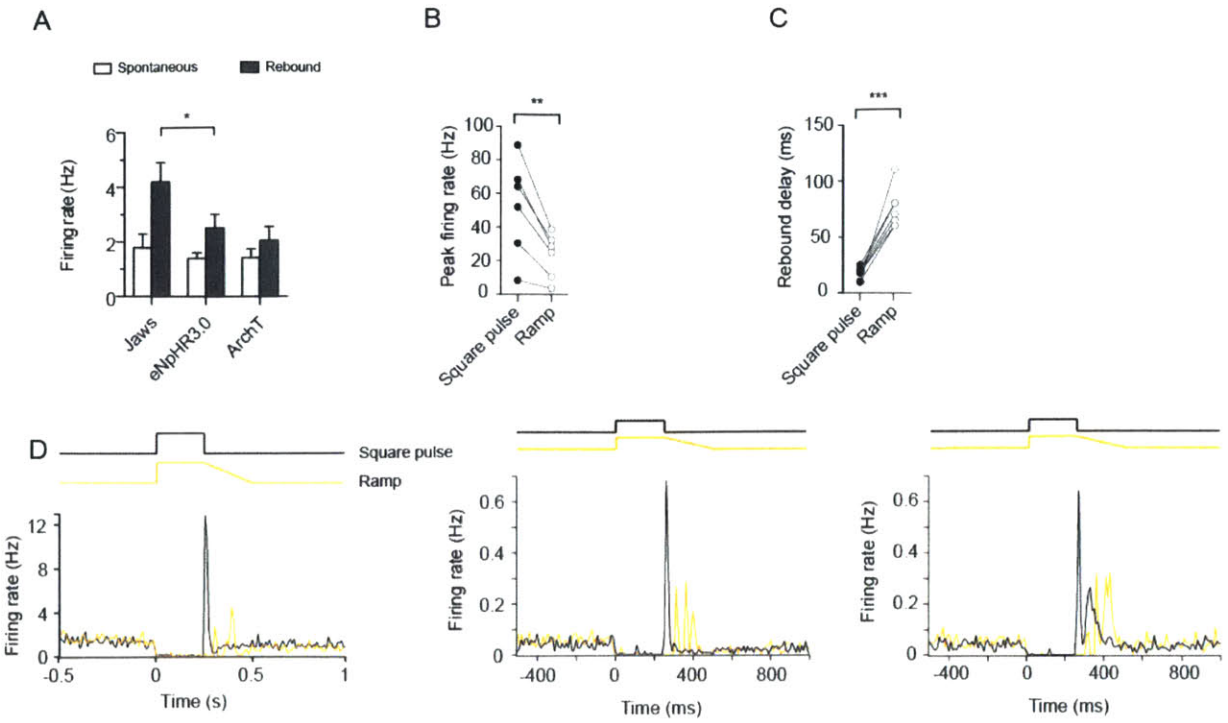

Figure 2.16 - Light pulse shape affects intensity and duration of post-illumination rebound.

(a) Comparison of spontaneous and immediately post-illumination firing rates for Jaws, eNpHR3.0 and ArchT (n = 32 units from 4 mice for eNpHR3.0, n = 21 units from 3 mice for ArchT, n = 5 units for Jaws from 2 mice; $P < 0.05$ for Jaws versus eNpHR3.0). **(b,c)** Comparison of peak firing rates and rebound delay rates for step versus ramped illumination (n = 16 units from 3 mice). Values throughout are mean ± s.e.m. For a-c, *P < 0.05, **P < 0.01, ***P < 0.001. ANOVAs with Newman-Keuls post hoc tests in a; paired t-tests in b,c. **(d)** Post-stimulus time histogram for a standard step light pulse (black line) versus ramped illumination (yellow line), for three spontaneously firing visual cortex neurons.

Red light performance of Jaws

We next assessed Jaws' red-light properties via whole-cell patch-clamp recordings in acute cortical slice as well as extracellular recordings in awake, head-fixed mice. We injected adeno-associated virus (AAV; serotype 8) encoding Jaws under the CaMKII or human synapsin promoters, or Jaws-ER2 under the human synapsin promoter, into motor cortex and observed robust red light photocurrents, hyperpolarization, and neural silencing (Figure 2.17a-e) with ~95% reduction of neural activity achievable in neurons illuminated by a 200 μm fiber (130

mW/mm^2 fiber tip irradiance of 635 nm; Figure 2.18). Jaws' kinetic properties were comparable to those of other silencers (Figure 2.9e-f, Figure 2.17f), and its expression did not alter basal cell properties in cultured cortical neurons (Figure 2.9g), or in cortical or dentate granule neurons in acute brain slice (Figure 2.17g, Figure 2.19).

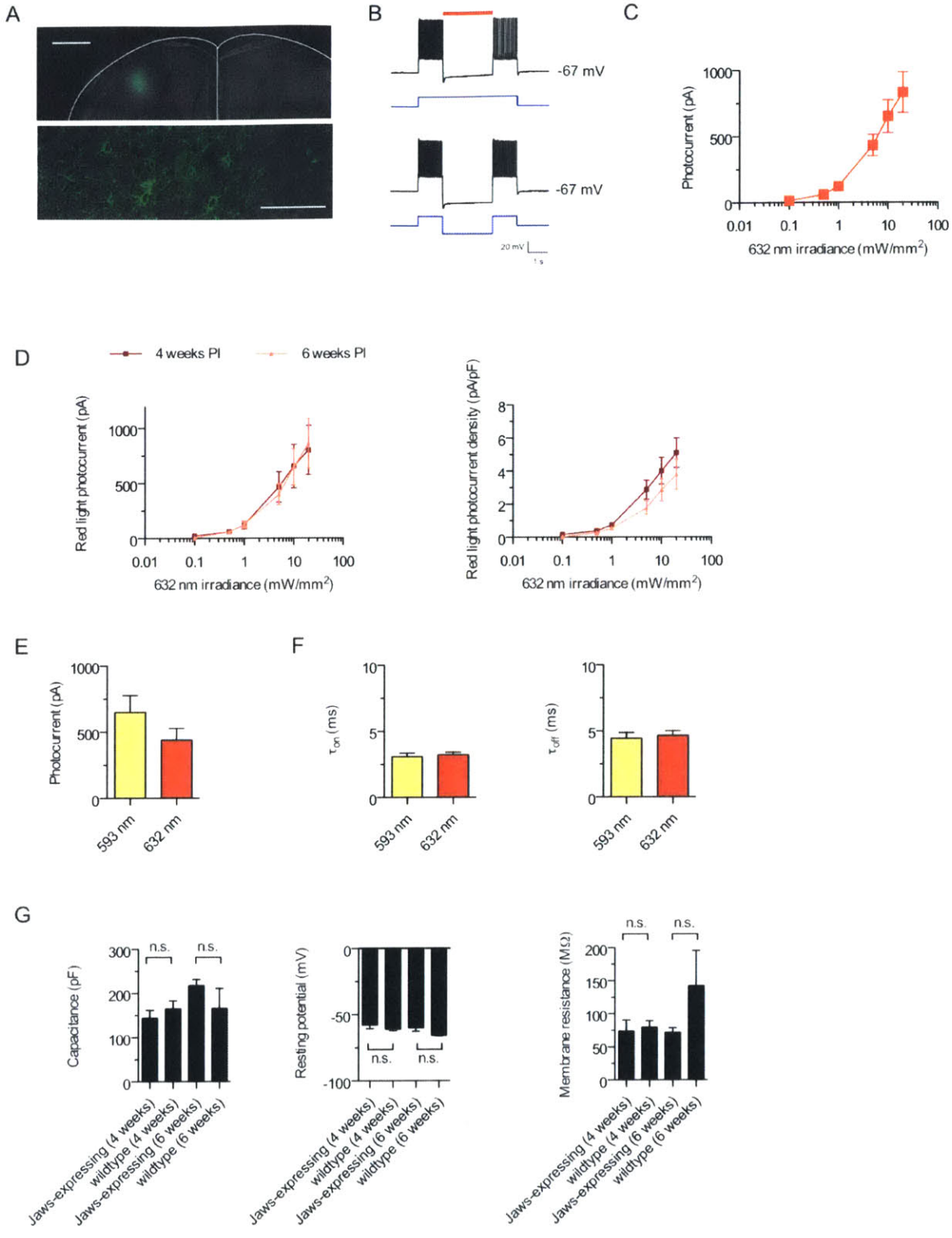

Figure 2.17 - Ex vivo characterization of Jaws in acute motor cortex slice.

(a) Confocal fluorescence images from Jaws-GFP expressing motor

cortex, 6 weeks post-injection. Scale bar, 1 mm (top) or 100 μm (bottom). **(b)** Representative current-clamp recording of Jaws-expressing neuron undergoing optically-evoked (top, 632 nm, 5 mW/mm^2) or electrically-evoked (bottom, 700 pA) hyperpolarization in acute cortical slice 6 weeks post-injection. **(c)** Quantification of Jaws photocurrents as a function of red light irradiance in acute slice (n = 16 cells). **(d)** Jaws photocurrents (left) and photocurrent densities (right), measured as a function of red light irradiance, were the same at 4 and 6 weeks post-injection in acute slice (n = 8 cells for each timepoint). **(e)** Jaws yellow and red light photocurrents (n = 16 cells, 5 mW/mm^2, 593 or 632 nm). **(f)** Comparison of Jaws on-kinetics (left) and off-kinetics (right) using red or yellow illumination (n = 16 cells for each, 5 mW/mm^2 593 or 632 nm). **(g)** Neuron properties upon Jaws expression at 4 (n = 9 cells) or 6 weeks (n = 10 cells) post-injection in acute cortical slice as compared against non-opsin-expressing neurons (n = 5 cells at 4 weeks, n = 3 cells at 6 weeks), including cell membrane capacitance (left), resting potential (middle), and cell input resistance (right). Values are means ± standard error. Statistics for panels d: * $P < 0.05$. Panel d was an ANOVA with Dunnett's post hoc test using non-opsin expressing neurons as the reference.

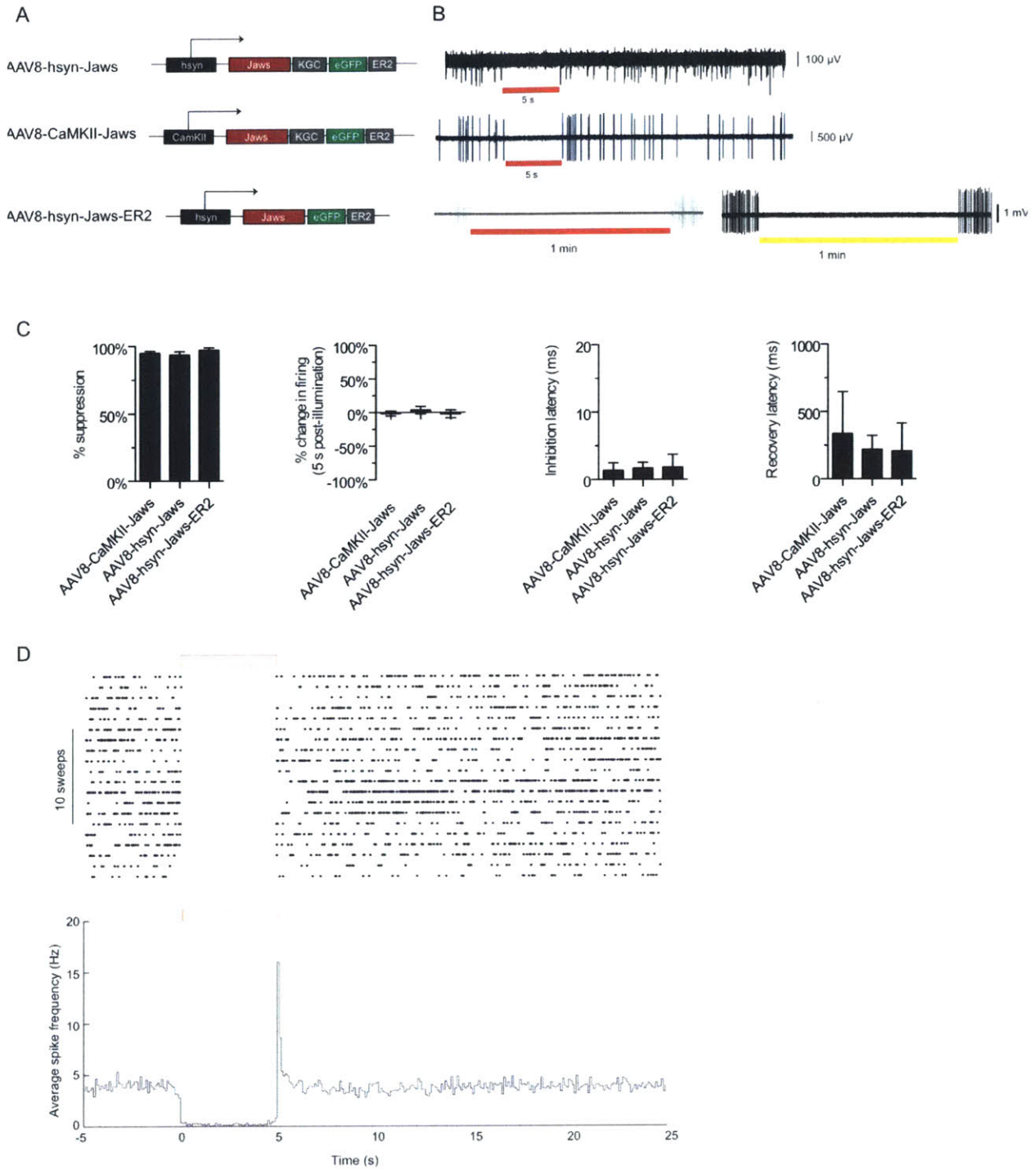

Figure 2.18 - Demonstration of Jaws functionality in awake mouse cortex, using invasive 200 um fibers.

Gene schematic **(a)** and corresponding representative glass pipette extracellular recording **(b)** of different Jaws variants expressed in cortical neurons 6 weeks post-injection in awake mice undergoing red or yellow light illumination (637 or 593 nm, ~130 mW/mm^2 out the fiber tip). **(c)**

Comparison of different Jaws variants 1-3 months post-injection, as measured by suppression of spontaneous firing, change in firing 5-seconds post-illumination, inhibition latency, and recovery latency (n = 14 units for AAV8-CaMKII-Jaws, n = 17 units for AAV8-hsyn-Jaws, n = 6 units for AAV8-Jaws-ER2). **(d)** Spike rasters recorded from a representative neuron (top), and population average (bottom; n = 31 units) of instantaneous firing rate in neurons showing any degree of light-induced suppression, recorded in awake headfixed mice 4-8 weeks after injection of AAV8 encoding Jaws under either the CaMKII (n = 14 units) or synapsin promoter (n = 17 units; black line, mean; grey lines, mean ± s.e.). Values are means ± standard error.

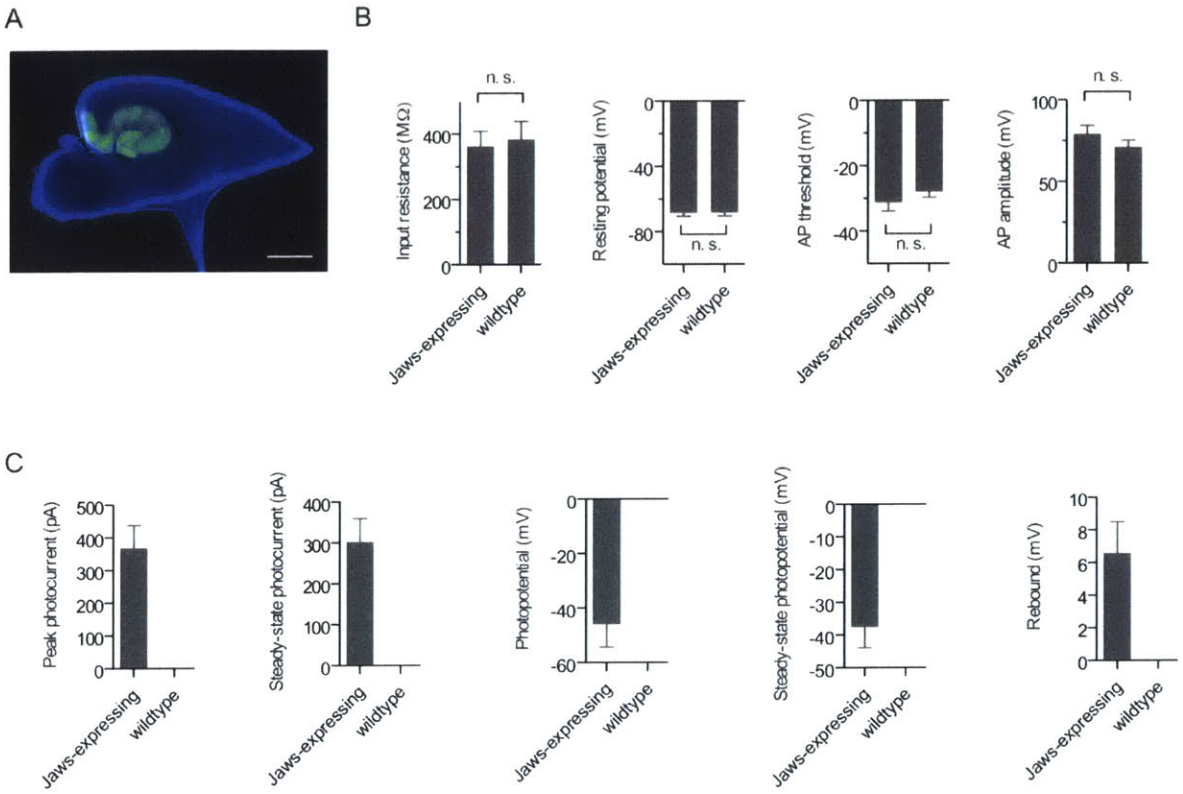

Figure 2.19 - Ex vivo characterization of Jaws-expressing dentate granule cells in acute hippocampal slice

(a) Epifluorescence image from Jaws-GFP expressing hippocampus, 4 weeks post-injection. Blue indicates DAPI staining, green indicates GFP fluorescence. Scale bar, 1 mm. **(b)** Physiological properties upon opsin expression at 4 weeks post-injection in dentate granule cells, including cell input resistance, resting potential, electrically evoked action potential threshold, electrically evoked action potential amplitude. **(c)** Physiological properties for Jaws-expressing and wildtype dentate granule cells upon red

light illumination, including peak and steady-state photocurrent, peak and steady- state photopotential, and post-illumination rebound voltages. n = 12 for Jaws-positive cells, n = 15 for wildtype cells, throughout this panel. Illumination was 1 second at 68 mW/mm^2, 625 nm. Values are means ± standard error. Statistics for panel b: * $P < 0.05$. Panel b was a Student's t-test.

Having established Jaws as a potent red-light-drivable inhibitor, I next assessed its *in vivo* performance compared to eNpHR3.0. I did titer-matched injections of 2×10^9 viral particles of AAV8-synapsin-Jaws, AAV8-synapsin-Jaws-ER2 or AAV8-synapsin-eNpHR3.0 into mouse motor cortex (Figure 2.20b) and performed awake head-fixed recordings to characterize each hyperpolarizer over different red (637 nm) light powers (Figure 2.20a,c). Yellow light (593 nm) was used as a positive control to identify opsin-expressing neurons, due to its proximity to both Jaws' and eNpHR3.0's spectral peaks, and we conducted paired recordings of individual opsin-expressing neurons to assess their performance under different wavelengths (Figure 2.20d). As expected, both Jaws variants robustly inhibited spontaneous neural activity when illuminated with either red (88.8 ± 15.9% inhibition for Jaws, 97.2 ± 3.9% inhibition for Jaws-ER2) or yellow wavelengths (94.2 ± 9.3% inhibition for Jaws, 99.0 ± 1.6% inhibition for Jaws-ER2), while eNpHR3.0 red-light inhibition dropped significantly to only 27.5 ± 30.3% relative to its peak yellow-light performance of 76.1 ± 11.1% inhibition (Figure 2.20d; n = 5-6 units, $P < 0.05$), and we found these red-light results to hold over a range of firing rates (Figure 2.20e; n = 5-8 units for each opsin).

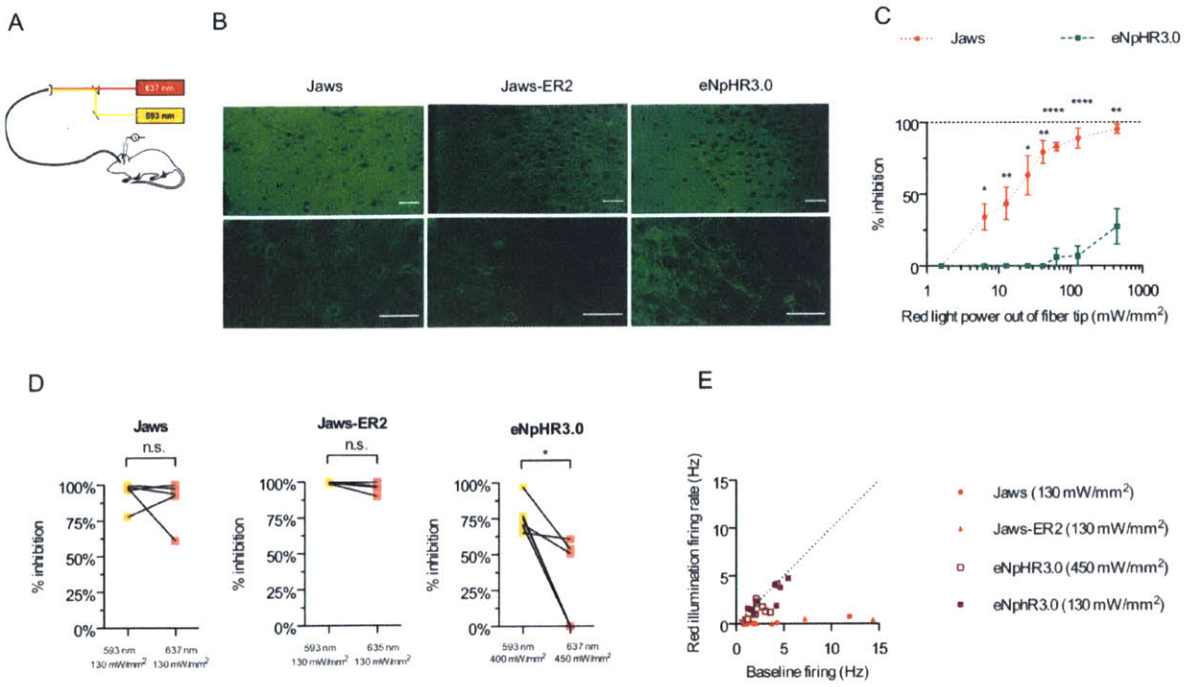

Figure 2.20 - Comparison of Jaws against eNpHR3.0

(a) Experimental schematic for side-by-side comparisons in awake, head-fixed rodent cortex, switching between 637 nm or 593 nm illumination out of a single optical fiber. **(b)** Confocal fluorescence images from Jaws-GFP-, Jaws-GFP-ER2- or eNpHR3.0- expressing motor cortex. Scale bar 100 μm. **(c)** Side-by-side comparison of red light-driven inhibition of spontaneous neural activity at different light powers in motor cortex (n = 6 units for each opsin; 637 nm). **(d)** Red-light inhibition was equivalent to yellow-light inhibition for Jaws (n = 5 units) and Jaws-ER2 (n = 6 units), but substantially less potent for eNpHR3.0 (n = 6 units). **(e)** Red light efficaciously inhibited Jaws- (n = 5 units) and Jaws-ER2- (n = 6 units) but not eNpHR3.0-expressing neurons (n = 8 units) over a range of firing rates. Values throughout are mean + standard error. Statistics for panels c and d: * $P < 0.05$, ** $P < 0.01$, *** $P < 0.001$, **** $P < 0.0001$. Panel c was an unpaired T-test, panel d was a paired T-test.

Non-invasive optogenetic inhibition

Having demonstrated Jaws' efficacy as a red-light-drivable reagent in a variety of contexts, we next sought to determine its potency as a non-invasive and long-distance neural silencer. Using red illumination (Figure 2.21a), we found we could transdurally inhibit neurons in the medial prefrontal cortex (mPFC) of a mouse, with a 86 ± 13% decrease (mean ± standard deviation) in firing for neurons showing suppression (n = 66 units across 2 anesthetized mice;

Figure 2.21d). Using a similar strategy, I successfully inhibited neurons in the awake mouse cortex by delivering red light transcranially through the intact skull (635 nm, 10 mW/mm^2 out of a 1500 μm fiber tip; Figure 2.21a,b) to regions 1-3 mm below the brain's surface (Figure 2.21c,e,f). Transcranial silencing in the motor, somatosensory, insular and piriform cortices was efficient, with a 92 ± 14% decrease in firing for neurons showing suppression (mean ± standard deviation; n = 13 units across 7 mice; n = 9 neurons showed no change, and n = 3 neurons showed an increase in activity; Figure 2.21f).

The efficacy of transcranial optogenetic silencing was similar across several millimeters of the awake mouse brain (Figure 2.21g) and over a variety of baseline firing rates (Figure 2.21h). To directly address the possibility that opsin-expressing apical dendrites near the brain's surface were being hyperpolarized, resulting in somatic or downstream network inhibition, I next conducted paired recordings using a standard acutely inserted 200 μm fiber as a positive control for transcranial illumination outside the mouse's intact skull. Illumination from a 200 μm fiber has been shown to fall off rapidly within a few hundred microns of the fiber tip[20, 45], and the likelihood of optogenetic inhibition has been similarly demonstrated to fall off over a similar distance[41]. My paired recordings revealed similar degrees of suppression over a range of 1-3 mm below the brain's surface (Figure 2.21i,j). From this, I conclude Jaws is capable of non-invasive optogenetic silencing comparable to the current standard of invasive optical delivery.

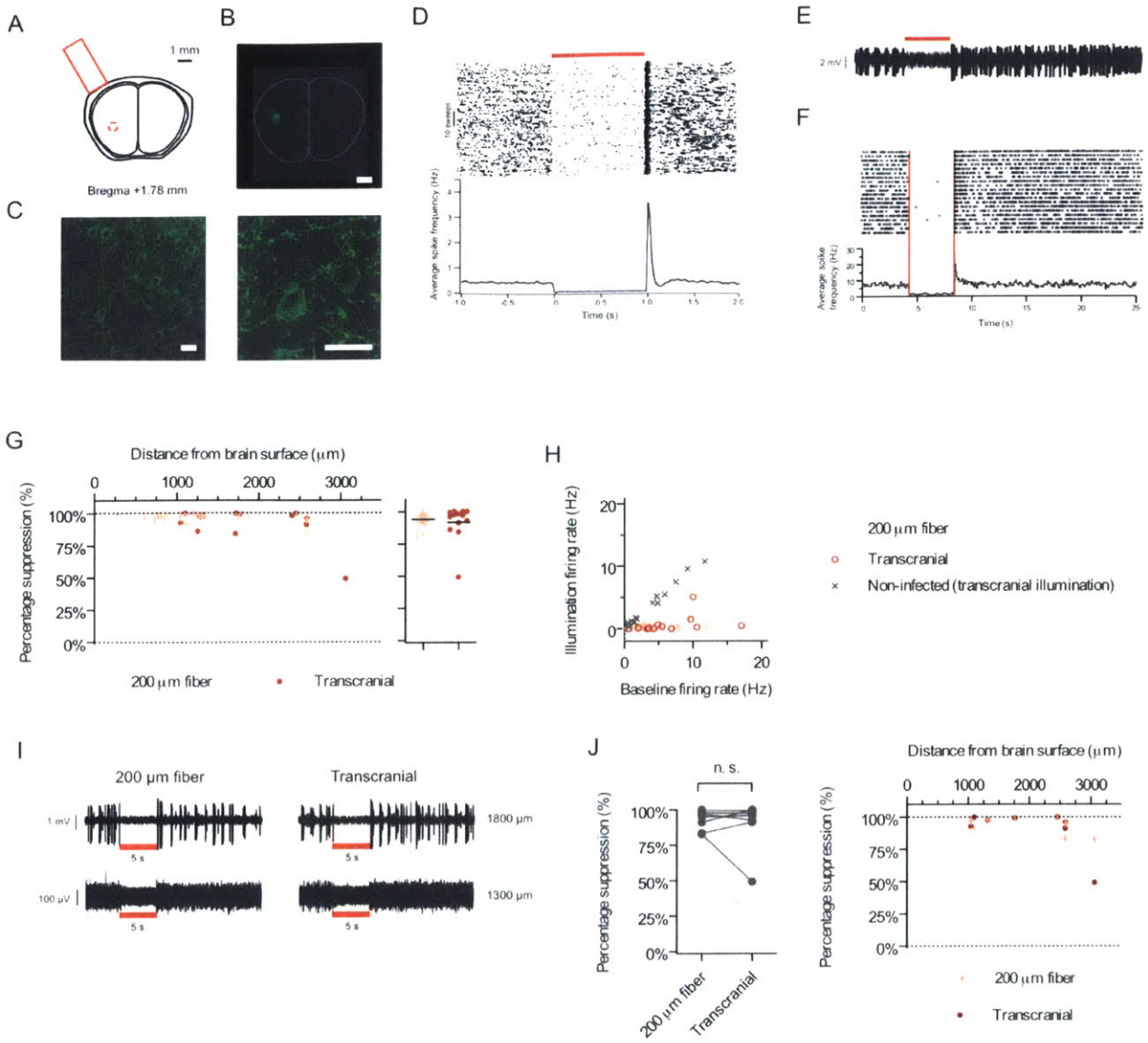

Figure 2.21 - Non-invasive red-light inhibition of neural activity.

(a) Schematic of non-invasive red light delivery through the intact skull. (**b-c)** Fluorescence images from mouse insular cortex (**b**; scale bar 1 mm) and motor cortex (**c**; scale bar 25 μm) 6 weeks post-injection with AAV8-synapsin-Jaws virus. **(d)** Raster plot (top) and population average (bottom) of transdural inhibition of neurons in the medial prefrontal cortex (mPFC) of anesthetized mice, showing any degree of light-induced suppression 6-8 weeks after injection with AAV8-synapsin Jaws virus (n = 26 units; 1 s pulse, 25 mW/mm^2 fiber tip irradiance, 635 nm). **(e)** Representative glass pipette extracellular recording of a transcranially-illuminated cortical neuron 2700 μm below brain surface in an awake mouse (10 mW/mm^2 fiber tip irradiance, 635 nm; 4 weeks post-injection with AAV8-synapsin-Jaws virus). **(f)** Spike rasters taken from a representative neuron (top), and population average (bottom; n = 13 units) of instantaneous firing rate in neurons from awake mice undergoing transcranial light-induced

suppression 4-8 weeks post-injection with AAV8-synapsin-Jaws virus (5 s pulse, 10 mW/mm^2 635 nm fiber tip irradiance; black line, mean; grey lines, mean ± s.e.). **(g)** Percent reduction in neural activity for neurons recorded at different depths in awake mouse brain, 6-8 weeks post-injection with AAV8-synapsin virus. Red light delivered via traditional 200 μm fiber (n = 37 units) or transcranially (n = 13 units). **(h)** Firing rate averaged over the illumination period vs. baseline firing rate for neurons recorded in awake mouse brain (n = 14 units). **(i)** Representative extracellular recordings of neurons 1800 μm (*top*) and 1300 μm (*bottom*) below the awake brain surface undergoing illumination via a 200 μm fiber (~130 mW/mm^2; 635 nm) 500 μm above the electrode tip (*left*) or transcranially (*right*) through the intact skull (~10 mW/mm^2; 635 nm), recorded 8 weeks post-injection with AAV8-synapsin-Jaws virus. **(j)** Transcranial and 200 μm fiber illumination were equally efficacious (*left*) in inhibiting neurons (n = 8 units) over depths of up to 3 mm (*right*). Values are means ± standard error. Panel **j** was a paired T-test.

Discussion

We here report Jaws, a novel red light sensitive opsin with the most red-shifted known spectrum of any optogenetic silencer. Jaws enables efficacious transcranial silencing of neural activity in awake mouse brain in response to red light, with a similar efficacy to standard invasive light delivery with a 200 μm optical fiber. Additionally, Jaws enables significantly more silencing of stimulus evoked neural activity than possible with previous halorhodopsins. Finally, it restores photosensory responses in RP retinas in a fashion achieving greater spike rates than previously achievable and with a more naturalistic frequency range, which may be important for retinal neural coding. Thus, Jaws has demonstrated utility across a wide variety of key neuroscience applications, both basic-science and pre-clinical. We also demonstrate that light pulse sculpting can ameliorate the amplitude of post-inhibition rebound that has been widely reported for halorhodopsins.

It has been previously well established that optical penetrance of mammalian tissues in the red to near-infrared (600-1000 nm) wavelengths is better than that of bluer wavelengths, due to substantially reduced absorption from hemoglobin, myoglobin, and lipid. Despite this better red light penetrance, it is still important to note that myelination may affect optical propagation in neural tissue and should therefore be taken into account given the experimental system in question[42, 43]. The relative inexpensiveness and stability of red light sources may additionally be

of use to experimental investigators, as well as the ability to avoid potentially confounding experimental visual artifacts, since mouse visual pigments peak at approximately 380 nm (UV cones) and 500 nm (green cones) but mice have poor vision above 600 nm[46, 47].

As others have reported, we observed a small number of neurons across multiple *in vivo* experiments which increased firing during optical illumination delivered either transcranially or from a 200 μm fiber, most likely due to network inhibition from upstream neurons[3, 48, 49]. It is important to note it is not possible to non-invasively illuminate only deep volumes with our experimental setup without also targeting surface and intermediate layers. We therefore cannot explicitly rule out that the observed non-invasive results were the result of indirect network activity or apical dendritic illumination: a caveat for any *in vivo* investigation of noninvasive optogenetics. However, the robust photocurrents we observed both *in vitro* and in acute slice over a range of irradiances are consistent with and corroborate the functional inhibition we observed in awake mice. We therefore believe our paired recordings comparing transcranial illumination with local 200 μm fiber illumination are highly suggestive of direct inhibition.

In scenarios where brain integrity is mandatory, non-invasive optogenetics may be invaluable in helping to prevent the many known issues associated with implants[8-10]. The efficacy and simplicity of transcranial inhibition could be helpful for chronic optogenetic experiments involving long-term imaging[50, 51], longitudinal monitoring of disease progression[52], or developmental studies, during which developmental changes in brain structures might preclude the chronic implantation of a fiber at a given target[53]. In principle, the need for brain surgery could be eliminated altogether by using transcranial illumination with a Jaws-expressing transgenic mouse strain[36]. Neural inhibition in animals with large brains, such as the rhesus macaque, which recently has been demonstrated to undergo optogenetic perturbation of behavior with optogenetic stimulation or inhibition of neurons[54, 55], may particularly benefit from the usage of Jaws. Finally, with increasing interest in the potential for therapeutic optogenetics[30, 56], the opsin described here may prove useful in the context of the many prototype therapies being explored.

Experimental Methods

Animal procedures

All procedures were in accordance with the National Institute for Laboratory Animal Research Guide for the Care and Use of Laboratory Animals and approved by the Boston University Institute Institutional Care and Use Committee, the Massachusetts Institute of Technology Committee on Animal Care, the Yale University Institute Institutional Care and Use Committee, or the Swiss Veterinary Office. All mice in this study were housed 3-5 per cage, maintained with a 12-hr light-dark cycle, and had no previous experimental history.

Plasmid construction and site directed mutagenesis.

Opsin genes were mammalian codon-optimized and synthesized (Genscript). Point mutants were generated using the QuikChange kit (Stratagene) on the opsin-GFP fusion cassette in the pEGFP-N3 backbone (Invitrogen). Cultured neuron experiments were carried out by subcloning all genes into a lentiviral backbone containing the CaMKII promoter and with a C-terminal GFP fusion. AAV vectors were constructed by subcloning opsin-GFP cassettes into AAV vectors behind the CaMKII, CAG, or synapsin promoters. For cone photoreceptor delivery, opsin-GFP cassettes were subcloned into pAAV2-mCAR-EGFP, replacing the EGFP gene[30].

In vitro culture, transfection, and imaging.

Hippocampal neuron cultures were prepared from postnatal day 0 or 1 Swiss Webster mice (Taconic), plated at a density of 16,000-20,000 per glass coverslip coated with Matrigel (BD Biosciences)[57], and transfected at 3-5 days in vitro (DIV) using calcium phosphate (Invitrogen)[1, 3]. GFP fluorescence was used to identify transfected neurons for the cruxhalorhodopsin screen and HEK293FT characterizations; all other experiments were conducted by cotransfecting with an independent tdtomato plasmid, in which case neurons were picked based solely on tdtomato fluorescence.

Whole cell patch clamp recordings were made using a Multiclamp 700B, a Digidata 1440, and a PC running pClamp (Molecular Devices). Neurons were recorded 14-24 days DIV, bathed in room temperature Tyrode containing 125 mM NaCl, 2 mM KCl, 3 mM $CaCl_2$, 1 mM $MgCl_2$, 10 mM HEPES, 30 mM glucose, 0.01 mM NBQX and 0.01 mM GABAzine (Sigma) at pH 7.3

(NaOH-adjusted) and osmolarity 300 mOsm (sucrose-adjusted). HEK cells were bathed in an identical Tyrode bath solution lacking GABAzine and NBQX. No all-*trans*-retinal was supplemented for any recordings. 3-9 MΩ borosilicate glass pipettes (Warner Instruments) were pulled with a P-97 micropipette puller (Sutter Instruments) and filled with a solution containing (in mM): 125 K-gluconate, 8 NaCl, 0.1 $CaCl_2$, 0.6 MgCl2, 1 EGTA, 10 HEPES, 4 Mg-ATP, and 0.4 Na-GTP at pH 7.3 (KOH-adjusted) and osmolarity 298 mOsm (sucrose-adjusted).

Ion selectivity tests were carried out in chloride-free recording solution containing (in mM): 125 Na-Gluconate, 2 K-Gluconate, 3 CaSO4, 1 MgSO4, 10 HEPES, 30 glucose, at pH 7.3 (NaOH-adjusted), and with 305-310 mOsm (sucrose-adjusted) and using intracellular solution containing (in mM): 125 K-Gluconate, 8 Na-Gluconate, 0.1 CaSO4, 0.6 MgSO4, 1 EGTA, 10 HEPES, 4 Mg-ATP, 0.4 Na-GTP, pH 7.3 (KOH-adjusted), 295-300 mOsm (sucrose-adjusted).

No action spectrum data was gathered from cells voltage-clamped at -65 mV with a leak current greater than -200 pA, or with a resting membrane potential more positive than -45 mV in current-clamp mode. Access resistance was 5-30 MΩ. Resting membrane potential was ~-65 mV for neurons and ~-30 mV for HEK 293FT cells in current-clamp recording. All parameters were monitored throughout recording.

All *in vitro* action spectra, photocurrent, and voltage data were taken with a Leica DMI6000B microscope. Action spectra were taken with a monochromator (Till Photonics Polychrome V, 15 nm bandwidth centered around each value). Spectra for a given cell were taken by averaging red-to-UV (685 to 387 nm) and UV-to-red (387 to 685 nm) spectra, to eliminate history dependence. Photon fluxes for all wavelengths were ~3.0×10^{21} photons/s/m^2 (0.756 mW/mm^2 at 670 nm). Normalized action spectra were obtained by dividing the averaged photocurrent data by the highest observed data point.

Trafficking *in vitro* photocurrents were taken with a DG-4 optical switch with 300 W xenon lamp (Sutter Instruments), delivered with a 575 ± 25 nm bandpass filter (Chroma). All other *in vitro* photocurrents were measured using 470 nm, 530 nm, or 625 nm LEDs (Thorlabs). LED spectra were bandpass filtered with the following (Semrock): 530 nm LED with 543 nm ± 11 nm filter or 625 nm LED with 632 nm ± 11 nm. All light powers were measured out of the objective lens with a PM200B photodetector (Thorlabs). Data was analyzed using Clampfit (Molecular Devices) and MATLAB (Mathworks, Inc.)

AAV preparation

The AAV particles used for cone photoreceptor targeting were produced in the Roska laboratory[58], with titers between 5.2 x 10^{11} and 6.8 x 10^{12} GC/ml. All other AAV constructs were produced by the University of North Carolina Chapel Hill Vector Core at a titer of ~6 x 10^{12} cfu/mL. All viral dilutions were carried out in phosphate buffered saline (PBS; Life Technologies).

In vivo rodent electrophysiology

Injections for glass-pipette electrophysiology were made under isoflurane anesthesia and buprenorphine analgesia, and 1 μL AAV was injected through a craniotomy made in the mouse skull, into the motor cortex (1.78 mm anterior, 1.5 mm lateral, and 1.75 mm deep, relative to bregma), or the piriform, insular, or somatosensory/motor cortices (1.78 mm anterior, 2.0 mm lateral, and respectively 4.0, 3.0, and 2.0 mm deep, relative to bregma) of 5-9 week old female C57BL6 mice. Comparisons for eNpHR3.0 and Jaws were carried out by injecting 2 x 10^9 viral particles in 1 uL of an AAV-PBS mixture into motor cortex.

All viruses were injected at a rate of 0.15 μl/min through a 34-gauge injection needle, after which the needle was allowed to rest at the injection site for 10 minutes to allow viral diffusion. The craniotomy was marked with Examix NDS (GC America), headplates were affixed to the skull with skull screws (JL Morris), and the craniotomy and headplate were covered with dental cement (C&B Metabond).

Expression of Jaws targeted populations of neurons in the prefrontal cortex was achieved by intracranial injection of AAV8-hSyn-Jaws in P60-120 male C57BL/6 mice. Opsins were expressed in excitatory neurons in primary visual cortex by injecting AAV5-CAG-FLEX viruses into Emx1-Cre or PV-Cre mice. Mice were anesthetized with 1.5% isoflurane and virus was injected at 0.1μl/min; mice were given 4-5 weeks for recovery.

Extracellular recordings to measure inhibition of spontaneous neural activity were made in the cortex of headfixed awake mice 1-2 months after virus injection, using 3-10 MΩ saline-filled glass microelectrodes containing silver/silver-chloride electrodes[1, 3]. Signals were amplified with a Multiclamp 700B and digitized with a Digidata 1440, using pClamp software (Molecular Devices). A 635 nm, 200 mW laser (Shanghai Laser Optics and Century) was coupled to a 200 micron-diameter optical fiber. An optical fiber was attached to the recording

glass electrode, with the tip of the fiber 600 μm laterally from and 500 ± 50 μm above the tip of the electrode, and guided into the brain with a Sutter manipulator. Transcranial recordings were carried out with a 635 nm red laser coupled to a 1500 μm-diameter optical fiber, and the recording electrode was additionally attached to a 200 μm-diameter fiber, coupled to a different 635 nm laser, as described above. Comparisons between Jaws and eNpHR3.0 were carried out using a 593 nm yellow laser (Shanghai Laser Optics and Century) and a 637 nm red laser (Coherent Lasers), which were both coupled into the same 200 micron-diameter optical fiber. All lasers were controlled via Digidata-generated TTL pulses. Light powers were measured with an integrating sphere (S142C, Thorlabs) and PM200B photodetector (Thorlabs).

Extracellular recordings to measure suppression of evoked neural activity were conducted in mice anesthetized with 0.2-0.4% isoflurane and 0.8 mg/kg fentanyl. Extracellular recordings were performed with moveable arrays of tetrodes (Thomas Recording) with a 250 μm inter-electrode distance. Data acquisition at 40kHz and online spike identification by waveform analysis used the Cheetah data acquisition software (Neuralynx). An optical fiber (200 or 1500 μm) was placed on the dura next to the electrode array and connected to either a 593 nm or a 635 nm laser. To activate Jaws, 1 s pulses of light were given at 0.1 Hz at varying light intensities (10, 25, 50, or 75 mW/mm^2). Visually evoked responses were driven by randomized sequences of drifting gratings at 16 orientations and a spatial frequency of 0.05 cycles/degree on a background of mean luminance. The size of the visual stimulus was optimized for the receptive fields of the recorded population. Response measurements for each neuron were taken at the optimal orientation as identified by post-hoc analysis.

Data was analyzed using MATLAB (Mathworks, Inc.)[1, 3]. Briefly, spikes were detected and sorted offline using Offline Sorter (Plexon) or waveform template matching and principal component analysis discrimination (KlustaKwik and custom-written Igor software, J. Cardin[59]). Only clusters with clear refractory periods in the autocorrelogram, indicating a single unit source, were used for further analysis. As a further precaution against overrepresentation of the same unit, cross correlograms were run for every pair of identified units in a set. Clusters that were not easily separable were discarded. Light modulated units were identified by performing a paired t-test between the 1 or 5 second illumination period against the baseline firing period of the same time duration immediately before illumination, thresholding at $p < 0.05$. The degree of suppression by Jaws activation was calculated for each cell by dividing the mean firing rate

during the light stimulus by the mean baseline firing rate during the same time duration prior to light stimulation onset. Rebound firing rates were calculated within a window immediately after the cessation of the light stimulus. The width of the window was determined as the duration for which firing rates were elevated > 3 standard deviations of the mean spontaneous firing rate.

Light onset latency to inhibition was calculated by sweeping a 20 ms sliding window to identify the earliest 20 ms period deviating from the baseline firing rate, as assessed by performing a paired t-test for the firing rate during each window vs. during the baseline period, averaged across all trials for each neuron. The time for after-light suppression to recover back to baseline was calculated by taking the median of all trials, due to a non-parametric distribution.

Ex vivo slice electrophysiology

For whole-cell patch clamp recordings in motor cortex, coronal 300 μm brain slices were prepared after four or six weeks after viral injection of AAV8-hsyn-Jaws. Male C57BL6 mice were deeply anaesthetized with sodium pentobarbital (200 mg/kg) then transcardially perfused with 15-20 ml of ice-cold modified artificial cerebrospinal fluid (ACSF; composition in mM: NaCl 87, KCl 2.5, NaH2PO4*H2O 1.3, MgCl2*6H2O 7, NaHCO3 25, sucrose 75, ascorbate 5, CaCl2*2H2O 0.5, in ddH2O; osmolarity 320-330 mOsm, pH 7.30-7.40) saturated with carbogen gas (95% oxygen, 5% carbon dioxide). The brain was rapidly removed from the cranial cavity and then sectioned using a vibrating-blade microtome (VT1000S, Leica). Slices were allowed to recover for at least 90 min in a holding chamber containing ACSF (composition in mM: NaCl 126, KCl 2.5; NaH_2PO4*H_2O 1.25, $MgCl_2*6H2O$ 1, $NaHCO_3$ 26, glucose 10, $CaCl_2*2H_2O$ 2.4, in ddH_2O; osmolarity 299-301 mOsm; pH 7.35-7.45) saturated with carbogen gas at 32 °C before being transferred to the recording chamber for electrophysiology. Once in the recording chamber, slices were continuously perfused at a rate of 2 ml/min with fully oxygenated ACSF at 32 °C with added Picrotoxin (100 μM), NBQX (20 μM; Sigma), and AP5 (50 μM; Tocris) to block fast synaptic transmission within the slice.

For whole-cell patch clamp recordings of dentate granule cells, four 9-10 week old male C57BL6 mice were injected with AAV8-CaMKII-Jaws under deep isoflurane anesthesia. 0.5 ul AAV was delivered twice at two locations into the hippocampus (3.2 mm posterior, 3.1 mm lateral, and respectively 2.3 and 2.7 mm deep, relative to bregma) at 100 ul/min with a 34-gauge needle attached to a Hamilton 5 ul syringe, and the needle was left in place for 3 min to allow

viral diffusion. Four weeks post-injection, mice were killed by decapitation and horizontal 300 μm brain sections were prepared on a Leica VT1200 S vibratome. Sucrose based aCSF (composition in mM: sucrose 75, NaCl 67, $NaHCO_3$ 26, glucose 25, KCl 2.5, NaH_2PO_4 1.25, $CaCl_2$ 0.5, $MgCl_2$ 7; pH 7.4, osmolarity 305-310 mOsm) was used for cutting (at 4°C) and subsequent storage of slices (32°C for 20-30 min, then maintained at room temperature, 23.0 - 23.5°C). After >1 hr incubation, slices were transferred to a submerged recording chamber constantly perfused at 2 ml/min with aCSF (in mM; NaCl 119, $NaHCO_3$ 1.24, glucose 10, KCl 2.5, NaH_2PO_4 1.24, $CaCl_2$ 2.5, $MgCl_2$ 1.3, pH 7.4, 295 mOsm) maintained at room temperature. Jaws infected cells were identified under 460-480 nm blue light, whereas visual guidance of the patch electrode was assisted by infrared DIC microscopy (Olympus BX51).

Electrodes for cortical recordings were pulled from thin-walled borosilicate glass capillary tubing using a P-97 puller (Sutter Instruments) and had resistances of 4-6 MΩ when filled with internal solution (composition in mM: potassium gluconate 125, NaCl 10, HEPES 20, Mg-ATP 3, Na-GTP 0.4, and 0.5% biocytin, in ddH20; osmolarity 289 mOsm; pH 7.31). Capacitance, series resistance, and input resistance were frequently measured throughout recording to monitor cell health. Cells were visualized through a 40X water-immersion objective on an upright microscope (Scientifica) equipped with infra-red (IR) differential interference contrast (DIC) optics and a Q-imaging Retiga Exi camera (Q Imaging).

Tip electrode resistance for dentate granule cell recordings was 4.6-7.4 MΩ in aCSF. Patch electrode solution consisted of (in mM) K-gluconate 122.5, KCl 12.5, KOH-HEPES 10, KOH-EGTA 0.2, MgATP 2, Na_3GTP 0.3, NaCl 8 (pH 7.35, mOsm 296) and 0.2-0.4 mg/ml biocytin was added immediately before use. 10 pA step hyper-/depolarization square current pulses were used to determine the input-output relationship and 300 pA ramp depolarization was used for AP generation. Non-infected dentate granule cells recorded from the contra-lateral dentate gyrus of viral injected mice or non-injected animals served as controls. None of these cells responded to 625 nm red light. Uncompensated series resistance was typically 14-25 MΩ and cells with resting membrane potential more positive than -50mV were discarded (n=3).

Optical activation was delivered to motor cortex using 500 ms pulses from 590 nm or 625 nm LEDs (Thorlabs), which were additionally filtered with bandpass filters (Semrock): 590 nm LED with 590 nm ± 10 nm filter or 625 nm LED with 632 nm ± 11 nm, and to dentate granule cells using 1 sec 625 nm red light (M625L3-C1, ThorLabs, 68 mW/mm^2). All light powers were

measured out of the objective lens with a PM200B photometer (Thorlabs). Illumination spot sizes were measured by photobleaching a focused microscope slide coated with Alexa 488 dye for 10 minutes under full intensity illumination, then imaging with a micrometer calibration slide to determine the photobleached radius.

All recordings were made using a Multiclamp 700B amplifier and Clampex 10 or 10.4 software (Molecular Devices, CA, USA). Cortical recordings were low-pass filtered at 1 Hz and digitized at 10 kHz using a Digidata 1550 (Molecular Devices, CA, USA); dentate granule cell recordings were digitized with a Digidata 1440. All data was analyzed using Clampfit (Molecular Devices) and MATLAB (Mathworks)

Retinal multi-electrode array recordings

Rodent information is outlined in Table 2.2. Experiments were conducted as previously described[30]. Briefly, for viral injections to the retina, animals were anaesthetized using 3% isoflurane. A small incision was made with a sharp 30-gauge needle in the sclera near the lens and 2 µl AAV particles were injected slowly into the subretinal space using a blunt 5 µl Hamilton syringe held in a micromanipulator.

To record spike trains of retinal ganglion cells, isolated mouse retinas were placed on a flat MEA60 200 Pt GND array (30 µm diameter microelectrodes spaced 200 µm apart) (Ayanda Biosystems or Multi Channel Systems). The retina was continuously superfused in oxygenated Ringer's solution (110mM NaCl, 2.5mM KCl, 1.0mM CaCl2, 1.6mM MgCl2, 22mM NaHCO3, and 10mM D-glucose (pH 7.4 with 95% O2/5% CO2)) at 36 C during experiments. Signals were recorded (MEA1060-2-BC, Multi-Channel Systems) and filtered between 500 Hz (low cut-off) and 3,500 Hz (high cut-off). Action potentials were extracted with a threshold of greater than 4 times the standard deviation of the recorded trace (Matlab, Mathworks).

Table 2.2 - Rodent information for retinal MEA recordings.

Strain	Age (d)	Gender	AAV incubation (d)	Opsin	Multi-electrode array recordings of the retinal ganglion cells
f-RD (C3H)	71	F	36	eNpHR	recordings
f-RD (C3H)	74	F	36	Halo57	recordings
f-RD	75	F	37	Halo57 (K200R	recordings

(C3H)				W214F)	
f-RD	64	F	34	ArchT	recordings
(C3H)					
f-RD	67	F	33	Mac	recordings
(C3H)					
f-RD	67	F	33	Mac	recordings
(C3H)					
f-RD	65	F	29	Jaws	recordings
(C3H)					
f-RD	50	F	22	eNpHR3.0	no response (patch clamp recordings of cones revealed tiny photocurrents; data not shown; n = 4 retinas)
(C3H)					
s-RD	113	F	21	eNpHR3.0	no response (patch-clamping was not tried; n = 3 retinas)

Histology

We performed histology on n = 6 mice injected with AAV8-synapsin-Jaws and n = 2 mice injected with AAV8-synapsin-eNpHR3.0 and n = 2 mice injected with AAV8-synapsin-Jaws-ER2, representative images from each of which are shown in Fig. 4 and 5. We examined n = 7 opsin-expressing retinas, and the images shown in Fig. 2 and Supplementary Fig. 5 are representative of the whole population.

Mice were terminally anesthetized with isoflurane, then perfused through the left cardiac ventricle with 4% paraformaldehyde in PBS. The brain was removed and sectioned into 40 μm coronal sections on a cryostat, and subsequently mounted with Vectashield HardSet (Vector Labs). Acute brain slices were fixed in 4% paraformaldehyde overnight at 4 °C after recording and then washed in PBS. The slices were blocked for 1 h at room temperature in PBS containing 3% normal donkey serum (NDS) and 0.3% Triton, followed by incubation with Alexa 405-conjugated streptavidin (1:1000; Life Technologies) in PBS containing 3% NDS and 0.3% Triton, for 2 h at room temperature, to reveal biocytin labelling. Brain slices were subsequently washed in PBS, mounted on glass slides, and coverslipped with PVA-DABCO (Sigma).

Cryosectioned slides were visualized and imaged with a Zeiss LSM 510 confocal microscope using 20x and 63x objective lenses, or a Nikon TI-E microscope using a 20x objective lens. Acute slices were imaged using a Olympus FV1000 confocal laser scanning microscope through a 10X / 0.40 numerical aperture objective or a 40X / 1.30 numerical aperture oil-immersion objective using Fluoview software (Olympus). Images were subsequently processed in Adobe Photoshop CS6 (Adobe Systems).

Retinal immunostaining was conducted as previously described[30]. Briefly, retinas were isolated and fixed in 4% paraformaldehyde in PBS for 30 min at room temperature (RT), and washed in PBS overnight at 4°C. Retinal whole mounts were incubated in 30% sucrose treated with three freeze-thaw cycles, after which all steps were performed at RT. Retinas were incubated in a blocking solution (10% normal donkey serum (NDS, Chemicon), 1% bovine serum albumin (BSA), and 0.5% Triton X-100 in PBS, pH 7.4) for 1h. Primary and secondary antibody applications were done in 3% NDS, 1% BSA, 0.02% sodium azide, and 0.5% Triton X-100 in PBS.

Primary antibodies for GFP (rat-GFP, 1/500, Nacalai/Brunschwig 04404-84) and mCAR (rabbit-cone-arrestin, 1/200, Millipore AB15282) were applied for 3 days. After washing the retina 3x for 10 min in PBS, the retina was incubated with Alexa Fluor-conjugated secondary antibodies (1:200 dilution) and 10 μg/ml DAPI (Roche Diagnostics) for 2h. After another three 10 min washes in PBS, the retina was mounted on a glass slide with ProLong Gold antifade reagent (Invitrogen). Confocal images of antibody-stained retinas were taken using a Axio Imager Z2 equipped with a LSM 700 scanning head.

Statistical analysis

No statistical methods were used to pre-determine sample sizes, but sample sizes in this paper were similar to previous papers from our group[1, 3, 60, 61], and were chosen to reflect sample sizes that might be experienced by end-users. No blinding was carried out, with the exception of cotransfected opsin-GFP and tdtomato datasets, as the chief goal of the paper was to demonstrate the capabilities of a new technology. No randomization was carried out. All replicates were biological.

Statistical analyses were performed using JMP Pro 10 (SAS Software) and Prism 5 (GraphPad). All data was tested for normality with a Shapiro-Wilk test. Two-sample comparisons were characterized with a two-tailed T-test, and multiway comparisons for a single variable were characterized with an ANOVA followed by a Newman-Keuls multiple comparison post-test between pairs. Paired tests were conducted with a two-tailed paired sample T-test. A Kolmogorov-Smirnov test was used to assess differences in spiking frequency distributions, due to its sensitivity to both location and shape of cumulative distribution functions.

References

1. Chow, B.Y. et al. High-performance genetically targetable optical neural silencing by light-driven proton pumps. *Nature* **463**, 98-102 (2010).
2. Gradinaru, V. et al. Molecular and cellular approaches for diversifying and extending optogenetics. *Cell* **141**, 154-165 (2010).
3. Han, X. et al. A high-light sensitivity optical neural silencer: development and application to optogenetic control of non-human primate cortex. *Frontiers in systems neuroscience* **5**, 18 (2011).
4. Martin, J.H. Autoradiographic estimation of the extent of reversible inactivation produced by microinjection of lidocaine and muscimol in the rat. *Neuroscience letters* **127**, 160-164 (1991).
5. Ibanez-Tallon, I. et al. Tethering naturally occurring peptide toxins for cell-autonomous modulation of ion channels and receptors in vivo. *Neuron* **43**, 305-311 (2004).
6. Armbruster, B.N., Li, X., Pausch, M.H., Herlitze, S. & Roth, B.L. Evolving the lock to fit the key to create a family of G protein-coupled receptors potently activated by an inert ligand. *Proceedings of the National Academy of Sciences of the United States of America* **104**, 5163-5168 (2007).
7. Kramer, R.H., Mourot, A. & Adesnik, H. Optogenetic pharmacology for control of native neuronal signaling proteins. *Nature neuroscience* **16**, 816-823 (2013).
8. Polikov, V.S., Tresco, P.A. & Reichert, W.M. Response of brain tissue to chronically implanted neural electrodes. *Journal of neuroscience methods* **148**, 1-18 (2005).
9. Nimmerjahn, A., Kirchhoff, F. & Helmchen, F. Resting microglial cells are highly dynamic surveillants of brain parenchyma in vivo. *Science* **308**, 1314-1318 (2005).
10. Xu, H.T., Pan, F., Yang, G. & Gan, W.B. Choice of cranial window type for in vivo imaging affects dendritic spine turnover in the cortex. *Nature neuroscience* **10**, 549-551 (2007).
11. Arenkiel, B.R. et al. In vivo light-induced activation of neural circuitry in transgenic mice expressing channelrhodopsin-2. *Neuron* **54**, 205-218 (2007).
12. Yizhar, O. et al. Neocortical excitation/inhibition balance in information processing and social dysfunction. *Nature* **477**, 171-178 (2011).
13. Drew, P.J. et al. Chronic optical access through a polished and reinforced thinned skull. *Nature methods* **7**, 981-984 (2010).
14. Huber, D. et al. Sparse optical microstimulation in barrel cortex drives learned behaviour in freely moving mice. *Nature* **451**, 61-64 (2008).
15. Gradinaru, V. et al. Targeting and readout strategies for fast optical neural control in vitro and in vivo. *The Journal of neuroscience : the official journal of the Society for Neuroscience* **27**, 14231-14238 (2007).
16. Iwai, Y., Honda, S., Ozeki, H., Hashimoto, M. & Hirase, H. A simple head-mountable LED device for chronic stimulation of optogenetic molecules in freely moving mice. *Neuroscience research* **70**, 124-127 (2011).
17. Scott, N.A. & Murphy, T.H. Hemodynamic responses evoked by neuronal stimulation via channelrhodopsin-2 can be independent of intracortical glutamatergic synaptic transmission. *PloS one* **7**, e29859 (2012).
18. Hira, R. et al. Transcranial optogenetic stimulation for functional mapping of the motor cortex. *Journal of neuroscience methods* **179**, 258-263 (2009).

19. Kleinlogel, S. et al. A gene-fusion strategy for stoichiometric and co-localized expression of light-gated membrane proteins. *Nature methods* **8**, 1083-1088 (2011).
20. Yizhar, O., Fenno, L.E., Davidson, T.J., Mogri, M. & Deisseroth, K. Optogenetics in neural systems. *Neuron* **71**, 9-34 (2011).
21. Wray, S., Cope, M., Delpy, D.T., Wyatt, J.S. & Reynolds, E.O. Characterization of the near infrared absorption spectra of cytochrome aa3 and haemoglobin for the non-invasive monitoring of cerebral oxygenation. *Biochimica et biophysica acta* **933**, 184-192 (1988).
22. Zijlstra, W.G., Buursma, A. & Meeuwsen-van der Roest, W.P. Absorption spectra of human fetal and adult oxyhemoglobin, de-oxyhemoglobin, carboxyhemoglobin, and methemoglobin. *Clinical chemistry* **37**, 1633-1638 (1991).
23. Biran, R., Martin, D.C. & Tresco, P.A. Neuronal cell loss accompanies the brain tissue response to chronically implanted silicon microelectrode arrays. *Experimental neurology* **195**, 115-126 (2005).
24. Kim, T.I. et al. Injectable, cellular-scale optoelectronics with applications for wireless optogenetics. *Science* **340**, 211-216 (2013).
25. Lin, J.Y., Knutsen, P.M., Muller, A., Kleinfeld, D. & Tsien, R.Y. ReaChR: a red-shifted variant of channelrhodopsin enables deep transcranial optogenetic excitation. *Nature neuroscience* **16**, 1499-1508 (2013).
26. Sato, M., Kanamori, T., Kamo, N., Demura, M. & Nitta, K. Stopped-flow analysis on anion binding to blue-form halorhodopsin from Natronobacterium pharaonis: comparison with the anion-uptake process during the photocycle. *Biochemistry* **41**, 2452-2458 (2002).
27. Ma, D. et al. Role of ER export signals in controlling surface potassium channel numbers. *Science* **291**, 316-319 (2001).
28. Hofherr, A., Fakler, B. & Klocker, N. Selective Golgi export of Kir2.1 controls the stoichiometry of functional Kir2.x channel heteromers. *Journal of cell science* **118**, 1935-1943 (2005).
29. Sung, C.H. & Chuang, J.Z. The cell biology of vision. *The Journal of cell biology* **190**, 953-963 (2010).
30. Busskamp, V. et al. Genetic reactivation of cone photoreceptors restores visual responses in retinitis pigmentosa. *Science* **329**, 413-417 (2010).
31. Menzler, J. & Zeck, G. Network oscillations in rod-degenerated mouse retinas. *The Journal of neuroscience : the official journal of the Society for Neuroscience* **31**, 2280-2291 (2011).
32. Farber, D.B., Flannery, J.G. & Bowes-Rickman, C. The rd mouse story: Seventy years of research on an animal model of inherited retinal degeneration. *Progress in Retinal and Eye Research* **13**, 31-64 (1994).
33. Busskamp, V. & Roska, B. Optogenetic approaches to restoring visual function in retinitis pigmentosa. *Current opinion in neurobiology* **21**, 942-946 (2011).
34. Gradinaru, V., Thompson, K.R. & Deisseroth, K. eNpHR: a Natronomonas halorhodopsin enhanced for optogenetic applications. *Brain cell biology* **36**, 129-139 (2008).
35. Cardin, J.A. Dissecting local circuits in vivo: Integrated optogenetic and electrophysiology approaches for exploring inhibitory regulation of cortical activity. *Journal of physiology, Paris* **106**, 104-111 (2012).
36. Madisen, L. et al. A toolbox of Cre-dependent optogenetic transgenic mice for light-induced activation and silencing. *Nature neuroscience* **15**, 793-802 (2012).

37. Arrenberg, A.B., Del Bene, F. & Baier, H. Optical control of zebrafish behavior with halorhodopsin. *Proceedings of the National Academy of Sciences of the United States of America* **106**, 17968-17973 (2009).
38. Tsunematsu, T. et al. Acute optogenetic silencing of orexin/hypocretin neurons induces slow-wave sleep in mice. *The Journal of neuroscience : the official journal of the Society for Neuroscience* **31**, 10529-10539 (2011).
39. Tonnesen, J., Sorensen, A.T., Deisseroth, K., Lundberg, C. & Kokaia, M. Optogenetic control of epileptiform activity. *Proceedings of the National Academy of Sciences of the United States of America* **106**, 12162-12167 (2009).
40. Mattis, J. et al. Principles for applying optogenetic tools derived from direct comparative analysis of microbial opsins. *Nature methods* **9**, 159-172 (2012).
41. Znamenskiy, P. & Zador, A.M. Corticostriatal neurons in auditory cortex drive decisions during auditory discrimination. *Nature* **497**, 482-485 (2013).
42. Gilmartin, M.R., Miyawaki, H., Helmstetter, F.J. & Diba, K. Prefrontal activity links nonoverlapping events in memory. *The Journal of neuroscience : the official journal of the Society for Neuroscience* **33**, 10910-10914 (2013).
43. Raimondo, J.V., Kay, L., Ellender, T.J. & Akerman, C.J. Optogenetic silencing strategies differ in their effects on inhibitory synaptic transmission. *Nature neuroscience* **15**, 1102-1104 (2012).
44. Znamenskiy, P. & Zador, A.M. Corticostriatal neurons in auditory cortex drive decisions during auditory discrimination. *Nature* (2013).
45. Tye, K.M. et al. Amygdala circuitry mediating reversible and bidirectional control of anxiety. *Nature* **471**, 358-362 (2011).
46. Jacobs, G.H., Williams, G.A., Cahill, H. & Nathans, J. Emergence of novel color vision in mice engineered to express a human cone photopigment. *Science* **315**, 1723-1725 (2007).
47. Naarendorp, F. et al. Dark light, rod saturation, and the absolute and incremental sensitivity of mouse cone vision. *The Journal of neuroscience : the official journal of the Society for Neuroscience* **30**, 12495-12507 (2010).
48. Anikeeva, P. et al. Optetrode: a multichannel readout for optogenetic control in freely moving mice. *Nature neuroscience* **15**, 163-170 (2012).
49. Lee, S.-H. et al. Activation of specific interneurons improves V1 feature selectivity and visual perception. *Nature* **advance online publication** (2012).
50. Grutzendler, J., Kasthuri, N. & Gan, W.B. Long-term dendritic spine stability in the adult cortex. *Nature* **420**, 812-816 (2002).
51. Yoder, E.J. & Kleinfeld, D. Cortical imaging through the intact mouse skull using two-photon excitation laser scanning microscopy. *Microscopy research and technique* **56**, 304-305 (2002).
52. Berenyi, A., Belluscio, M., Mao, D. & Buzsaki, G. Closed-loop control of epilepsy by transcranial electrical stimulation. *Science* **337**, 735-737 (2012).
53. Trachtenberg, J.T. et al. Long-term in vivo imaging of experience-dependent synaptic plasticity in adult cortex. *Nature* **420**, 788-794 (2002).
54. Jazayeri, M., Lindbloom-Brown, Z. & Horwitz, G.D. Saccadic eye movements evoked by optogenetic activation of primate V1. *Nature neuroscience* (2012).

55. Ohayon, S., Grimaldi, P., Schweers, N. & Tsao, D.Y. Saccade modulation by optical and electrical stimulation in the macaque frontal eye field. *The Journal of neuroscience : the official journal of the Society for Neuroscience* **33**, 16684-16697 (2013).
56. Ye, H., Daoud-El Baba, M., Peng, R.W. & Fussenegger, M. A synthetic optogenetic transcription device enhances blood-glucose homeostasis in mice. *Science* **332**, 1565-1568 (2011).
57. Klapoetke, N.C. et al. Independent optical excitation of distinct neural populations. *Nature methods* **11**, 338-346 (2014).
58. Grieger, J.C., Choi, V.W. & Samulski, R.J. Production and characterization of adeno-associated viral vectors. *Nature protocols* **1**, 1412-1428 (2006).
59. Cardin, J.A. et al. Driving fast-spiking cells induces gamma rhythm and controls sensory responses. *Nature* **459**, 663-667 (2009).
60. Boyden, E.S., Zhang, F., Bamberg, E., Nagel, G. & Deisseroth, K. Millisecond-timescale, genetically targeted optical control of neural activity. *Nature neuroscience* **8**, 1263-1268 (2005).
61. Han, X. & Boyden, E.S. Multiple-color optical activation, silencing, and desynchronization of neural activity, with single-spike temporal resolution. *PloS one* **2**, e299 (2007).

Chapter 3 - Transgenic mice for intersectional targeting of neural sensors and effectors with high specificity and performance

The data shown in this chapter was adapted from a manuscript published in Neuron, in collaboration with Linda Madisen and Hongkui Zeng of the Allen Brain Institute. Linda generated the Ai57 and Ai79 transgenic lines with the help of many others at the Allen Brain Institute, which Nathan Klapoetke and I characterized via *in vivo* extracellular recordings and slice electrophysiology. Nathan and I generated and analyzed all electrophysiology data presented in this chapter; I wrote or contributed to all text in this chapter.

Introduction

While viral gene delivery and *in utero* electroporation have been widely utilized for the heterologous expression of optogenetic proteins, the generation of transgenic animals is of increasing interest due to their ability to target and cover large tissue volumes independent of injection diffusion or packaging limits, their widespread genetic specificity independent of laminar specificity or developmental stage, their consistent protein expression levels, and their lack of invasive surgeries. In previous years, multiple transgenic rodent lines expressing microbial rhodopsins have been generated (Table 3.1), but these have been frequently restricted by poor expression or limited genetic specificity.

Previously, we generated and characterized opsin-expressing mice in which transgene expression of ChR2 (H1343R), Arch, and eNpHR3.0 was driven by a strong, ubiquitous CAG promoter (pCAG) targeted to the Rosa26 locus[1, 2] and functionally validated these animals in double-transgenic crosses using Cre-driver lines[1, 3-5] (**Error! Reference source not found.**). While these strains were useful in some contexts, their broader functionality was limited by the overall low expression. Further, Cre-reporter expression is only as specific as the endogenous regulatory sequences driving Cre-expression. We therefore felt more effective transgenic strategies were necessary.

Table 3.1 - Rodent transgenic lines expressing microbial rhodopsins.

Line name	Opsin	Strategy	Reference
Thy1.2-ChR2-eYFP	ChR2	Plasmid transgenic	Arenkiel Neuron 2007[6]
Thy1.2-NpHR-eYFP	NpHR	Plasmid transgenic	Zhao Brain Cell Biol. 2008[7]
Omp-ChR2-eYFP	ChR2	Plasmid transgenic	Dhawale Nat. Neuro 2010[8]
Vglut-ChR2 (H134R)-eYFP	ChR2 (H134R)	BAC transgenic	Hagglund Nat. Neuro 2010[9]
VGAT-ChR2 (H134R)-eYFP	ChR2 (H134R)	BAC transgenic	Zhao Nat. Methods 2011[10]
TPH2-ChR2 (H134R)-eYFP	ChR2 (H134R)	BAC transgenic	Zhao Nat. Methods 2011[10]
ChAT-ChR2 (H134R)-eYFP	ChR2 (H134R)	BAC transgenic	Zhao Nat. Methods 2011[10]
Pvalb-ChR2 (H134R)-eYFP	ChR2 (H134R)	BAC transgenic	Zhao Nat. Methods 2011[10]
Omp-ChR2-eYFP	ChR2 (H134R)	Knock-in	Smear Nature 2011[11]
R26-ChR2 (H134R)-eGFP	ChR2 (H134R)	Cre-inducible knock-in	Katzel Nat. Neuro 2011[12]
orexin-NpHR-eGFP	NpHR	Knock-in	Tsunematsu J. Neuroscience 2011[13]
Ai27 (ChR2 (H134R)-tdtomato)	ChR2 (H134R)	Cre-inducible knock-in	Madisen Nat. Neuro 2012[14]
Ai32 (ChR2 (H134R)-eYFP)	ChR2 (H134R)	Cre-inducible knock-in	Madisen Nat. Neuro 2012[14]
Ai35 (ss-Arch-eGFP-ER2)	ss-Arch-ER2	Cre-inducible knock-in	Madisen Nat. Neuro 2012[14]
Ai39 (eNpHR3.0)	eNpHR3.0	Cre-inducible knock-in	Madisen Nat. Neuro 2012[14]
Thy1-NphR-eYFP	NpHR	Plasmid transgenic	Asrican Front. Neural Circ. 2013[15]
Thy1-eNpHR2.0-eYFP	eNpHR2.0	Plasmid transgenic	Asrican Front. Neural Circ. 2013[15]
Thy1-VChR1-eYFP	VChR1	Plasmid transgenic	Asrican Front. Neural Circ. 2013[15]
Thy1-ChR2-eYFP	ChR2	Plasmid transgenic	Asrican Front. Neural Circ. 2013[15]
PV-ChR2-mCherry	ChR2	BAC transgenic	Asrican Front. Neural Circ. 2013[15]
PV-ChR2-eYFP	ChR2	BAC transgenic	Asrican Front. Neural Circ. 2013[15]
Thy1-ChR2-tdtomato	ChR2	BAC transgenic	Asrican Front. Neural Circ. 2013[15]
PV-ChR2 (H134R)-eYFP	ChR2 (H134R)	BAC transgenic	Asrican Front. Neural Circ. 2013[15]
TetO-ChETA-eGFP	ChR2 (E123T T159C)	Knock-in	Tsunematsu J. Neuroscience 2014[16]
TetO-ArchT-eGFP	ArchT	Knock-in	Tsunematsu J. Neuroscience 2014[16]

The majority of Cre-dependent reporter transgenic lines either flip the cassette of interest, or preface it with lox stop sites. To achieve additional levels of specificity, we previously validated a novel genomic locus known as the TIGRE locus, introducing a tTa-based transcriptional approach[17] (Figure 3.1). Given its previous success, we chose to implement optogenetic effectors in the TIGRE locus and found that reporter lines doubly regulated by Cre and tTA drove robust expression of optogenetic effectors at levels substantially higher than those in comparable Rosa26-CAG based reporters. Functional characterization of lines carrying representative types of optical tools under Cre and tTA control demonstrates their utility for high-performance studies of neuronal activity, both *in vitro* and *in vivo* and the utility of TIGRE as a useful foundation for transgene expression strategies that require high-level and reliable tTA-inducible gene regulation.

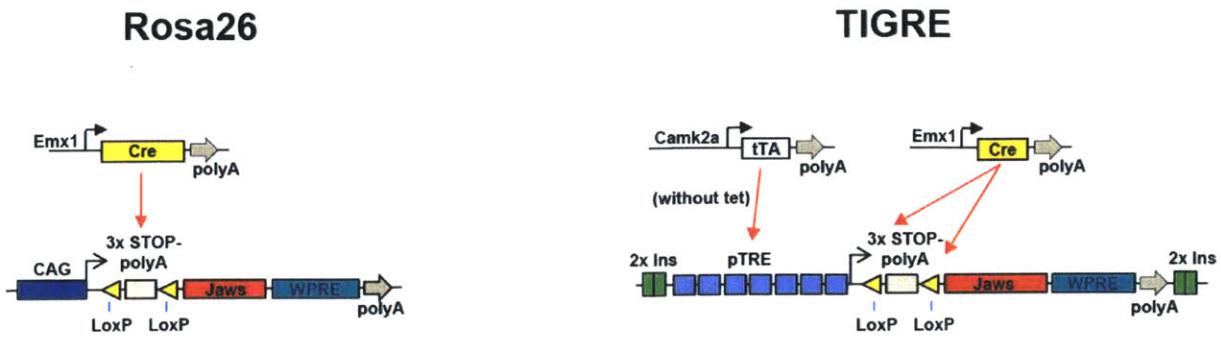

Figure 3.1 - Schematic of Rosa26 vs TIGRE transgenic targeting approaches

The binary transgenic systems for expressing optogenetic tools (using ChR2 as an example). Previous knock-in transgenics were generated in the Rosa26 locus using the Cre-lox system (*left*), in which Cre-mediated recombination excises the stop codon cassette between the two loxP sites and induces transgene expression. The TIGRE approach (*right*) has an extra tet-inducible component (tTa) which is expressed under a specific promoter in the driver line of interest. The transgene is expressed under the TRE promoter, which tTa binds in the absence of tetracycline or doxycycline, and expression is induced. When tetracycline is present, tTa does not bind the TRE promoter and transgene transcription stops..

Cre/tTA dependent reporters targeted to the TIGRE locus are more highly expressed than in Rosa26-CAG reporter lines

We tested two transactivators, Gal4 and tTa to combine the requirement for Cre activity with that for a transcriptional transactivator. The tetracycline (Tet)-regulated expression system allows for inducible expression of genes from the TRE (tetracycline response element, also often called tetO) promoter in response to tTA (Tet-Off) or rtTA (Tet-On) activation[18-21], and we previously established that TRE driven genes retrovirally targeted to the mouse TIGRE locus could be expressed in most tissues in the presence of tTA[17]. To determine whether tTA/TRE can drive the selective expression of functionally high levels of fluorescent markers, sensors, and effectors, we created an expression platform in the TIGRE locus by homologous recombination. To establish feasibility, we first generated a tdTomato reporter allele, whose expression depends both on activation of the TRE promoter and on Cre recombinase activity (Figure 3.2a). Notably, our reporter allele also contains the WPRE element, to increase expression levels, and is flanked

by two copies of the chicken β-globin HS4 insulator element[22, 23] on each side, which prevent repressive chromatin modifications from spreading into and silencing the reporter allele. We refer to this new reporter line using the acronym Ai62(TITL-tdT), to represent the TIGRE-Insulator-TRE promoter-LSL-tdTomato components within it.

To determine how expression from our new Ai62(TITL-tdT) reporter compares with that from Ai14 (which targets the traditional Rosa26 locus), we generated a series of double and triple transgenic lines containing tdTomato, Cre and/or tTA expressing alleles and evaluated native fluorescence in the brain (Figure 3.2b). We incorporated three different tTA lines into our TIGRE mice: Camk2a-tTA, ROSA:LNL:tTA, and ROSA26-ZtTA to test whether their varying tTA expression levels would influence the amount of reporter produced. To evaluate all these lines on a common benchmark, we crossed the reporters to Nr5a1-Cre, which drives specific expression in cortical layer 4 neurons.

We observed robust tdTomato fluorescence in cortical layer 4 cells in Nr5a1-Cre;Ai14 mice and in each of the three Ai62(TITL-tdT) triple Tg lines containing Nr5a1-Cre (Figure 3.2b). The overall levels of tdTomato fluorescence varied considerably across the three Ai62(TITL-tdT) triple Tg lines, yet expression in each appeared higher than that in the Rosa26-based Ai14 reporter. Expression was lowest in Nr5a1-Cre;Ai14, followed by Nr5a1-Cre;ROSA:LNL:tTA;Ai62(TITL-tdT), by Nr5a1-Cre;ROSA26-ZtTA;Ai62(TITL-tdT), and finally by Nr5a1-Cre;Camk2a-tTA;Ai62(TITL-tdT), where expression was highest (Figure 3.2b). Interestingly, we found that inclusion of the two flanking sets of chromatin insulators is essential for high level reporter expression, as a TIGRE reporter allele that lacks these elements is poorly expressed in similar triple transgenic animals (Figure 3.2d). From the comparative studies above, we conclude that the TIGRE-targeted Ai62(TITL-tdT) reporter presents considerable advantages over Rosa26-targeted Ai14, namely, more robust transgene expression and the potential for additional specificity mediated through restricted tTA expression.

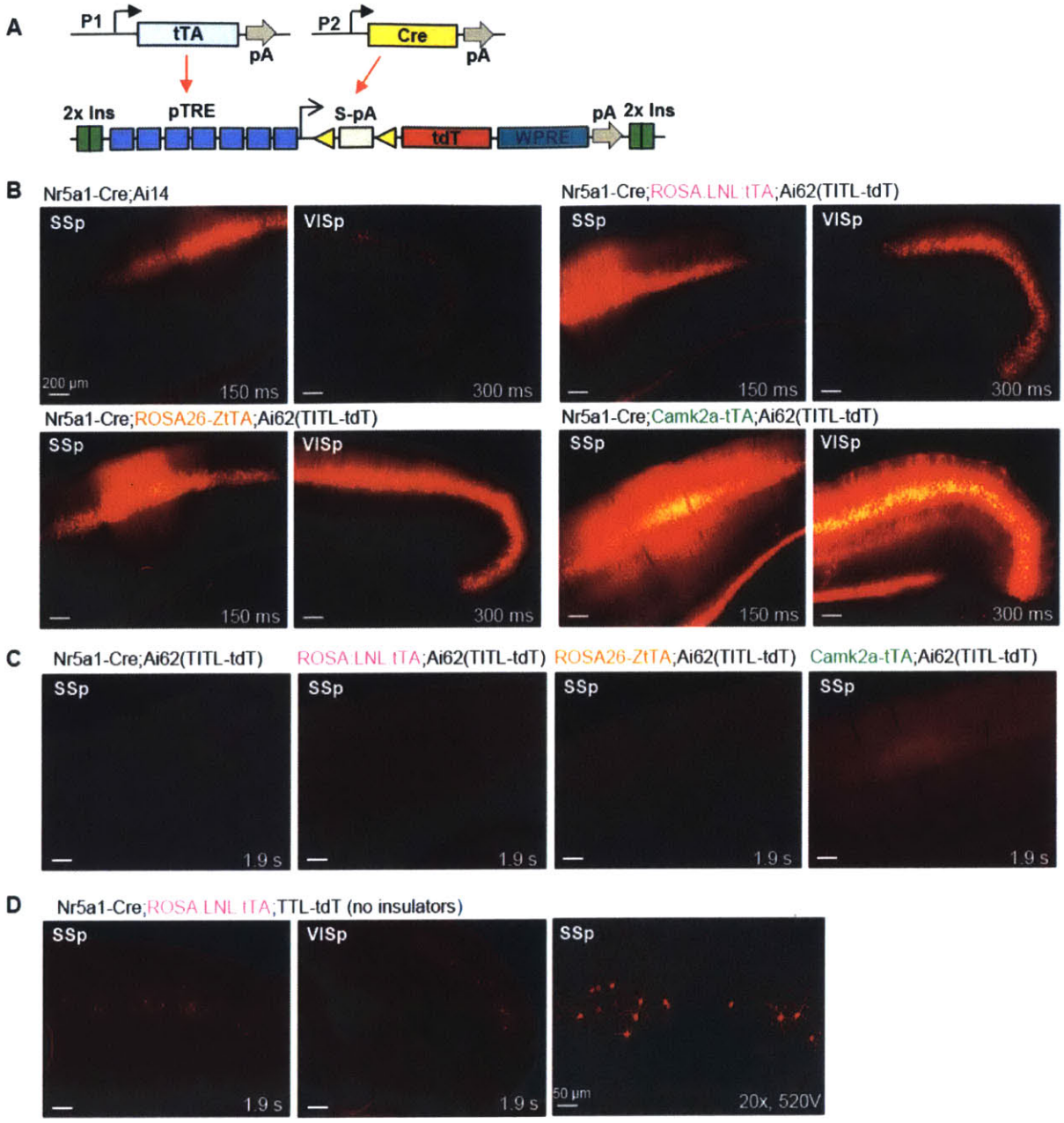

Figure 3.2 - Cre and tTa dependent intersectional expression at the TIGRE locus produces tightly regulated and high-level expression.

(a) Schematic of intersectional control by Cre and tTA, driven by different promoters (P1 or P2), on a double reporter line based in the TIGRE locus, Ai62(TITL-tdT). **(b)** Comparison of tdTomato fluorescence in 4 transgenic mouse lines carrying either Ai14 or Ai62 reporter alleles. **(c)** No detectable tdTomato expression in the Cre+/tTA- control Nr5a1-Cre;Ai62(TITL-tdT), or in Cre-/tTA+ controls ROSA:LNL:tTA;Ai62(TITL-tdT) and ROSA26-ZtTA;Ai62(TITL-tdT). Very weak tdTomato fluorescence was seen in the barrel cortex and

hippocampus of Camk2a-tTA;Ai62(TITL-tdT) control mice (Cre-/tTA+). **(d)** Poor tdTomato expression in similar triple Tg mice with a TIGRE reporter (TTL-tdT) that lacks chromatin insulators (compare to B). Right, a higher magnification confocal image of somatosensory cortex shows that the sparsely labeled cells are layer 4 neurons. For B-D, exposure time for each epifluorescence image is shown for comparison.

New TIGRE reporter lines with strong expression of sensors and effectors

Based on the enhanced Ai62 expression levels, we next proceeded to generate a series of TIGRE reporter lines carrying a variety of fluorescent sensors and optogenetic effectors: calcium indicators GCaMP6f and GCaMP6s[24], voltage indicator VSFP-Butterfly 1.2 (VSFPB)[25], glutamate sensor iGluSnFR[26], and red-light optogenetic inhibitor Jaws[27]. In parallel, we generated Rosa26-based reporter lines for further direct comparison between the Rosa26-CAG and TIGRE-TRE expression systems.

We used identical imaging parameters to evaluate native fluorescence via confocal microscopy for pairs of age-matched reporter mice crossed to the same Cre lines (Figure 3.3) and found transgenes were consistently more highly expressed from the TIGRE alleles than the Rosa26 allele. In all cases, we observed strong expression of reporter transgenes without overt cytotoxicity. To further compare gene expression patterns in Rosa26 and TIGRE reporter lines, we evaluated mRNA expression in multiple lines by in situ hybridization (ISH) (Figure 3.4). All lines examined exhibited widespread and high-density expression in cortex when under the control of Emx1-IRES-Cre alone (for Rosa26 lines), or in combination with Camk2a-tTA (for TIGRE lines).

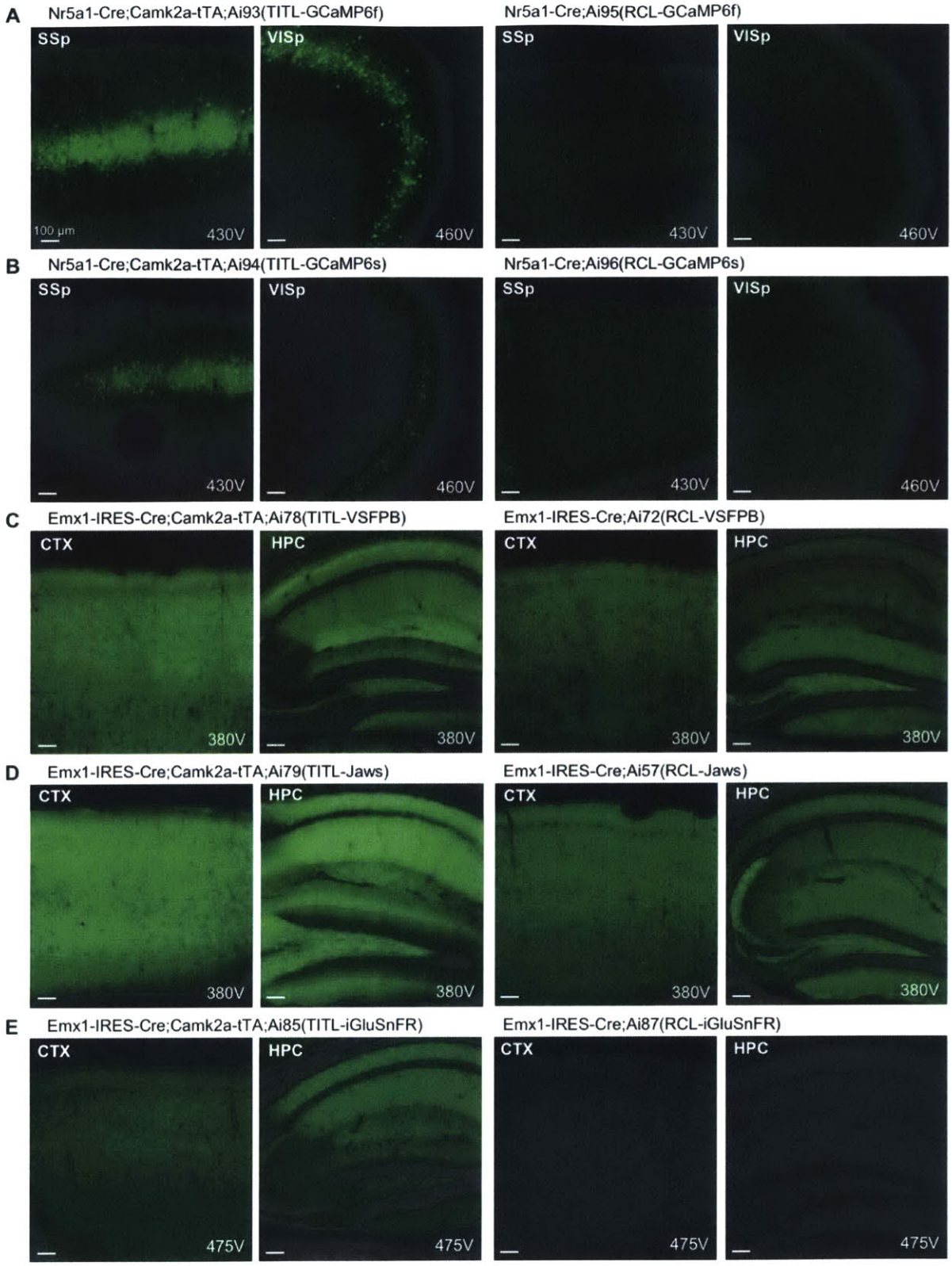
A
Nr5a1-Cre;Camk2a-tTA;Ai93(TITL-GCaMP6f)
Nr5a1-Cre;Ai95(RCL-GCaMP6f)
SSp
VISp
SSp
VISp
100 μm
430V
460V
430V
460V
B
Nr5a1-Cre;Camk2a-tTA;Ai94(TITL-GCaMP6s)
Nr5a1-Cre;Ai96(RCL-GCaMP6s)
SSp
VISp
SSp
VISp
430V
460V
430V
460V
C
Emx1-IRES-Cre;Camk2a-tTA;Ai78(TITL-VSFPB)
Emx1-IRES-Cre;Ai72(RCL-VSFPB)
CTX
HPC
CTX
HPC
380V
380V
380V
380V
D
Emx1-IRES-Cre;Camk2a-tTA;Ai79(TITL-Jaws)
Emx1-IRES-Cre;Ai57(RCL-Jaws)
CTX
HPC
CTX
HPC
380V
380V
380V
380V
E
Emx1-IRES-Cre;Camk2a-tTA;Ai85(TITL-iGluSnFR)
Emx1-IRES-Cre;Ai87(RCL-iGluSnFR)
CTX
HPC
CTX
HPC
475V
475V
475V
475V

Figure 3.3 - TIGRE reporter lines have higher levels of transgene expression than Rosa26 reporter lines.

Native fluorescence in each pair of lines was compared by confocal microscopy using identical imaging parameters. All images were taken under a 10x objective using 10% laser power, and the PMT gain (in voltage) is indicated on each image. Mouse names are shown above each set of images taken from the same mouse. Comparisons are shown for **(a)** GCaMP6f, **(b)** GCaMP6s, **(c)** VSFP-Butterfly 1.2, **(d)** Jaws-GFP-ER2, and **(e)** iGluSnFR. Ai57(RCL-Jaws) was created by crossing Ai57(RCFL-Jaws) with a Flp-deleter mouse, FLPeR, to delete the FSF cassette.

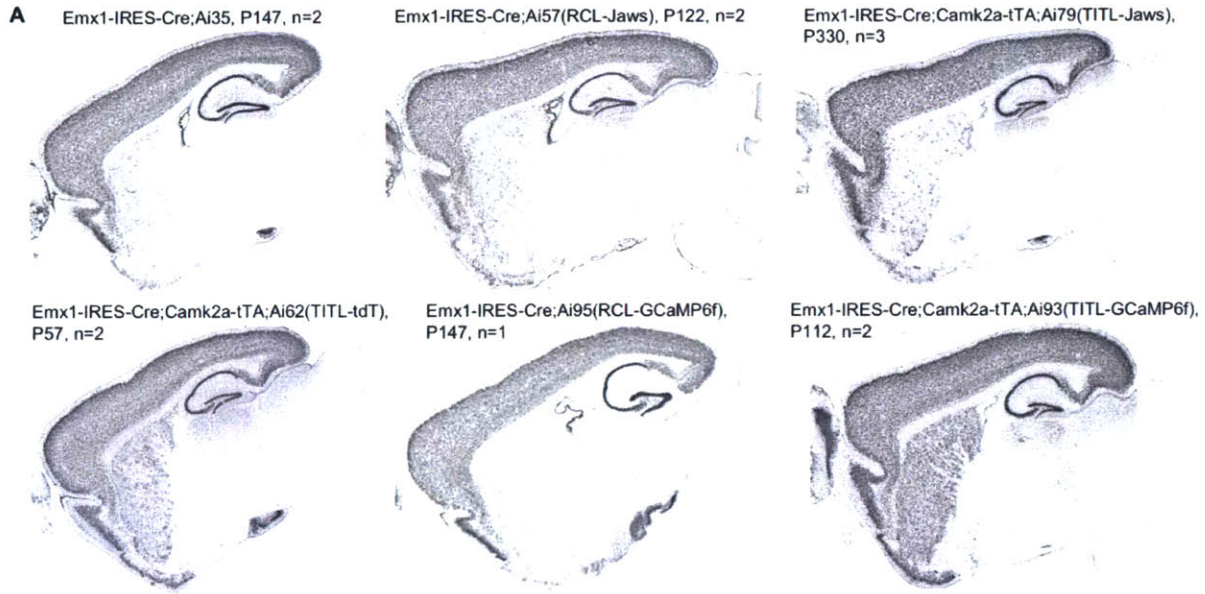

Figure 3.4 - In situ hybridization characterization of reporter gene expression patterns in multiple transgenic lines.

Number of mice used for ISH for each line and their representative age are shown. Note that expression levels can't be compared reliably between different mice due to the saturation of ISH signals in both expression systems shown. ISH comparison of various Rosa26 and TIGRE lines under the control of Emx1-IRES-Cre alone, or in combination with Camk2a-tTA or ROSA26-ZtTA. All mice exhibited widespread and high-density expression in cortex, and there was no significant difference in number of expressed cells between different lines or across ages. There is variability in number of expressed cells in striatum.

Red light-mediated optogenetic inhibition in TIGRE-Jaws mice

Jaws is the first red light drivable optogenetic inhibitor, engineered from the *H. salinarum* (strain shark) cruxhalorhodopsin[27]. Compared with other photoactivated inhibitors such as eNpHR3.0[28], Arch[29] or ArchT[30], Jaws responds robustly to red light with high sensitivity, large photocurrent and fast kinetics, and thus enables better tissue penetrance and more effective optogenetic silencing of large volumes[27]. We compared the performance of a modified trafficking variant of Jaws, Jaws-GFP-ER2, expressed from the Rosa-CAG allele, *i.e.* Emx1-IRES-Cre;Ai57(RCL-Jaws) mice (simplified as Ai57), and the TIGRE allele, *i.e.* Emx1-IRES-Cre;Camk2a-tTA;Ai79(TITL-Jaws) mice (simplified as Ai79), via slice and *in vivo* electrophysiology, using virally expressed Jaws (AAV8-hSyn-Jaws) and Arch-expressing mice Ai35 as references[14, 27].

In brain slices, Jaws-expressing cells showed normal membrane properties (n = 13 cells in Ai57 mice, n = 17 cells in Ai79 mice, n = 12 in Ai35 mice, Figure 3.5). Red light illumination (632 nm) induced strong hyperpolarizing currents in Jaws-expressing neurons in Ai79 mice and effectively blocked depolarization-induced spiking, whereas the light effect was small to moderate in Ai57 mice (Figure 3.6a-c). Photocurrents were comparable between Ai79 and virally expressed Jaws at all irradiance levels tested, but were significantly smaller in Ai35 and Ai57 cells (Figure 3.6d-e). The low photocurrents generated between the Ai35 and Ai57 mice were similar (Figure 3.6d-e).

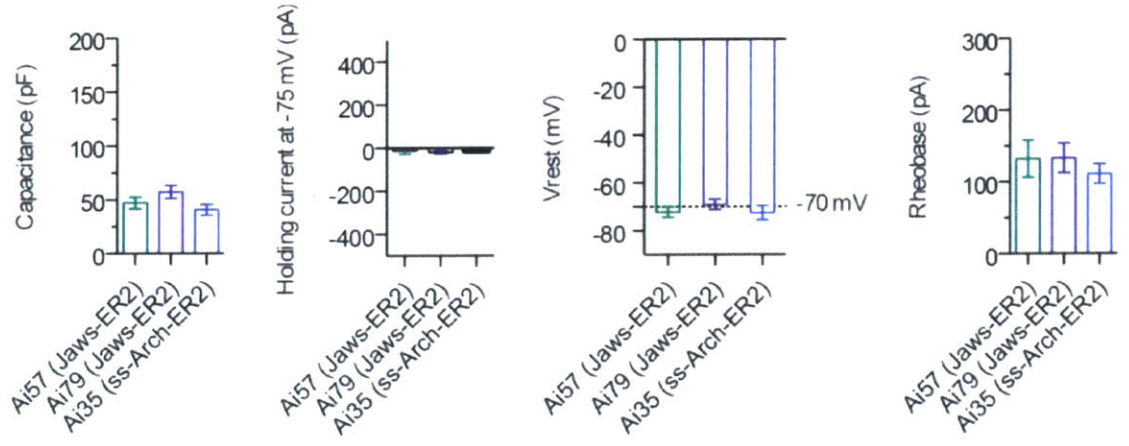

Figure 3.5 - Comparison of membrane properties for different inhibitory opsin transgenic lines.

Normal membrane electrophysiological properties in Jaws-expressing neurons in brain slices from Ai57, Ai79 and Ai35 mice. All values represent mean ± SEM.

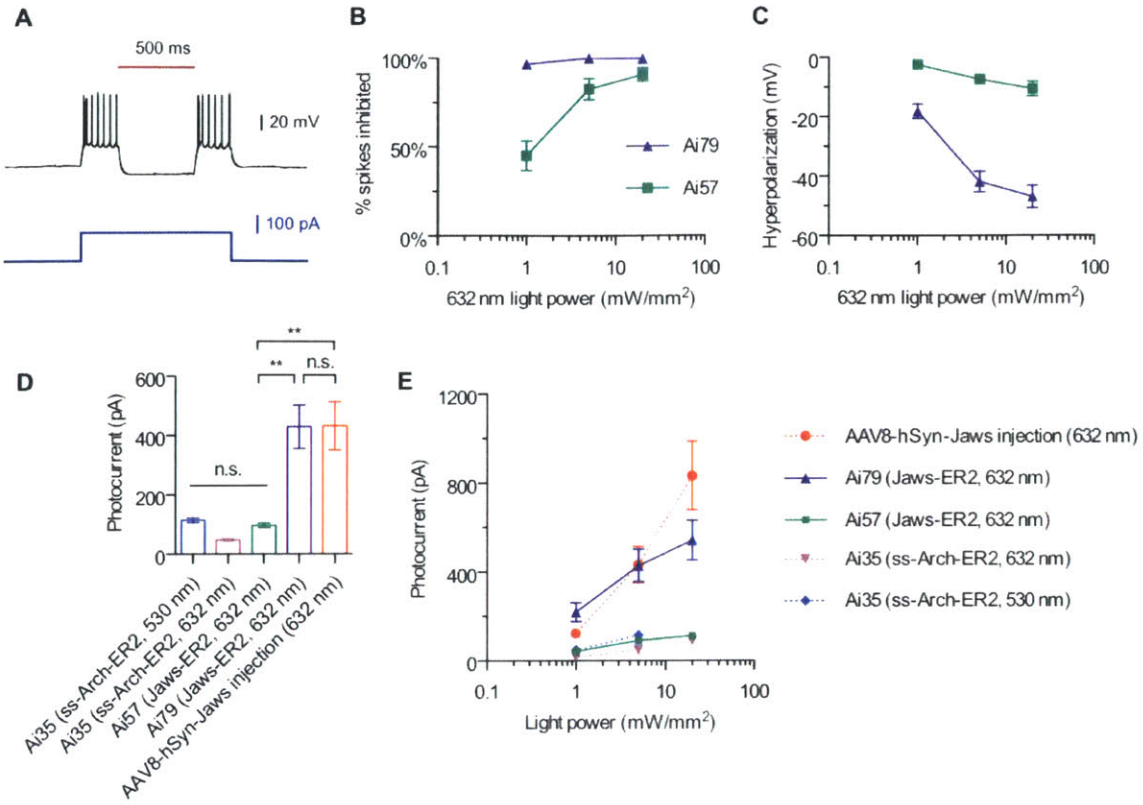

Figure 3.6 - Ex vivo comparison of different inhibitory opsin transgenic lines.

(a) Representative current-clamp recording of a Jaws-expressing neuron from Ai79 undergoing optically evoked (632 nm, 5 mW/mm^2) hyperpolarization in an acute cortical slice. **(b)** Comparison of red light induced inhibition of electrically evoked spiking in slices from Ai79 and Ai57 mice. Spiking was induced by a current injection of 1.5x the rheobase. **(c)** Comparison of red light induced hyperpolarization in slices from Ai79 and Ai57 mice. **(d)** Comparison of red or green light (632 or 530 nm, 5 mW/mm^2) induced photocurrents in slices from Ai79, Ai57, Ai35 and AAV-Jaws virus injected mice. **(e)** Comparison of light induced photocurrents in slices from Ai79, Ai57, Ai35 and AAV-Jaws virus injected mice across different light intensities for red or green light.

Next we assessed Jaws performance *in vivo*. We conducted extracellular recordings in the primary visual cortex of awake, head-fixed mice using glass pipettes and delivering illumination with a 200-µm optical fiber[27]. Due to the poor performance of Ai35 and Ai57 in slice, only Ai79

was tested *in vivo*. Ai79 showed strong red light (637 nm) induced suppression of spontaneous neuronal firing (Figure 3.7; n = 23 units from 2 mice, n = 3 units showed no change). Light delivery through the fiber tip inhibited neuronal firing in a light intensity-dependent manner in these mice, comparable to the performance of virally-expressed Jaws (Figure 3.7). Taken together our data verify the TIGRE approach of optogenetically silencing neural activity both *in vitro* and in *vivo* and provide functional evidence that the TIGRE-TRE system results in better functionality than the Rosa-CAG system.

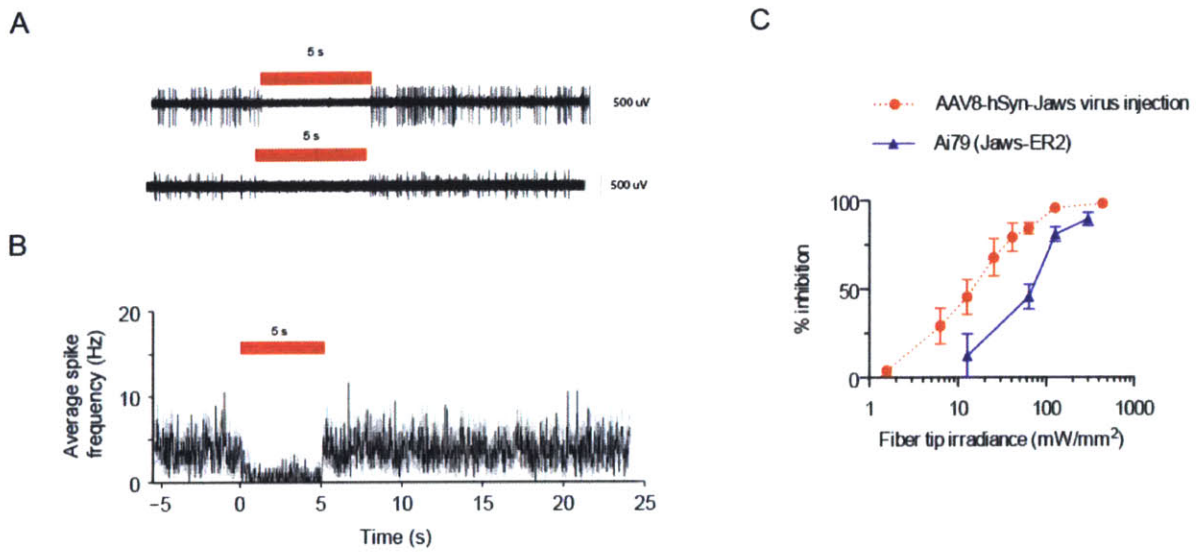

Figure 3.7 - *In vivo* comparison of virally-expressed versus Jaws-transgenic suppression of spontaneous activity in rodent cortex.

Representative extracellular recordings **(a)** in awake Ai79 mice demonstrate the in vivo inhibition of spontaneous firing activities **(b)** of Jaws-expressing neurons. **(c)** Comparison of in vivo inhibition of spontaneous firing activities over a range of red light intensities between Ai79 and AAV-Jaws injected mice. All values represent mean ± SEM. ** $p < 0.01$, n.s. not significant.

Discussion

We sought to develop transgenic strategies for intersectional control and to compare performance of these strategies under native conditions in the mouse brain. In addition to striving for high-level and highly specific expression of genetic tools, we aimed to generate standardized

expression platforms, in a few defined genomic loci, that would allow rapid modification for future improvements and applications. Such efforts are more laborious and time-consuming than other in vivo approaches, such as random transgenesis or viral infection, but they can provide more definitive evaluations and more consistent platforms for incorporating additional genetic tools and expansion into other cell types.

While the functional comparisons here do suggest that the Ai79 transgenic strain possess superior photocurrents and hyperpolarization as compared to the Ai57 strain, it is difficult to extrapolate further since the TIGRE transgenics differ from the Rosa26 in genomic location, promoter, and the addition of flanking chromatin insulators: we cannot disambiguate which of these (or what combination of these) led to the improvement in function. The mechanism of the TIGRE locus improvements is therefore still unknown. Histological analyses suggest that the total fluorescence level is higher, but we also cannot draw any conclusions about the amount of membrane-localized (and therefore functional) protein without more quantitative histology.

Although the data presented here suggests that the Ai79 mice are indeed capable of robust red-light driven *ex vivo* and *in vivo* inhibition, recordings from a more sparsely-labeled Cre-reporter line would have been more ideal than the double-crossed Emx1-Cre CamKII-tTa lines, which theoretically labels all excitatory cortical neurons. Since light from a 200 um fiber illuminates a volume of approximately a cubic millimeter, we cannot rule out that some of the observed inhibition may result from network activity.

Another, more general problem in transgenic animals is that of leaky transgene expression in the absence of Cre[31], which has been demonstrated previously on the mRNA level[14]. While we do demonstrate Jaws' function in Cre-crossed animals, it would have been better to record from non-crossed as well as doxycycline-fed animals to better understand basal leak expression levels which may impact neuroscientific experiments that wish to address a more sparse subset of neurons.

The Ai79 transgenic line reported here should facilitate novel neuroscientific experiments, and suggests that the TIGRE platform has potential for expressing new or existing genetically-encoded tools. However, the question of whether this locus should be more broadly adopted requires further characterization.

Experimental Procedures

All experimental procedures related to the use of mice were conducted according to NIH guidelines, the UK Animals Scientific Procedures Act (1986), and the New Zealand Animal Welfare Act (1999). Experiments performed at the Allen Institute were approved by the Institutional Animal Care and Use Committee (IACUC) of the Allen Institute for Brain Science.

Transgenic mice generation

Targeting constructs were generated using a combination of molecular cloning, gene synthesis (GenScript, Piscataway, US) and Red/ET recombineering (Gene Bridges, Heidelberg, DE). Coding sequences were cloned between the LSL cassette and the WPRE element in the targeting backbones described below, either directly from acquired plasmids or after gene synthesis based on published information. The 129S6B6F1 ES cell line, G4, was used to generate all transgenic mice by homologous recombination and, in many cases, subsequent Flp- recombinase-mediated cassette exchange (RMCE). Correct clones were used in blastocyst injections to obtain germline transmission. Resulting mice were crossed to the Rosa26-PhiC31 mice (JAX Stock # 007743) to delete the pPGK-neo or pPGK-hygro selection marker cassette, and then backcrossed to C57BL/6J mice and maintained in C57BL/6J congenic background.

Rosa26-pCAG-LSL-WPRE-bGHpA (RCL) vectors: Vector backbone has been previously described[1] and contains a loxP – stop codons – 3x SV40 polyA – loxP cassette.

TIGRE vectors: ES clones carrying TIGRE reporters were generated by a recombinase-mediated cassette exchange (RMCE) strategy into an ES clone that had been first targeted with a Flp/FRT-based docking site. In our first step to generate this ES clone with a docking site inserted into the TIGRE locus, the original targeting vector contained: 5' and 3'homology arms (base pairs 21539059-21545314 and 21545315-21549209, respectively, of ref_NC 000075.6 on mouse chromosome 9) flanking the following cassette: FRT3 (F3) – AttB – pPGK – neomycin-resistant gene – PGK polyA – FRT5 (F5) – mRNA splice acceptor – domain 2 from the hygromycin-resistant gene – SV40 polyA – AttP. Southern blot analysis was done on neo resistant ES clones to confirm correct construct integration. Several targeted clones were injected into blastocysts, and those that gave rise to high-percentage chimeras were chosen for expansion and use in the RMCE transfections.

Replacement vectors used for RMCE into the TIGRE docking site: The replacement vectors were in the following: F3 – 2 copies of the 1.2-kb chicken β-globin HS4 insulator fragment – pTRE-Tight – loxP – an 8 amino acid open reading frame – stop codons – a synthetic polyA – hGH polyA – PGK polyA – loxP – Transgene – WPRE – bGH polyA – 2 copies of the 1.2-kb chicken β-globin HS4 insulator fragment – AttB – pPGK – domain 1 from the hygromycin-resistant gene – mRNA splice donor – F5. The TRE promoter used here was from Clontech's pTRE-Tight vector, which contains a modified Tet response element (TREmod) that consists of seven direct repeats of a 36-bp sequence containing the 19-bp tet operator sequence (tetO); the TREmod is just upstream of the minimal CMV promoter. Supercoiled replacement vectors were co-transfected with a pCAG-Flpe plasmid into the above TIGRE docking clones and selected with hygromycin. Resistant colonies were screened for correct 5' and 3' junctions and for the lack of the original docking site sequence.

Transgenic mice expression characterization

Driver and reporter lines were crossed together according to specific schemes. Expression of the reporter genes was assessed by native fluorescence (without antibody staining) on perfused, microtomed sections or by *in situ* hybridization (ISH) on fresh-frozen sections.

For analysis of native fluorescence, animals were perfused with 4% paraformaldehyde (PFA) in 0.1 M PB. Brains were fixed for an additional 18 hr at 4°C, then cryoprotected in 10% sucrose in PBS at 4°C overnight. Brains were sectioned to 100 μm using a Leica SM2000R sliding microtome and sections were mounted onto slides. The sections were examined by epifluorescence microscopy without antibody staining. For confocal imaging, sections were imaged using an Olympus FV1000 confocal system with 10x or 20x objectives. To keep imaging conditions constant for comparison purposes, laser power was always set at 10%, whereas PMT gain was adjusted to stay within proper dynamic range but kept constant within each group of brains being compared and the value was reported for each confocal image shown in this paper.

For ISH, we used the Allen Institute–established pipelines for tissue processing, riboprobe hybridization, image acquisition and data processing[1, 32]. Riboprobes used for expression profiling ISH were designed against Cre, tdTomato and EYFP/EGFP. All transgenic mice characterization data can be found at the Transgenic Mouse database[33].

***In vitro* and *in vivo* electrophysiology of optogenetic silencing**

All light powers were measured with a PM200B photodetector (Thorlabs); all *in vivo* light powers were reported as measured at a 200 μm fiber tip with an integrating sphere (S142C, Thorlabs) rather than calculated at a distance[27].

In vivo extracellular recordings were conducted as before[27]. Briefly, adult mice were implanted with a metal headplate and a circular craniotomy was made over the primary visual cortex. Extracellular recordings were conducted in the cortex of awake, head-fixed mice using 3-10 MΩ saline-filled glass microelectrodes containing silver/silver-chloride electrodes. Signals were amplified with a Multiclamp 700B and digitized with a Digidata 1440B, using pClamp software (Molecular Devices). A recording glass electrode was attached to a 200 μm diameter optical fiber, coupled to a 473 nm or 637 nm laser (Coherent Lasers), such that the fiber tip was 500 ± 50 μm above the tip of the electrode, and guided into the brain with a Sutter manipulator. Light pulses were controlled via Digidata-generated TTL pulses, and data was analyzed using MATLAB and Offline Sorter (Plexon). Light-modulated units were identified by performing a paired t-test between the 5-s illumination period and the baseline firing period of the same time duration immediately before illumination, thresholding at $P < 0.05$. The degree of suppression was calculated for each cell by dividing the mean firing rate during the light stimulus by the mean baseline firing rate during the same time duration before light stimulation onset.

Ex vivo electrophysiology was carried out with 300 μm brain slices. Mice were deeply anaesthetized with isoflurane, then transcardially perfused with 40 ml of ice-cold ACSF (in mM: NaCl 87, KCl 2.5, NaH2PO4 1.3, MgCl2 7, NaHCO3 25, sucrose 75, ascorbate 5, CaCl2 0.5, in ddH2O; 320–330 mOsm, pH 7.30–7.40, saturated with 95% O2 / 5% CO2). The brain was sectioned using a Compresstome (Precisionary Instruments Inc.) and slices were incubated in ACSF (containing in mM: NaCl 124, KCl 2.5, NaH2PO4 1.25, MgSO4 1, NaHCO3 25, sodium pyruvate 3, sodium L-ascorbate 0.5, myo inositol 3, taurine 0.01, glucose 10, CaCl2 1.2, in ddH2O; 299–301 mOsm; pH 7.35–7.45, saturated with 95% O2 / 5% CO2) at 32°C for ≥ 90 min before being transferred to the recording chamber for electrophysiology. Once in the recording chamber, slices were continuously perfused at a rate of 2 ml/min with fully oxygenated ACSF at 22°C with added Picrotoxin (100 μM) and kynurenic acid (1 mM) to block GABAergic and glutamatergic synaptic transmission. Neurons were identified under DIC based on pyramidal morphology rather than fluorescence and optical activation with 500-ms light pulses was

delivered using 473 or 625 nm LEDs (Thorlabs), which were additionally filtered with a 632 nm ± 11 nm filter (Semrock). 4–6 MΩ borosilicate glass pipettes (Kings Precision Glass) filled with internal solution containing (in mM): potassium gluconate 120, KCl 7, EGTA 1, HEPES 10, Mg-ATP 3, Na-GTP 0.4, phosphocreatine 10; 290 mOsm; pH 7.3) were used for whole-cell patch-clamp recording in slice. During recording, membrane capacitance (Cm), series resistance (Rs) and input resistance (Rin) were frequently monitored. All cells patched were included in data analysis.

References

1. Madisen, L. et al. A robust and high-throughput Cre reporting and characterization system for the whole mouse brain. *Nature neuroscience* **13**, 133-140 (2010).
2. Muzumdar, M.D., Tasic, B., Miyamichi, K., Li, L. & Luo, L. A global double-fluorescent Cre reporter mouse. *Genesis* **45**, 593-605 (2007).
3. Gerfen, C.R., Paletzki, R. & Heintz, N. GENSAT BAC cre-recombinase driver lines to study the functional organization of cerebral cortical and basal ganglia circuits. *Neuron* **80**, 1368-1383 (2013).
4. Gong, S. et al. Targeting Cre recombinase to specific neuron populations with bacterial artificial chromosome constructs. *J Neurosci* **27**, 9817-9823 (2007).
5. Taniguchi, H. et al. A resource of Cre driver lines for genetic targeting of GABAergic neurons in cerebral cortex. *Neuron* **71**, 995-1013 (2011).
6. Arenkiel, B.R. et al. In vivo light-induced activation of neural circuitry in transgenic mice expressing channelrhodopsin-2. *Neuron* **54**, 205-218 (2007).
7. Zhao, S. et al. Improved expression of halorhodopsin for light-induced silencing of neuronal activity. *Brain cell biology* **36**, 141-154 (2008).
8. Dhawale, A.K., Hagiwara, A., Bhalla, U.S., Murthy, V.N. & Albeanu, D.F. Non-redundant odor coding by sister mitral cells revealed by light addressable glomeruli in the mouse. *Nature neuroscience* **13**, 1404-1412 (2010).
9. Hagglund, M., Borgius, L., Dougherty, K.J. & Kiehn, O. Activation of groups of excitatory neurons in the mammalian spinal cord or hindbrain evokes locomotion. *Nature neuroscience* **13**, 246-252 (2010).
10. Zhao, S. et al. Cell type-specific channelrhodopsin-2 transgenic mice for optogenetic dissection of neural circuitry function. *Nature methods* **8**, 745-752 (2011).
11. Smear, M., Shusterman, R., O'Connor, R., Bozza, T. & Rinberg, D. Perception of sniff phase in mouse olfaction. *Nature* **479**, 397-400 (2011).
12. Katzel, D., Zemelman, B.V., Buetfering, C., Wolfel, M. & Miesenbock, G. The columnar and laminar organization of inhibitory connections to neocortical excitatory cells. *Nature neuroscience* **14**, 100-107 (2011).
13. Tsunematsu, T. et al. Acute optogenetic silencing of orexin/hypocretin neurons induces slow-wave sleep in mice. *The Journal of neuroscience : the official journal of the Society for Neuroscience* **31**, 10529-10539 (2011).

14. Madisen, L. et al. A toolbox of Cre-dependent optogenetic transgenic mice for light-induced activation and silencing. *Nature neuroscience* **15**, 793-802 (2012).
15. Asrican, B. et al. Next-generation transgenic mice for optogenetic analysis of neural circuits. *Frontiers in neural circuits* **7**, 160 (2013).
16. Tsunematsu, T. et al. Optogenetic manipulation of activity and temporally controlled cell-specific ablation reveal a role for MCH neurons in sleep/wake regulation. *The Journal of neuroscience : the official journal of the Society for Neuroscience* **34**, 6896-6909 (2014).
17. Zeng, H. et al. An inducible and reversible mouse genetic rescue system. *PLoS genetics* **4**, e1000069 (2008).
18. Garner, A.R. et al. Generation of a synthetic memory trace. *Science (New York, N.Y* **335**, 1513-1516 (2012).
19. Gossen, M. & Bujard, H. Tight control of gene expression in mammalian cells by tetracycline-responsive promoters. *Proceedings of the National Academy of Sciences of the United States of America* **89**, 5547-5551 (1992).
20. Mayford, M. et al. Control of memory formation through regulated expression of a CaMKII transgene. *Science (New York, N.Y* **274**, 1678-1683 (1996).
21. Reijmers, L.G., Perkins, B.L., Matsuo, N. & Mayford, M. Localization of a stable neural correlate of associative memory. *Science (New York, N.Y* **317**, 1230-1233 (2007).
22. Chung, J.H., Bell, A.C. & Felsenfeld, G. Characterization of the chicken beta-globin insulator. *Proceedings of the National Academy of Sciences of the United States of America* **94**, 575-580 (1997).
23. Gaszner, M. & Felsenfeld, G. Insulators: exploiting transcriptional and epigenetic mechanisms. *Nature reviews. Genetics* **7**, 703-713 (2006).
24. Chen, T.W. et al. Ultrasensitive fluorescent proteins for imaging neuronal activity. *Nature* **499**, 295-300 (2013).
25. Akemann, W. et al. Imaging neural circuit dynamics with a voltage-sensitive fluorescent protein. *Journal of neurophysiology* **108**, 2323-2337 (2012).
26. Marvin, J.S. et al. An optimized fluorescent probe for visualizing glutamate neurotransmission. *Nature methods* **10**, 162-170 (2013).
27. Chuong, A.S. et al. Noninvasive optical inhibition with a red-shifted microbial rhodopsin. *Nature neuroscience* (2014).
28. Gradinaru, V. et al. Molecular and cellular approaches for diversifying and extending optogenetics. *Cell* **141**, 154-165 (2010).
29. Chow, B.Y. et al. High-performance genetically targetable optical neural silencing by light-driven proton pumps. *Nature* **463**, 98-102 (2010).
30. Han, X. et al. A high-light sensitivity optical neural silencer: development and application to optogenetic control of non-human primate cortex. *Frontiers in systems neuroscience* **5**, 18 (2011).
31. Sohal, V.S., Zhang, F., Yizhar, O. & Deisseroth, K. Parvalbumin neurons and gamma rhythms enhance cortical circuit performance. *Nature* **459**, 698-702 (2009).
32. Lein, E.S. et al. Genome-wide atlas of gene expression in the adult mouse brain. *Nature* **445**, 168-176 (2007).
33. Harris, J.A. et al. Anatomical characterization of cre driver mice for neural circuit mapping and manipulation. *Frontiers in neural circuits* **8** (2014).

Chapter 4 - Discussion

Practical considerations for implementing optogenetic inhibition

In this thesis, I have demonstrated highly efficient red-light-driven inhibition of neural activity using Jaws. However there are limits to these tools, and there are stimulation regimes in which the inhibition data may be difficult to interpret not only for Jaws, but also for all optogenetic inhibitors.

The rate-limiting step in optogenetic experiments is almost always balancing high functional expression levels against cell health, while simultaneously achieving cell-type specificity for the neuronal subpopulation of interest. The optogenetic activation of a small subset of neurons has been demonstrated to drive robust behavioral responses[1, 2]: the converse of this is that behaviorally meaningful optogenetic inhibition may necessitate not only strong single-molecule biophysics, but also large-volume expression and modulation.

It has been previously well established that longer wavelength light propagates further in tissue and I have demonstrated here that ~40 nm off-peak stimulation can successfully drive an opsin, but it is important to note diminishing returns as the illumination wavelength moves further off peak: because Jaws' peak is ~600 nm, the photocurrents at 600 nm will still always be double those at 640 nm. While Jaws has successfully inhibited *in vivo* neural activity at wavelengths up to 660 nm, the substantially lower photocurrents necessitate more input light power. If an experiment does not require large volume modulation, yellow illumination will always provide the best performance.

While optogenetic tool efficacy is commonly reported as photocurrent from *in vitro* or *ex vivo* slice, this may not be informative within an *in vivo* context. The majority of these characterizations only demonstrate photocurrent efficacy in response to a short 100 ms-5s illumination pulse, but most *in vivo* experiments involve longer illumination durations on a seconds-to-minutes timescale over multiple, repeated trials. Pump desensitization/inactivation is therefore also more prominent *in vivo*, in particular because light powers for *in vitro* or *ex vivo* slice characterizations are typically ten-to-a-hundred-fold lower than those used *in vivo*. These high light intensities further exacerbate the problem of inactivation. In addition to light

intensities, opsin recovery is also a function of wavelength, reflecting the fact that different photocycle intermediates absorb at different wavelengths. UV/blue light illumination can partially reset red-shifted opsins to ground state and therefore be used to probe the degree of inactivation/recovery[3]. It is also important to note that the geometric nature of illumination fall off means neurons closer to the optical source may be substantially more hyperpolarized for extended durations than neurons on the illumination periphery.

Subcellular expression is another major issue for *in vivo* implementation, due to the fact that illumination is often difficult to precisely control and target to specific areas *in vivo*. It is becomingly an increasingly common practice to report optogenetic light powers as estimated at a neuron rather than the power directly out of the illumination source hundreds of microns away. This estimated value is meaningless, because the exact distance between the illumination source and neuron cannot be known (without additional elaborate experiments), because irradiance scales and propagates differently depending on the size of the illumination source, and because light propagation in brain tissue is not only heterogeneous but also differs dramatically depending on the cell types in that brain region. This geometric nature of fall-off also makes it difficult to draw biophysical conclusions from opsin characterization in slice where illumination is delivered via a 200 um fiber (rather than whole field illumination), since the final data is so subject to fiber position.

Finally, it is important to note that while inhibitory opsin characterization is typically carried out by patching at the soma while illuminating the entire cell, experimenters frequently want to shut down processes/inputs which may have very different inhibition efficacies than at the soma. Many *in vitro* or *ex vivo* characterizations are designed to inhibit electrically evoked spiking, which frequently has substantially different input drives than spontaneous neuronal spiking, which in turn may have very different strengths than sensory or behaviorally evoked spiking. While it is a common practice to validate opsin function in a given brain region and behavioral paradigm in slice, it therefore is critical to carry out simultaneous *in vivo* electrophysiology using the same expression and illumination conditions as used for the behavior since slice or *in vitro* results may not translate.

Multi-color control

Multicolor optogenetics, either in the form of modulating two independent neural populations or in the bidirectional control of a single neural population, has been a topic of great interest since the optogenetic toolbox was first expanded beyond the *C. reinhardtii* channelrhodopsin-2 to include VChR1 and the *N. pharaonis* halorhodopsin. While Jaws' red-shifted spectrum does suggest some potential for multicolor control, it is important to note that all microbial opsins share the same retinal chromophore with an intrinsic blue light absorption due to retinal's peak absorbance between 350-450 nm[4]. This absorption leads all opsins to retain a blue shoulder independent of red-shift, which may still be sufficient to substantially shift a neuron's excitability, particularly over long illumination durations where charge is integrated.

Kinetic gating strategies utilizing the channelrhodopsins Chrimson and Chronos have been previously successful in independently controlling two different channelrhodopsin populations[5], by exploiting kinetic as well as spectral differences to define an operational blue light range in which the Chronos blue partner could be activated with short 5 ms light pulses without activating the Chrimson red partner. However, it is important to note that long light pulses still elicited spiking in Chrimson (Figure 4.1).

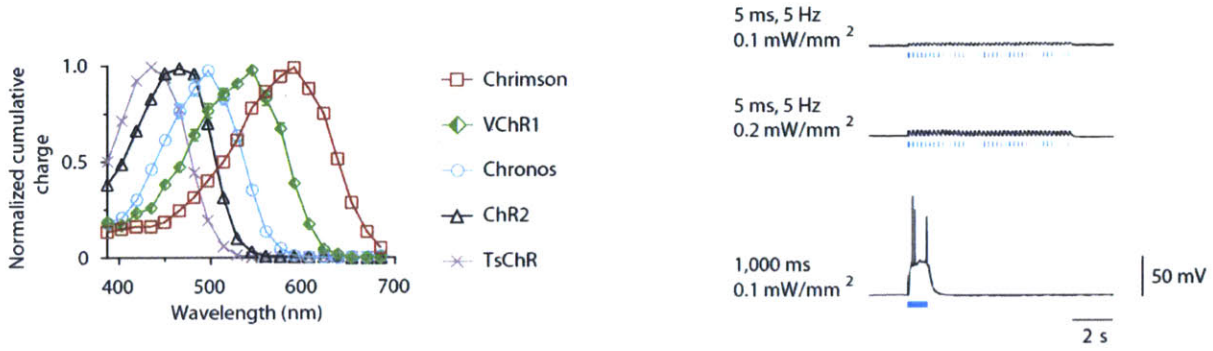

Figure 4.1 - Long illumination durations integrate charge independent of spectrum.

Action spectrum (*left*), and current-clamp traces (*right*) of representative Chrimson-expressing neuron using different pulse-widths, demonstrating that longer (or continuous) blue illumination can lead to the integration of charge even at off-peak colors. Figure modified from Klapoetke *et al*[5].

In contrast to channelrhodopsins, hyperpolarizing opsins are typically controlled using sustained illumination on the seconds-to-minutes timescale. Without the ability to predict when

a given neuron will spike (and thus to illuminate with short pulses within that interval), it is impossible to inhibit a single cell's activity using an optogenetic pump without sustained illumination which drives crosstalk in the other partner.

It is additionally important to note the difficulty of precisely controlling light powers in the intact *in vivo* brain, as well as the substantially different conductances between channels and pumps. While it is therefore theoretically possible to use Jaws with a blue channelrhodopsin partner, this must be empirically determined for each system of interest due to the number of factors it depends upon, which include opsin expression level and subcellular trafficking, illumination duration, and optical scattering in tissue in addition to spectrum. Crosstalk for two color inhibition is a more complex problem, given that hyperpolarizing opsins have similar light sensitivity and can be driven in the blue. For example, Jaws' activation at 470 nm is approximately 40% of its peak, while its activation at 630 nm is 54%. In order to achieve robust separation in the blue, it is therefore necessary for the blue inhibitory opsin partner to have high light sensitivity and conductance.

Future directions for optogenetic inhibition

While I have demonstrated large volume inhibition using Jaws in the rodent brain, a great deal more work remains to be done before application to larger-brained species such as the non-human primate, or clinical applications in the human brain. The cubic scaling of volume is critical. Primate neural modulation has previously been successfully carried out using channelrhodopsins[6-10], but corresponding inhibitory studies have been less successful and have been primarily limited to electrophysiology without a substantial quantifiable behavioral output[6, 10-12] and require light powers of up to 1000 mW/mm^2 out of a 200 um fiber tip.

The extent to which opsin spectra can be further shifted remains yet to be seen. One possibility for spectral shift is the utilization of different retinal chromophores such as A2 retinal, which successfully induced a spectral redshift of 30-40 nm in Arch or CaChR1[13]. However, the use of this system would be constrained primarily to species such as *Drosophila* or *C. elegans* which do not possess basal endogenous retinal levels sufficient for optogenetic experiments (and therefore must be fed retinal-supplemented media); mammalian usage would not only require the heterologous expression of this retinal isomer but also necessitate the engineering of an

orthogonal opsin which would utilize the new chromophore without binding to endogenous all-*trans*-retinal. Manipulation of the opsin protein alone without altering the chromophore partner thus seems more practical for mammalian use.

Shifts in retinal spectral absorption have been well established as the result of electrostatic interactions between the retinal chromophore and chromophore binding pocket, leading to shifts in electrostatic distribution over the chromophore itself. Changes in this electrostatic distribution can result in a retinal spectral range of up to 220 nm, and a λ_{max} of up to 644 nm, roughly 45 nm more red than that of Jaws[14, 15]. It should therefore be theoretically possible, although perhaps technically difficult to achieve while preserving ion transport functions, to further red-shift Jaws. Another possibility is substantially boosting Jaws' photocurrent, either through boosting the turnover rate, conductance, or expression level and driving the opsin on its near infrared shoulder.

The generation and engineering of a chloride-selective or potassium-selective channel would be of great interest. While this has previously been demonstrated with the ChloCs[16] (chloride-conducting ChRs), iC1C2[17] and SwiChR$_{CT}$[17] using channelrhodopsin-2 as a protein engineering substrate, the same mutations did not translate to Chrimson, most likely due to low sequence homology. These constructs additionally have very low conductances, which must be substantially boosted before practical implementation.

Finally, it is important to note that actuating tools, by their nature, should ideally perturb a system's basal activity as little as possible. Because all microbial opsins are transmembrane proteins, the only functionally relevant protein is that which traffics to and properly inserts into the membrane. However, differences in trafficking between these proteins' original archaeal or algal origins and their experimental system of use has been frequently problematic and boosting heterologous expression levels can place undue stress on endogenous protein folding or translocation pathways[18-23]. While rudimentary improvements have been made via trafficking sequences and codon optimization, it would be of great use to examine other methods of improving opsin trafficking.

References

1. Choi, G.B. et al. Driving opposing behaviors with ensembles of piriform neurons. *Cell* **146**, 1004-1015 (2011).
2. Huber, D. et al. Sparse optical microstimulation in barrel cortex drives learned behaviour in freely moving mice. *Nature* **451**, 61-64 (2008).
3. Bamberg, E., Tittor, J. & Oesterhelt, D. Light-driven proton or chloride pumping by halorhodopsin. *Proceedings of the National Academy of Sciences of the United States of America* **90**, 639-643 (1993).
4. Waddell, W.H., Schaffer, A.M. & Becker, R.S. Visual pigments. 3. Determination and interpretation of the fluorescence quantum yields of retinals, Schiff bases, and protonated Schiff bases. *Journal of the American Chemical Society* **95**, 8223-8227 (1973).
5. Klapoetke, N.C. et al. Independent optical excitation of distinct neural populations. *Nature methods* (2014).
6. Diester, I. et al. An optogenetic toolbox designed for primates. *Nature neuroscience* **14**, 387-397 (2011).
7. Gerits, A. et al. Optogenetically Induced Behavioral and Functional Network Changes in Primates. *Current biology : CB* (2012).
8. Han, X. et al. Millisecond-timescale optical control of neural dynamics in the nonhuman primate brain. *Neuron* **62**, 191-198 (2009).
9. Jazayeri, M., Lindbloom-Brown, Z. & Horwitz, G.D. Saccadic eye movements evoked by optogenetic activation of primate V1. *Nature neuroscience* (2012).
10. Ohayon, S., Grimaldi, P., Schweers, N. & Tsao, D.Y. Saccade modulation by optical and electrical stimulation in the macaque frontal eye field. *The Journal of neuroscience : the official journal of the Society for Neuroscience* **33**, 16684-16697 (2013).
11. Cavanaugh, J. et al. Optogenetic inactivation modifies monkey visuomotor behavior. *Neuron* **76**, 901-907 (2012).
12. Han, X. et al. A high-light sensitivity optical neural silencer: development and application to optogenetic control of non-human primate cortex. *Frontiers in systems neuroscience* **5**, 18 (2011).
13. Sineshchekov, O.A., Govorunova, E.G., Wang, J. & Spudich, J.L. Enhancement of the long-wavelength sensitivity of optogenetic microbial rhodopsins by 3,4-dehydroretinal. *Biochemistry* **51**, 4499-4506 (2012).
14. Wang, W. et al. Tuning the electronic absorption of protein-embedded all-trans-retinal. *Science* **338**, 1340-1343 (2012).
15. Chuong, A.S. et al. Noninvasive optical inhibition with a red-shifted microbial rhodopsin. *Nature neuroscience* (2014).
16. Wietek, J. et al. Conversion of channelrhodopsin into a light-gated chloride channel. *Science* **344**, 409-412 (2014).
17. Berndt, A., Lee, S.Y., Ramakrishnan, C. & Deisseroth, K. Structure-guided transformation of channelrhodopsin into a light-activated chloride channel. *Science* **344**, 420-424 (2014).
18. Griffith, D.A., Delipala, C., Leadsham, J., Jarvis, S.M. & Oesterhelt, D. A novel yeast expression system for the overproduction of quality-controlled membrane proteins. *FEBS letters* **553**, 45-50 (2003).

19. Klepsch, M.M., Persson, J.O. & de Gier, J.W. Consequences of the overexpression of a eukaryotic membrane protein, the human KDEL receptor, in Escherichia coli. *Journal of molecular biology* **407**, 532-542 (2011).
20. Valent, Q.A. et al. Nascent membrane and presecretory proteins synthesized in Escherichia coli associate with signal recognition particle and trigger factor. *Molecular microbiology* **25**, 53-64 (1997).
21. Wagner, S. et al. Consequences of membrane protein overexpression in Escherichia coli. *Molecular & cellular proteomics : MCP* **6**, 1527-1550 (2007).
22. Wagner, S. et al. Tuning Escherichia coli for membrane protein overexpression. *Proceedings of the National Academy of Sciences of the United States of America* **105**, 14371-14376 (2008).
23. Xu, L.Y. & Link, A.J. Stress responses to heterologous membrane protein expression in Escherichia coli. *Biotechnology letters* **31**, 1775-1782 (2009).

Appendix - Dye Screening

Whole-cell patch clamping has been widely adopted as the standard technique for characterizing ion channels and pumps due to its picoampere resolution, but it has a relatively slow throughput compared to imaging-based approaches. While rational mutagenesis using channelrhodopsin-2 as a template has previously enjoyed some success[1, 2], halorhodopsin or archaerhodopsin mutagenesis has been less successful. The *H. salinarum* (strain Shark) halorhodopsin is 277 amino acids long, leading to a theoretical 4^{831} genetic sequences yielding a potential 20^{272} different proteins. While this process can to some extent be simplified by knowledge of different amino acid properties, the problem of fully exploring sequence space is still massive. We therefore reasoned that dye-based approaches might be one way to improve screening throughput.

In order to explore a large sequence space, I designed a saturation mutagenesis library for the *H. salinarum* (strain Shark) cruxhalorhodopsin using NNK mutagenesis primers, which encoded all 20 amino acids as well as one stop codon. NNK primers were used due to the fact that they introduce less sequence bias than noisy PCR. I transfected HEK293FT cells with calcium phosphate and loaded the membranes with oxonol FRET voltage-sensitive dye (Figure 5.; CC2-DMPE (donor); $DiSBAC_2(3)$ (acceptor))[3, 4] two days post-transfection.

All opsin constructs examined were fused to GFP at their C terminus. I used GFP fluorescence to generate image masks in Cell Profiler for analyzing oxonol dye fluorescence (Figure 5.), and carried out simultaneous whole-cell patch clamp while dye imaging (Figure 5.). 360 nm light was delivered to excite the dye, while the opsin was driven with 625 nm illumination. It is important to note that the opsin still mediated 8 mV hyperpolarization at 360 nm, approximately 250 nm off-peak and less than 25% of the opsin's peak activation, due to intrinsic retinal activation. While this crosstalk was relatively minimal compared to the -58 mV red light deflection, crosstalk will be more substantial for more blue-shifted opsins such as Arch or NpHR.

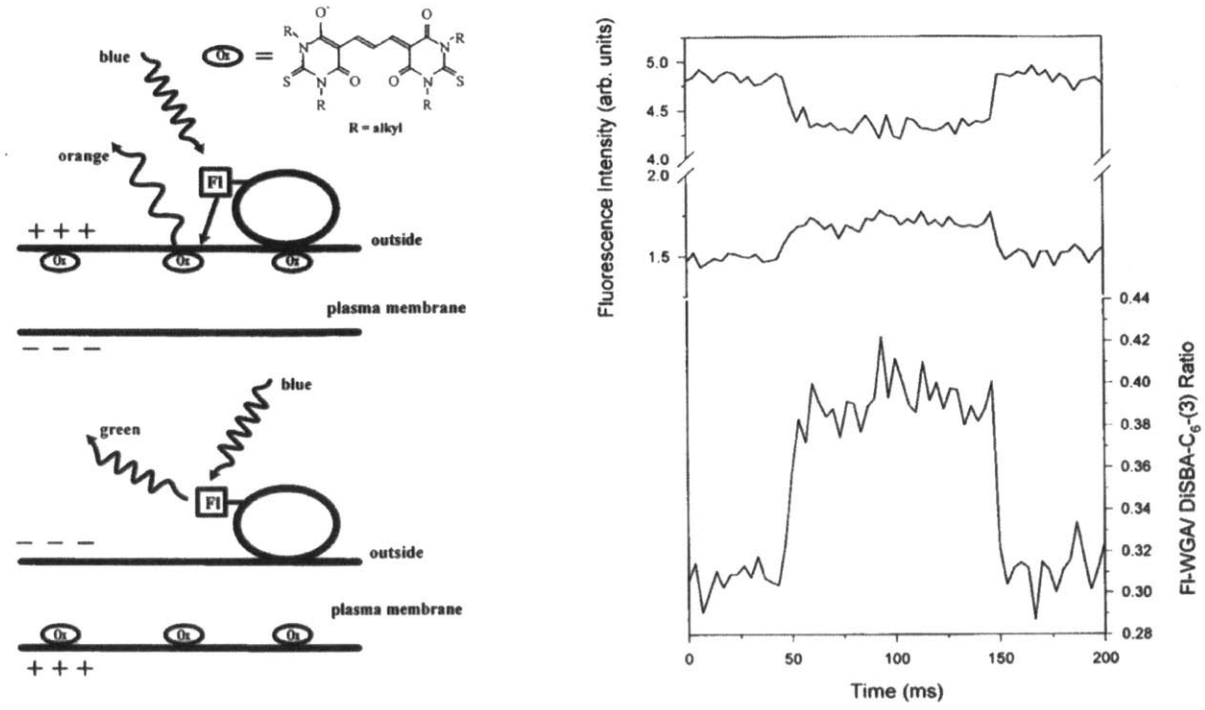

Figure 5.1 - Oxonol dye screening

Schematic of oxonol FRET mechanism (left) and representative oxonol dye fluorescence changes elicited by changes in voltage (right). Figure modified from Gonzalez *et al.* 2005[4].

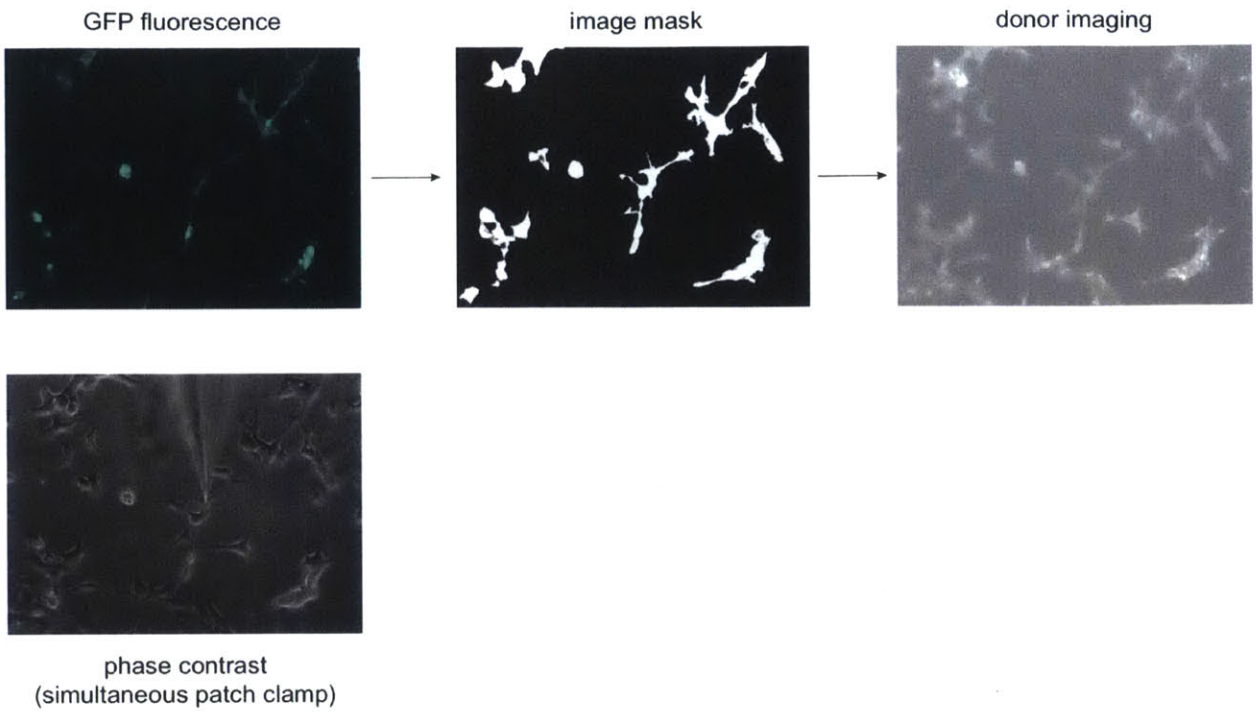

Figure 5.2 - Screening workflow

Representative images from screening process. Image masks (*top, center*) for analyzing dye fluorescence (*top right*) were generated from GFP fluorescence (*top left*), while I carried out simultaneous whole-cell patch clamping (*bottom*).

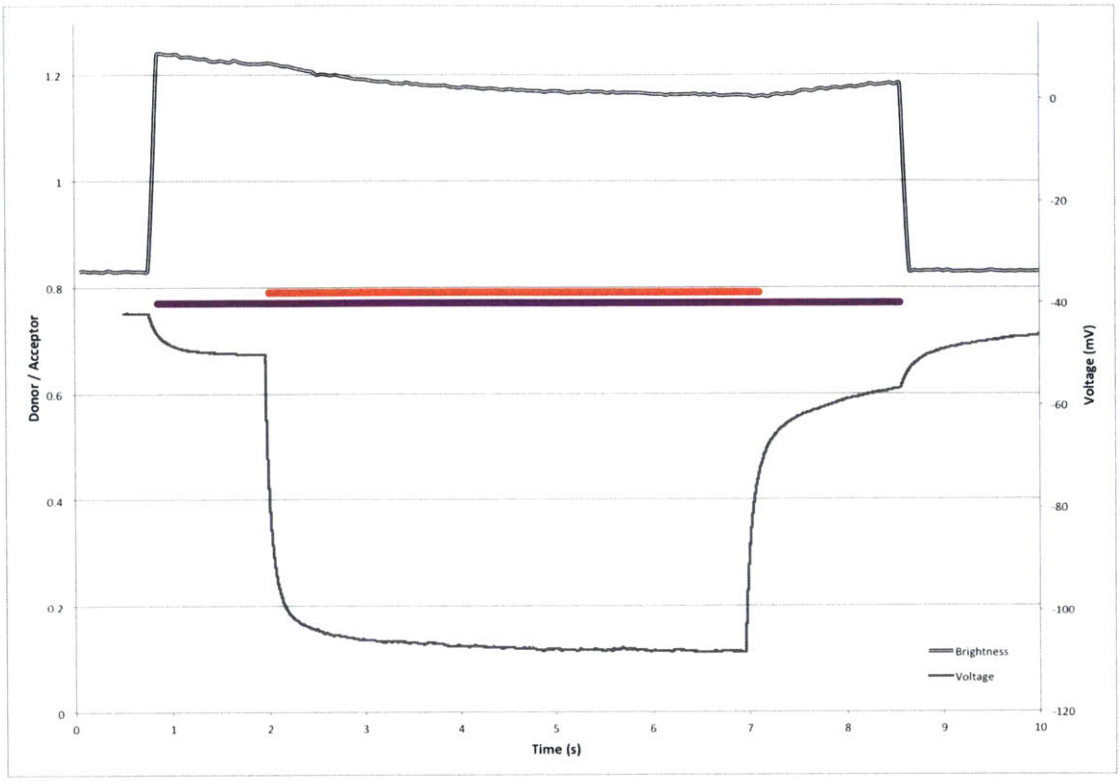

Figure 5.3 - Simultaneous oxonol dye imaging and whole-cell patch clamping.

Sample fluorescence (*top*) and current-clamp (*bottom*) trace from HEK293FT cell transfected with an *H. salinarum* (strain Shark) mutant, incubated in 40 uM CC2-DMPE and 5 uM DiSBAC2(3), and illuminated with 360 nm (purple) and 625 nm (red) to respectively drive the dye and opsin.

Using this method, I examined several hyperpolarizing constructs and compared the results gathered through dye screening and patch clamping data (data not shown). I found little correlation between the two metrics, suggesting that higher resolution sensors or a more refined screening process may be necessary for future work.

Dye screening methods have a substantially higher potential throughput than other methods for measuring opsin activation. The fundamental problem is the conflation of dye and opsin excitation without a way to separate the two. Additionally, the signal to noise ratio was also extremely low: a deflection of approximately 10 mV led to a fluorescence change of around 1%, which meant that only mutations with extremely large effects could be optically resolved. It would therefore be advantageous to have better dye-based or genetically encoded tools with an improved signal-to-noise ratio.

References

1. Gunaydin, L.A. et al. Ultrafast optogenetic control. *Nature neuroscience* **13**, 387-392 (2010).
2. Lin, J.Y., Lin, M.Z., Steinbach, P. & Tsien, R.Y. Characterization of engineered channelrhodopsin variants with improved properties and kinetics. *Biophysical journal* **96**, 1803-1814 (2009).
3. Gonzalez, J.E. & Maher, M.P. Cellular fluorescent indicators and voltage/ion probe reader (VIPR) tools for ion channel and receptor drug discovery. *Receptors & channels* **8**, 283-295 (2002).
4. Gonzalez, J.E. & Tsien, R.Y. Voltage sensing by fluorescence resonance energy transfer in single cells. *Biophysical journal* **69**, 1272-1280 (1995).